Title
Design and Deployment of the Simons Array Cosmic Microwave Background Polarization Instrument

Author
Groh, John Collin

Publication Date
2021

Peer reviewed|Thesis/dissertation

Design and Deployment of the Simons Array Cosmic Microwave Background Polarization Instrument

by

John Collin Groh

A dissertation submitted in partial satisfaction of the

requirements for the degree of

Doctor of Philosophy

in

Physics

in the

Graduate Division

of the

University of California, Berkeley

Committee in charge:

Professor Adrian Lee, Chair
Professor William Holzapfel
Professor Aaron Parsons

Spring 2021

Design and Deployment of the Simons Array Cosmic Microwave Background Polarization Instrument

Abstract

Design and Deployment of the Simons Array Cosmic Microwave Background Polarization Instrument

by

John Collin Groh

Doctor of Philosophy in Physics

University of California, Berkeley

Professor Adrian Lee, Chair

The cosmic microwave background (CMB) provides a powerful tool for study of the history and evolution of the universe. Several decades of CMB measurements have yielded an increasingly clearer picture of the contents, structure, history, and fate of the cosmos. While some information channels in the CMB have been measured to their fundamental sensitivity limit, a host of physics remains to be extracted from the faint polarization anisotropies and small-scale angular correlations of the CMB. To such an end, a vibrant field of complementary measurements has developed over time. Adding to these is the Simons Array, a new ground-based telescope array in the Chilean Atacama desert designed to simultaneously search for signatures of cosmic inflation and precisely characterize the gravitational lensing of the CMB by large-scale cosmic structure.

This thesis describes the Simons Array design as well as several developments that have enabled its sensitivity and their implementation in the experiment. After a brief overview of the scientific motivations and measurement strategies of CMB polarization imaging surveys, an overview of the design and construction of the Simons Array instruments is given. The development of optimized packaging and assembly of close-packed detector hardware and developments in the cryomechanical support of large cryogenic detector arrays are then described. Additionally, advances in the frequency division multiplexed readout of CMB detector arrays representing a factor of several increase in multiplexing capability are presented. Finally, the integration and field commissioning of the first Simons Array telescope is described, and a summary of its initial performance during observations is given.

Contents

List of Figures

List of Tables

Acknowledgments

Measurements of the cosmic microwave background now require such complicated, massive, and expensive apparatuses that one student cannot progress in isolation. My experience has been no exception, and over the course of my trajectory through graduate school I have become indebted to many. In addition to the POLARBEAR collaboration as a whole, several others have been particularly helpful during my time in Berkeley to whom I would like to extend my gratitude here.

First and foremost, I owe a great deal of thanks to my advisor, Adrian Lee. Even as a young inexperienced student, Adrian allowed me to learn with both enormous freedom and responsibility, and he opened my eyes to realize just how much one person can accomplish. I would also like to thank Professors Bill Holzapfel, Kam Arnold, and Akito Kusaka - all excellent collaborators from whom I received both technical and personal advice.

Throughout my time in graduate school, I benefited greatly by learning from my seniors and predecessors in the Berkeley group - in particular Aritoki Suzuki, Ari Cukierman, and Darcy Barron, with whom I worked closely - but also Neil Goeckner-Wald, Charlie Hill, Ben Westbrook, Yuji Chinone, Kevin Crowley, Nathan Whitehorn, Tijmen de Haan, and Nick Harrington. Thanks as well to my fellow graduate students Nick Huang, Jessica Avva, and Shawn Beckman for pleasant collaboration and office banter. Additional thanks to Kevin Crowley and Tylor Adkins, who made a very long and otherwise lonely deployment to the telescope site during the COVID-19 pandemic both possible and enjoyable.

Finally, I would like to thank my mother and father, who provided me with the tools for success and encouraged me to follow my interests.

Chapter 1

Introduction

Studies of the cosmic microwave background (CMB) have been central to the formation of the modern understanding of the universe. Furthermore, a significant amount of information about many open questions in physics and cosmology still remains to be learned from the CMB. This chapter introduces the standard cosmological model and the CMB, further presenting an overview of how information on the primary science targets of the Simons Array may be extracted from the CMB anisotropies. A description of general measurement challenges is also given, along with a brief overview of recent and upcoming CMB anisotropy measurements.

1.1 The universe, on average

In the modern era, observations firmly support the idea that the Earth does not appear to occupy a special place in the universe. Specifically, on large scales the universe appears nearly *homogeneous*, meaning that other regions of the universe spatially distant from us look the same as they do here, and *isotropic*, meaning that there is no preferred direction. Ignoring for the moment[1] the deviations from uniformity which we know to exist (cosmic structures and voids, galaxies, stars, planets, humans), from geometric arguments alone the assumptions of isotropy and homogeneity lead to a spacetime metric $g_{\mu\nu}$

$$g_{tt} = -1, \;\; g_{0i} = g_{ij} = 0, \;\; g_{rr} = a^2(t)\frac{1}{1-kr^2}, \;\; g_{\theta\theta} = a^2(t)r^2, \;\; g_{\phi\phi} = a^2(t)r^2\sin^2\theta \qquad (1.1)$$

which is unique up to a coordinate transformation. The metric (1.1) is often referred to as the *Friedmann-Robertson-Walker metric*. Expressed in this way, the curvature k can take only the values of ± 1 or 0; all data to date is consistent with zero curvature, and so k will henceforth be set to 0.

[1] These deviations are often small enough that the following solution remains of great utility, on top of which deviations may be treated perturbatively. This is revisited in Section 1.2

The dynamics of the metric in (1.1) are determined solely by the single function $a(t)$, typically referred to as the scale factor and conventionally normalized to be 1 at the present day. To determine the evolution of the scale factor, one must first specify the energy content of the universe and turn to Einstein's equations of general relativity

$$\mathcal{R}_{\mu\nu} - \frac{1}{2} g_{\mu\nu}\mathcal{R} = 8\pi G_{\rm N} T_{\mu\nu} \tag{1.2}$$

where $\mathcal{R}_{\mu\nu}$ and $\mathcal{R}$ are the Ricci tensor and scalar, respectively. The stress-energy tensor $T_{\mu\nu}$ specifies the energy content as a source term, and using the assumptions of homogeneity and isotropy it may be treated as a perfect fluid with pressure p and density ρ

$$T_{\mu\nu} = -p g_{\mu\nu} + (p+\rho) u_\nu u_\nu \tag{1.3}$$

where u is the timelike unit vector. Inserting (1.1) and (1.3) into (1.2), one can arrive at the Friedmann equations for the dynamics of the scale factor:

$$\left(\frac{\dot{a}}{a}\right)^2 = \frac{8\pi G_{\rm N}\rho}{3} \tag{1.4}$$

$$\frac{\ddot{a}}{a} = -\frac{4\pi G_{\rm N}}{3}(\rho + 3p) \tag{1.5}$$

where dotted quantities indicate derivatives with respect to the time coordinate. The first of these may be more suggestively written in terms of the Hubble parameter $H \equiv \frac{\dot{a}}{a}$, the critical density $\rho_{\rm crit} \equiv \frac{3H^2}{8\pi G_{\rm N}}$, and the cosmological density parameters $\Omega_i \equiv \frac{\rho_i}{\rho_{\rm crit}}$ for various contributions to the cosmological energy budget labeled by i:

$$H^2 = H_0^2 \sum_i \Omega_i \tag{1.6}$$

where $\sum_i \Omega_i = 1$, and H_0 denotes the value of the Hubble parameter today.

It is the job of the cosmologist to enumerate all the types of energy content that contribute terms Ω_i to the sum in (1.6) and measure their relative densities. A useful tool for this enumeration is the equation of state parameter $w \equiv p/\rho$. A combination of three limiting cases - matter, radiation, and a cosmological constant - are sufficient to explain the observed expansion history, and their measured current relative densities $\Omega_{i,0}$ are listed in Table 1.1.

	w	$a(t)$ when only contributor	$\Omega_{i,0}$
Matter	0	$\propto t^{2/3}$	0.31
Radiation	1/3	$\propto t^{1/2}$	5.4×10^{-5}
Cosmological constant	-1	$\propto e^{Ht}$	0.69

Table 1.1: A few special cases of interest in the cosmic inventory, along with their equation of state parameters, the evolution of the scale factor in a universe where each is the only contributor, and their current density parameters.

A major success of modern cosmology are the discovery that most of the matter energy density Ω_m is in fact not in the form of Standard Model particles. The matter content of the universe appears to be dominated by nonrelativistic matter which interacts primarily through gravitation with other Standard Model particles, termed *cold dark matter*. The remaining matter is typically called *baryonic matter* to indicate that most of the energy density in normal matter comes from protons and neutrons. Current measurements place the cold dark matter density Ω_c and baryonic matter density Ω_b at 84% and 16% of Ω_m, respectively [1].

A second major breakthrough has been that the majority of the energy content of the universe appears to be in the form of a vacuum energy density Ω_Λ. Currently, it is not known if this so-called *dark energy* is the cosmological constant originally suggested by Einstein or potentially more exotic in origin. In the case of a cosmological constant Λ, the energy of the vacuum may be interpreted as a property of spacetime rather than part of the stress-energy tensor, and Einstein's equations are often written in this case as

$$\mathcal{R}_{\mu\nu} - \frac{1}{2} g_{\mu\nu}\mathcal{R} + \Lambda g_{\mu\nu} = 8\pi G_{\rm N} T_{\mu\nu} \tag{1.7}$$

Efforts are underway to precisely measure whether the equation of state parameter w for dark energy differs from -1 or has evolved over cosmic history; current constraints are consistent with a simple cosmological constant [1].

The densities Ω_m, Ω_r, and Ω_Λ all dilute with dependences on the scale factor a. The density of a fixed quantity of matter simply depends on the volume in which it is contained, so one may write $\Omega_m = \Omega_{m,0}/a^3$. The energy of radiation similarly dilutes volumetrically, but since the energy of a photon is also inversely proportional to its wavelength, which gets stretched with spacetime expansion, an extra factor of the scale factor appears in the dilution of radiation density: $\Omega_r = \Omega_{r,0}/a^4$. A cosmological constant is by definition constant, so $\Omega_\Lambda = \Omega_{\Lambda,0}$. These dilutions are collectively shown in Figure 1.1(a).

It is instructive to note that in a universe with only matter ($\Omega_m = 1$) or in a universe with only radiation ($\Omega_r = 1$), the Friedmann equations can be easily solved for $a(t)$, resulting in decelerating expansion as also listed in Table 1.1. In a universe dominated by a cosmological constant ($\Omega_\Lambda = 1$), the expansion is accelerating. For our universe with matter, radiation, and dark energy, however, one may proceed numerically by inserting the dilution scalings $\Omega_i(a)$ into (1.6), integrating

$$t(a) = \frac{1}{H_0}\int_0^a \frac{da'/a'}{\sqrt{\Omega_{m,0}/a'^3 + \Omega_{r,0}/a'^4 + \Omega_{\Lambda,0}}} \tag{1.8}$$

and then inverting to find $a(t)$, which is plotted in Fig. 1.1(b). The result, however, is reasonably approximated by the solutions in the single-component cases. In the initial radiation-dominated era, the scale factor grew as roughly $a \propto t^{1/2}$. As a grew above roughly 10^{-4}, matter came to dominate the energy density and the growth quickened to $a \propto t^{2/3}$. We are currently witnessing another transition to a Λ-dominated universe, in which the growth will continue with an $a \propto e^{Ht}$ dependence.

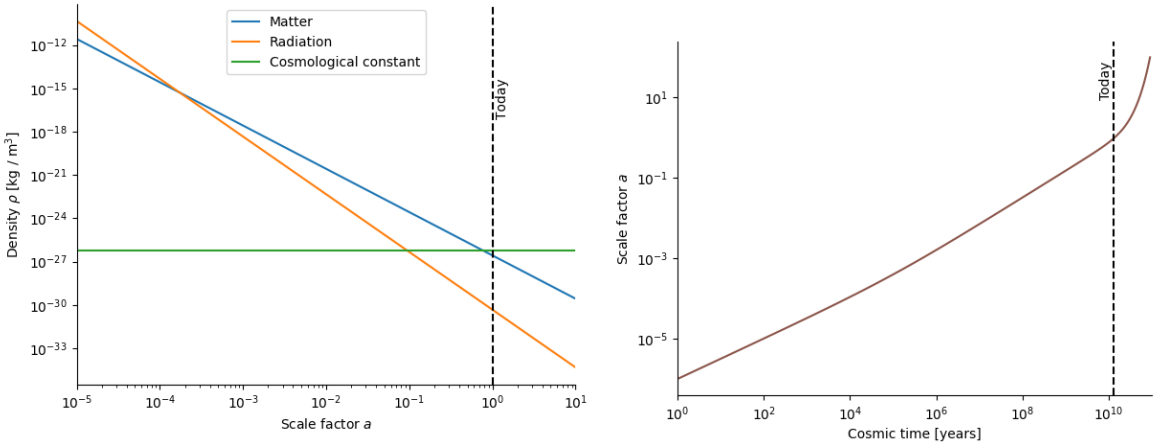

(a) (b)

Figure 1.1: (a) The dilution of the energy density of each cosmic inventory component with expansion, and (b) the evolution of the scale factor in the ΛCDM universe.

Since the $a(t)$ relationship is monotonic, one may use the scale factor as a measure of cosmic time. It is also often convenient to specify cosmic time in terms of the *cosmological redshift*

$$z = \frac{\lambda_{obs} - \lambda_{emit}}{\lambda_{emit}} \tag{1.9}$$

that an observer would determine from measuring radiation emitted at wavelength λ_{emit} from a distant comoving source and detected at λ_{obs}. The relationship between the scale factor and redshift is simple:

$$a = \frac{1}{1+z} \tag{1.10}$$

Supplementing the evolution of the scale factor with knowledge from other areas of physics about what happens to matter as a function of density, we may form a more detailed picture of the evolution of the cosmos. For example, neutrinos should have decoupled from the primordial plasma around $z \sim 10^7$, forming the cosmic neutrino background. The light nuclei were subsequently formed at roughly $z \sim 10^6$, and the observed relative abundances of elements matches very well with theoretical calculations. Later at $z \sim 10^3$, electrons and nuclei formed neutral atoms, enabling photons to begin free streaming to form what is now today the cosmic microwave background (CMB). Re-ionization of the neutral gas formed during recombination due to UV radiation emitted from the first stars occurred much later at $z \sim 6$.

1.2 Deviations from uniformity

The inhomogeneities that we observe in the universe, at least on sufficiently large scales, can be treated as small perturbations $h_{\mu\nu}$ on top of the background metric of (1.1):

$$g'_{\mu\nu} = g_{\mu\nu} + h_{\mu\nu}. \tag{1.11}$$

In general, $h_{\mu\nu}$ may be conveniently decomposed into a sum of scalar, vector, and tensor components whose equations for evolution are decoupled. Of these, only the scalars and tensors are of cosmological significance, as the vectors decay with cosmic expansion.

It is possible to solve for the evolution of metric perturbations given known energy contents (e.g. baryonic matter, dark energy, photons) and initial conditions for $h_{\mu\nu}$, or from an observational point of view surmise the initial conditions based on observations of the time-evolved perturbations (e.g. via galaxy surveys or CMB observations). Modern observations are consistent with the initial conditions consisting only of scalar perturbations $s(\vec{k})$ which are Gaussian and adiabatic[2] so that $\langle s(\vec{k})\rangle = 0$ and that they are fully characterized by their two-point function

$$\langle s(\vec{k}) s^*(\vec{k'})\rangle = (2\pi)^3 P_s(k) \frac{\delta^3(\vec{k} - \vec{k'})}{k^3}. \tag{1.12}$$

The dimensionless power spectrum $P_s(k)$ is consistent with a simple power law:

$$P_s(k) = A_s \left(\frac{k}{k_*}\right)^{n_s - 1} \tag{1.13}$$

for a pivot scale k_* usually chosen to be $k_* = 0.05$ Mpc^{-1}. As indicated by the current measured value in Table 1.2, the primordial scalar perturbations appear to be nearly scale-free (i.e. $P_s(k)$ is nearly independent of k). While evidence of primordial tensor perturbations has not been measured, one may parameterize their power spectrum similarly

$$P_t(k) = A_t \left(\frac{k}{k_*}\right)^{n_t} \tag{1.14}$$

and relate its amplitude to the scalars via

$$r \equiv \frac{P_t(k_*)}{P_s(k_*)}. \tag{1.15}$$

In principle, n_s and n_t may themselves be functions of k, though the current data do not suggest this to within errors. Furthermore, to improve constraining power, constraints on r

[2]Meaning that all components present at the time fluctuated up and down simultaneously. A different scenario might involve isocurvature perturbations where fluctuations in, for example, the matter density could be anticorrelated with fluctuations in, for example, the radiation density.

are often performed assuming scalar invariance of the tensors ($n_t = 0$).[3] The current upper bound on r is also listed in Table 1.2.

Parameter	Value
$\ln(10^{10}A_s)$	3.043 ± 0.014
n_s	0.9652 ± 0.0042
r	< 0.044 (95% confidence)

Table 1.2: Current constraints on primordial scalar [1] and tensor [3] perturbation power spectra, assuming a scale-independent n_s and the single-field consistency relation $n_t = -r/8$.

The physical mechanism responsible for the seeding of the initial perturbation spectra is of course a subject of great interest. Multiple possibilities may yet be possible, but the most theoretically compelling, widely accepted theory that is broadly consistent with the data is that of cosmic inflation, discussed further in Section 1.4.1.

The initial adiabatic scalar perturbations in the metric correspond to density fluctuations, which over cosmic history have led to the formation of the structures we see today via gravitational instability. At the scale of individual galaxies, the nonlinear nature of gravity and additional processes resulting from the high density of baryonic matter causes the linear perturbative treatment to break down. On much larger distance scales, however - such as those that can be probed by surveys of many many galaxies whose positions trace the underlying dark matter distribution or by the cosmic microwave background anisotropies - the linear treatment works remarkably well and may be used for cosmological inference.

1.3 The cosmic microwave background

As the early universe expanded and cooled, by redshift $z \simeq 1100$ all the electrons and nuclei had combined to form neutral gas, allowing photons to begin free streaming. Immediately before this period of so-called *recombination*, photons were tightly thermally coupled to the plasma, so their spectral distribution upon emission was that of a blackbody at the plasma temperature $T \simeq 3 \times 10^3$ K. Because of the expansion of spacetime throughout their journey to us, the photons we can observe today have been redshifted to now follow a blackbody distribution of $T = 2.7255 \pm 0.0006$ K [4]. Because this distribution peaks at $\nu = 160$ GHz the photon background is called the *cosmic microwave background* (CMB).

The CMB is for the most part uniform across the sky, but small deviations from isotropy exist and have been measured. The largest of these is a dipole pattern with an amplitude of $3.36208 \pm 0.00099\ \mu K_{\rm CMB}$ and is interpreted as the Doppler shifting of the monopole due to our peculiar velocity of $v = 369.82 \pm 0.11$ km/s with respect to the CMB rest frame [5].

[3] Another convention in use (as in [2]) is to fix n_t using the single-field slow-roll consistency relation (1.35).

Higher order multiploles, however, are mainly the result of perturbations in the density of the universe, encoded into the radiation pattern during the *epoch of last scattering* as photons decoupled from the primordial plasma. The resulting fluctuations in the intensity of the CMB are roughly 1 part in 10^5. Because quadrupolar anisotropies at last scattering generated linear polarization, the CMB also has linearly polarized anisotropies at about 5% of the level of the intensity anisotropies.

Several post-processing mechanisms also contribute to the CMB that we observe today. After emission, CMB photons can be gravitationally redshifted due to the integrated Sachs-Wolfe effect. Additional photon-electron scattering happened as Thompson scattering after the universe reionized and as inverse Compton scattering inside galaxy clusters via the Sunyaev-Zeldovich effect. Furthermore, gravitational lensing of the CMB by intervening cosmic structures deflects the apparent angles of the observed radiation.

CMB experiments typically determine the polarization state of the CMB radiation using intensity measurements only, for which the *Stokes parameters* are useful:

$$\begin{aligned} I &\equiv \langle E_x^2\rangle + \langle E_y^2\rangle && (1.16)\\ Q &\equiv \langle E_x^2\rangle - \langle E_y^2\rangle && (1.17)\\ U &\equiv \langle E_a^2\rangle - \langle E_b^2\rangle && (1.18)\\ V &\equiv \langle E_r^2\rangle - \langle E_l^2\rangle && (1.19)\\ & && (1.20) \end{aligned}$$

where the (a, b) coordinate basis is defined by $\hat{a} = (\hat{x} + \hat{y})/\sqrt{2}$ and $\hat{b} = (-\hat{x} + \hat{y})/\sqrt{2}$ and the (l, r) coordinate basis is defined by $\hat{l} = (\hat{x} + i\hat{y})/\sqrt{2}$ and $\hat{r} = (\hat{x} - i\hat{y})/\sqrt{2}$. I measures the total intensity of the radiation, Q and U measure linear polarization, and V measures circular polarization.

The Stokes parameters measured by the instrument are a function of the angle on the celestial sphere $\hat{n}$, so a harmonic decomposition can be done in terms of the spherical harmonic functions $Y_{\ell m}(\hat{n})$ and the spin-weighted spherical harmonic functions ${}_{\pm 2}Y_{\ell m}(\hat{n})$:

$$\begin{aligned} I(\hat{n}) &= \sum_{\ell,m} a_{T,\ell m} Y_{\ell m}(\hat{n}) && (1.21)\\ (Q \pm iU)(\hat{n}) &= \sum_{\ell,m} (a_{E,\ell m} \mp a_{B,\ell m})_{\mp 2} Y_{\ell m}(\hat{n}) && (1.22)\\ V(\hat{n}) &= 0 && (1.23) \end{aligned}$$

where the final relation is typically assumed because circular polarization is not expected from Thompson scattering. Current limits are indeed consistent with zero circular polarization [6].

The scalar $a_{T,\ell m}$ and $a_{E,\ell m}$ and pseudoscalar $a_{B,\ell m}$ modes are predicted to be Gaussian in most theories, but because of isotropy, the angular power spectrum

$$C_\ell^{XY} \equiv \frac{1}{2\ell + 1} \sum_m \langle a_{X,\ell m} a_{Y,\ell m}^* \rangle \quad (1.24)$$

is a more useful quantity. Experiments typically measure (binned) angular power spectra for comparisons to theory.

A compilation of recent power spectrum measurements and the best fit theoretical model is shown in Figure 1.2. The TT spectrum is by far the largest in amplitude, and at the largest angular scales ($\ell \lesssim 100$) is dominated by contributions from the Sachs-Wolfe and integrated Sachs-Wolfe effects. At intermediate angular scales ($100 \lesssim \ell \lesssim 1000$), the TT, TE, and EE spectra are dominated by the so-called acoustic peaks, a consequence of acoustic oscillations in the photon-baryon fluid prior to recombination. At the smallest angular scales ($\ell \gtrsim 1000$), the TT and EE spectra die off because the recombination process was not instantaneous and partially erased information about the smallest angular scales. The BB power spectrum is dominated by gravitationally lensed primordial E-modes, as scalar perturbations in the early universe do not source B-modes at linear order. As discussed in Section 1.4.1, the BB power spectrum may also contain a potentially measurable contribution from primordial tensor perturbations.

In addition to the temperature and polarization anisotropy angular power spectra, the gravitational lensing of the CMB by intervening cosmic structure offers an additional signal channel to measure. Schematically, the process of lensing remaps the measured Stokes parameters from their unlensed position $\hat{n}$ on the sky to a lensed position $\hat{n} + \vec{d}(\hat{n})$:

$$I(\hat{n}) \rightarrow I(\hat{n} + \vec{d}(\hat{n})) \tag{1.25}$$

$$(Q \pm iU)(\hat{n}) \rightarrow (Q \pm iU)(\hat{n} + \vec{d}(\hat{n})). \tag{1.26}$$

Equations (1.25) and (1.26) are exact in the flat-sky limit, but for the real curved sky the vector $\hat{n} + \vec{d}(\hat{n})$ denotes a new vector at a distance $|\vec{d}|$ away from $\hat{n}$ along a geodesic in the direction of $\vec{d}$. The pseudo-vector $(Q \pm iU)$ must also be parallel transported. The deflection vector is to lowest order the gradient of the scalar lensing potential

$$\vec{d} \simeq \nabla\phi \tag{1.27}$$

which measures the line-of-sight projection of the gravitational potential. Because gravitational lensing is a nonlinear operation, higher-order products of the T, E, and B fields may be used to reconstruct the lensing potential ϕ. With a harmonic decomposition similar to (1.21), the CMB lensing power spectrum $C_\ell^{\phi\phi}$ measures a 2-dimensional projection of the 3-dimensional matter power spectrum. Recent measurements of the lensing spectrum are also shown in the bottom panel of Figure 1.2.

When considering actual measurements of the angular power spectra, there is a fundamental limit to the uncertainty of such measurements. Because the $a_{\ell m}$ coefficients are Gaussian distributed, each C_ℓ is χ^2 distributed with $(2\ell+1)$ degrees of freedom. Additionally, experiments will practically only measure the CMB over a fraction $f_{sky} < 1$ of the total celestial sphere, reducing the number of modes useful for averaging down the noise. Together, these produce the *cosmic variance limit* for angular power spectrum measurements:

$$\Delta C_\ell \approx \sqrt{\frac{2}{(2\ell+1) f_{sky}}} C_\ell. \tag{1.28}$$

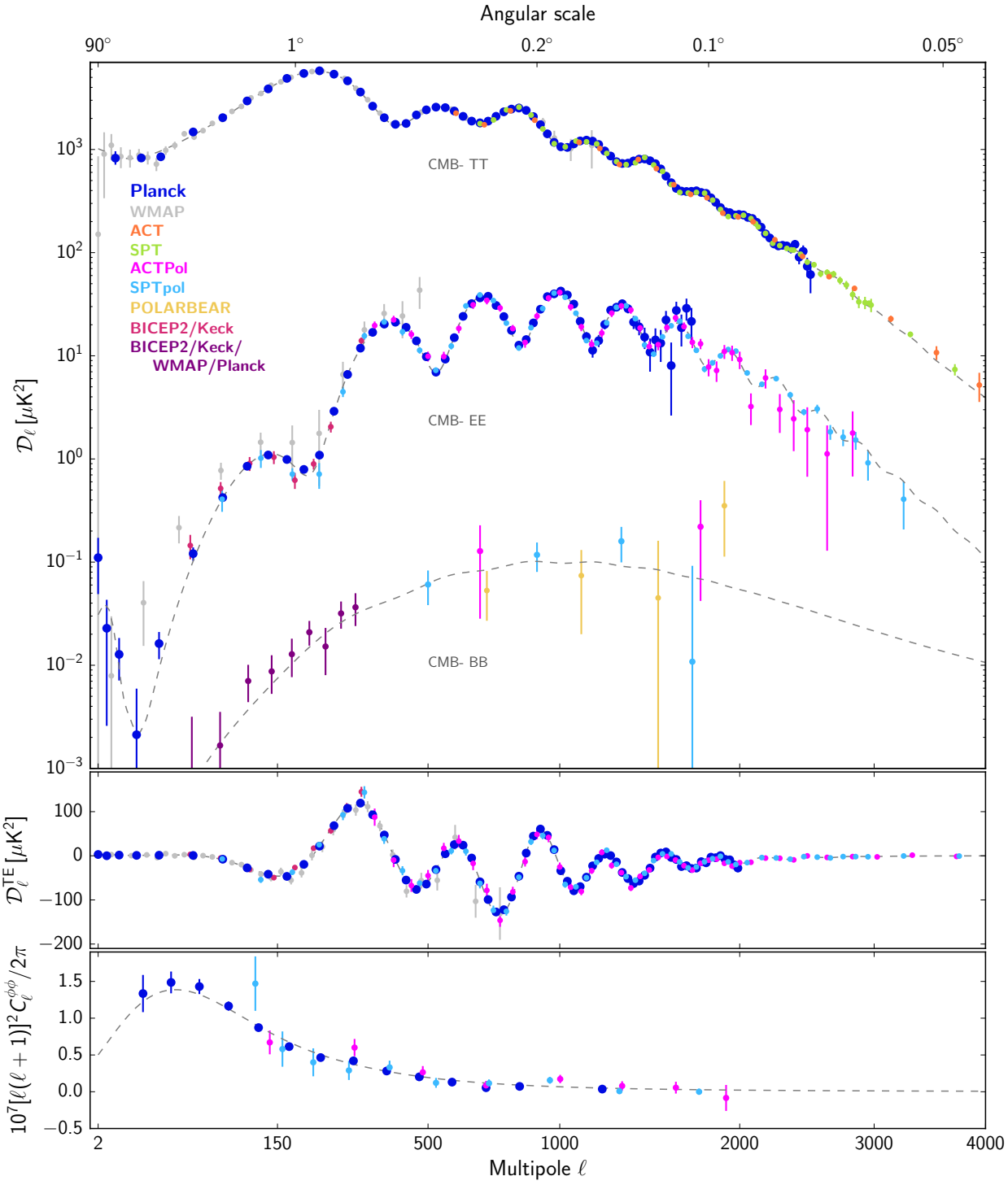

Figure 1.2: A compilation of recent CMB power spectra measurements from [1].

The CMB temperature power spectrum has already been measured to within cosmic variance over most cosmologically relevant angular scales; much more room for improved precision remains in the CMB polarization and CMB lensing.

1.4 Signatures of fundamental physics in the CMB

The large-scale properties of the universe are extremely well-described by (i) a perturbed Friedmann-Robertson-Walker spacetime metric and (ii) a spacetime filled primarily with a cosmological constant Λ and cold dark matter. Together, these are encapsulated in the *ΛCDM model*, a remarkable success of modern cosmology. With only 6 free parameters, it is able to describe all measurements to date to within errors. Nevertheless, with improved precision from future measurements several extensions to ΛCDM which are either expected to exist due to known physical processes or postulated to exist for theoretically interesting reasons are the focus of upcoming observational efforts. Two of these - the primary science targets of the Simons Array - are described here.

1.4.1 Inflation

The leading theoretical paradigm for the mechanism behind the initial conditions of the ΛCDM universe is that of *cosmic inflation*. Inflation simultaneously offers natural explanations for the observed lack of curvature (i.e. why $k \simeq 0$ in (1.1)), the uniformity of the CMB on scales much larger than the comoving horizon at recombination,[4] and the spectrum of primordial perturbations of the Friedmann-Robertson-Walker spacetime. While there are alternatives to the inflationary paradigm - notably bouncing and cyclic cosmologies - it is difficult to construct an alternative theory which simultaneously agrees with all the observational data in hand, leading to the modern popularity of inflation. The story is far from finished, however, with many questions remaining. If inflation is the correct paradigm, then it remains to be seen what microphysical theory gives rise to the inflaton field, as well as how many fields were involved. One promising probe which stands to shed light on these questions comes from the generic prediction of inflationary models that tensor perturbations were produced in the early universe, signatures of which may be measurable in the CMB.

The basic idea of inflation is that one or more scalar fields dominated the energy density of the early universe. To illustrate the concept here, the example of single-field slow-roll inflation is chosen. In this case, a canonical scalar field ϕ with self-interaction potential $V(\phi)$ which is mostly uniform in space dominates the energy density in the very early universe. In the homogeneous and isotropic background solution, the perfect fluid formed by the inflaton

[4] These are often referred to the "horizon" and "flatness" problems.

field has density and pressure

$$\rho = \frac{1}{2}\dot{\phi}^2 + V(\phi) \tag{1.29}$$

$$p = \frac{1}{2}\dot{\phi}^2 - V(\phi). \tag{1.30}$$

If V dominates and is approximately constant in time for some period, then $\rho = -p$ and (1.4) implies that $a(t) \propto e^{Ht}$ where $H = \sqrt{8\pi G_{\rm N}\rho/3}$. The resulting accelerating expansion dilutes away curvature and modifies the cosmological horizon, avoiding the fine-tuning issues of the horizon and flatness problems. The potential V can be the dominant contributor to the energy density under the "slow roll" condition in which the slow-roll parameters

$$\epsilon \equiv \frac{M_{\rm pl}^2}{16\pi}\left(\frac{V'}{V}\right)^2, \qquad \eta \equiv \frac{M_{\rm pl}^2}{8\pi}\left(\frac{V''}{V}\right) \tag{1.31}$$

satisfy $\epsilon \ll 1$ and $|\eta| \ll 1$ (where primed quantities denote derivatives with respect to the field value). Nevertheless, the inflationary epoch must eventually end; once the field value approaches its minimum, it decays into Standard Model (or precursor) particles in a process usually called *reheating*.

Quantum mechanical fluctuations in the inflaton field cause inflation to end at slightly different times at different locations, resulting in perturbations in the spacetime metric. These fluctuations provide a natural mechanism for the initial conditions of the ΛCDM universe. In the single-field slow-roll case, the parameters in the power spectra (1.13) and (1.14) are predicted in terms of the slow-roll parameters:

$$n_s \simeq 1 - 6\epsilon + 2\eta \tag{1.32}$$

$$r \simeq 16\epsilon \tag{1.33}$$

$$n_t \simeq -2\epsilon. \tag{1.34}$$

The fact that the observed value of n_s is less than 1 already is very suggestive of inflation in the early universe. Additionally, in the single-field case, (1.33) and (1.34) together imply the consistency relation

$$n_t = -\frac{r}{8} \tag{1.35}$$

which is modified in the multi-field case and may be useful to distinguish between single- and multi-field inflation in the case of the detection of tensor perturbations. A measurement of the tensor spectral index n_t will likely be very difficult, however, given that r is already constrained to be small. For large values of r that are no longer feasible given current constraints, the impact of primordial tensors will affect the temperature and E-mode power spectra. The tensor-to-scalar ratio r may still be measurable via a small excess in B-modes in the CMB polarization around $\ell < 10$ and also $\ell \sim 100$, as shown in Figure 1.3. The $\ell < 10$ excess is due to scattering after reionization so is called the "reionization bump",

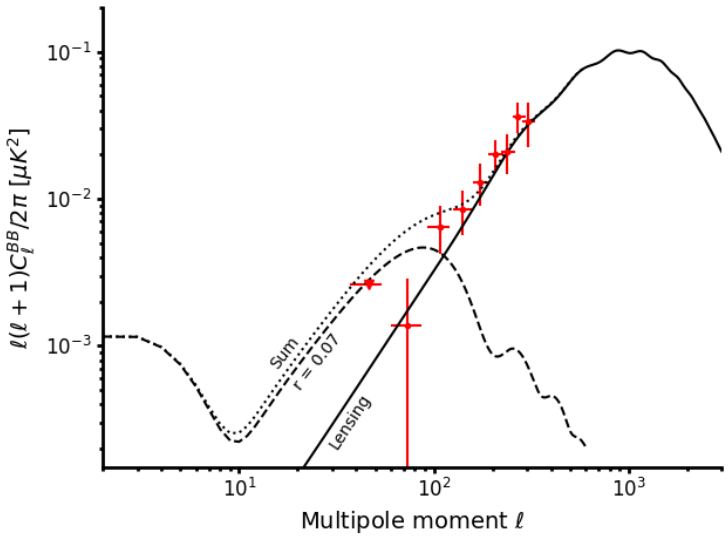

Figure 1.3: Theoretical curves for the angular power spectra of lensing B-modes and a possible tensor B-mode component, along with the measurement from BICEP2 and the Keck array which gives individually the best constraint on the value of r. The theory curves were simulated by the CAMB software package [7] and use the best-fit cosmological parameters from [1] and the upper limit of r from CMB B-modes alone [8].

while the $\ell \sim 100$ excess is due to scattering at the last scattering surface so is called the "recombination bump".

A detection of primordial tensor perturbations would give a very high energy probe of new physics. The value of the inflaton potential during inflation is related to the tensor-to-scalar ratio via

$$V^{1/4} = 10^{16}\ \text{GeV} \left(\frac{r}{0.01}\right)^{1/4}, \tag{1.36}$$

and may be many orders of magnitude above the energies accessible by modern particle colliders. A non-detection from upcoming CMB experiments is still of interest, however. Integrating over the number of e-foldings N_* by which the scale factor increased during the inflationary epoch, the field range traversed by the inflaton is

$$\frac{\Delta\phi}{M_{\text{pl}}} = \int_0^{N_*} \left(\frac{r}{8}\right)^{1/2} dN. \tag{1.37}$$

Given the minimum N_* required to solve the horizon problem, a sufficiently powerful upper limit on r can strongly disfavor inflation models in which the inflaton traverses a super-Planckian field range.

1.4.2 Neutrino masses

Particle physics experiments have solidly established that there are (at least) 3 neutrino species, two or more of which must have nonzero mass. Their massive nature in particular technically requires an addition to the Standard Model, and has the potential to be quite interesting. For instance, if the masses are generated by the Mayorana mechanism, there are theoretically compelling explanations - via the see-saw mechanism and leptogenesis - for the relative smallness of the neutrino masses compared to all the other Standard model masses and also the observed matter-antimatter symmetry in the universe.

Notably, the neutrino flavor and mass eigenbases are not coincident, giving rise to flavor oscillation phenomena. From a variety of neutrino flavor oscillation experiments which are sensitive to the squared mass splittings $\Delta m_{ij} \equiv m_i^2 - m_j^2$, the parameters Δm_{21}^2, $|\Delta m_{31}^2|$, and $|\Delta m_{32}^2|$ have been measured, with $\Delta m_{21}^2 \ll |\Delta m_{31}^2| \simeq |\Delta m_{32}^2|$. From these observations, two neutrino mass eigenstate orderings are possible:

$$\text{Normal}: \quad m_1 < m_2 < m_3 \tag{1.38}$$

$$\text{Inverted}: \quad m_3 < m_1 < m_2 \tag{1.39}$$

However, the absolute scale of the neutrino masses is currently unmeasured. The absolute neutrino mass scale is an important input towards determining the nature of neutrinos,[5] and may be measured via both laboratory[6] and cosmological methods.

Cosmological measurements, in particular, are sensitive to the total mass in neutrinos.[7] From well-understood Standard Model physics which accounts for the particle degrees of freedom between the energy scales at which neutrinos and photons decouple from the primordial plasma, their energy densities are related by a calculable constant

$$\frac{\rho_\nu}{\rho_\gamma} = \frac{7}{8} N_{\text{eff}} \left(\frac{4}{11}\right)^{4/3} \tag{1.40}$$

where $N_{eff} = 3$ is the number of neutrino species in the idealized case that neutrino decoupling is instantaneous. A more careful calculation taking into account the extended decoupling time and its relationship to the $e^+e^- \to \gamma$ conversion happening nearby in cosmic time, flavor oscillations, etc. yields the Standard Model expectation of 3.045 [9]. This calculation, along with a knowledge of n_γ from the CMB, also produces a number density n_ν of neutrinos.

As cosmic expansion proceeds and the neutrinos become nonrelativistic, because the number densities for each species are approximately equal, the total number density n_ν

[5] Neutrinoless double beta decay searches, CP-violation searches, and a determination of the mass ordering are others

[6] By precisely measuring the endpoint of the electron energy spectrum resulting from β-decay

[7] Whereas β-decay measurements are sensitive to the effective electron neutrino mass $\sum_{i=1}^{3} m_i |U_{ei}|$, where U is the neutrino mixing matrix

factors out:[8]

$$\rho_\nu = \sum_{i=1}^{3} m_i n_i \approx n_\nu \sum_{i=1}^{3} m_i. \tag{1.41}$$

Usually the sum in the last relation is written as $\sum m_\nu$ for convenience. The relative density of neutrinos in the universe is then

$$\Omega_{\nu,0} = \frac{\rho_{\nu,0}}{\rho_{crit,0}} = \frac{\sum m_\nu}{42.3 \text{ eV}} \tag{1.42}$$

and is bounded from below by the minimum mass configuration: $\Omega_{\nu,0} \gtrsim 0.0013$. In short, because the number densities of the neutrino species are heavily constrained by various cosmological considerations, a measurement of the total energy density in neutrinos may be converted into a measurement of the individual particle masses.

Neutrinos are the only known particle that contributes to the radiation density in the early universe and later to the matter density. Specifically, they become nonrelativistic as they cool below $T_\nu^{\text{nonrel}} = m_i/3.15$, and afterwards still travel at a greater speed than the cold dark matter with a free-streaming length of $v/c = 3.15 T_\nu/m_i$. For future cosmological constraints of $\sum m_\nu$, the most relevant method in which neutrinos affect cosmological observables is via the clustering of matter. Specifically, above the free streaming length, neutrinos contribute to structure formation, while below they do not. Additionally, both above and below the free streaming length, after the neutrinos become nonrelativistic they contribute to the background matter density on which the evolution of cold dark matter density inhomogeneities depends.

Neutrinos, then, modify the power spectrum of matter density fluctuations in a way that depends on $\sum m_\nu$. The CMB therefore is sensitive to $\sum m_\nu$ via the lensing power spectrum, which is essentially a 2D projection of the 3D matter power spectrum. This effect is demonstrated in Figure 1.4 for a range of neutrino masses and compared to the sensitivity of a possible configuration of the future CMB-S4 experiment.

1.5 Measurement strategies and challenges

To achieve maximum sensitivity, CMB experiments typically observe a fraction of the sky for as long as is practical.[9] The size of the survey patch on the sky is determined partially by the measurement requirements. Schematically, the precision with which a power spectrum C_ℓ may be measured is determined by the interplay between cosmic variance ΔC_ℓ^{CV} and

[8] It could still be the case that one neutrino is massless or approximately massless and therefore still relativistic, but even then the above relationship (1.41) is still approximately true.

[9] For a satellite experiment, this may be on the order of a decade. For a balloon experiment, it may be closer to several weeks. For a ground-based telescope, it may be on the order of several years.

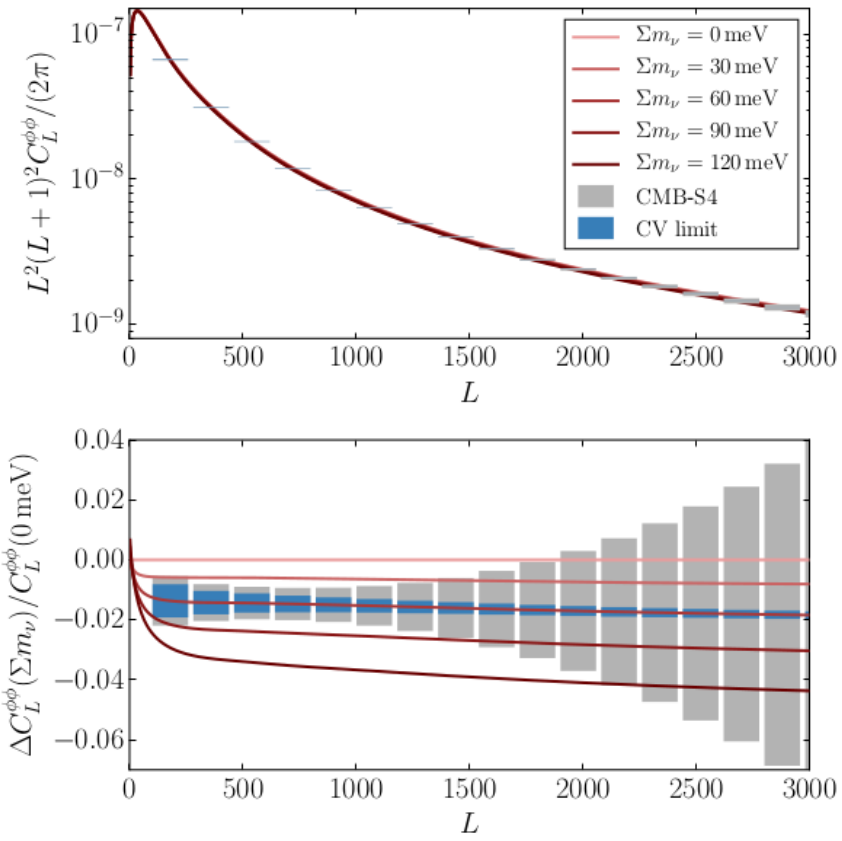

Figure 1.4: The effect of the sum of neutrino masses on the CMB lensing power spectrum, along with the cosmic variance and projected instrumental sensitivity for the CMB-S4 experiment for a fiducial value of $\sum m_\nu = 60$ meV from [10].

instrumental noise N_ℓ:

$$\Delta C_\ell^{tot} = \Delta C_\ell^{CV} + N_\ell \tag{1.43}$$

$$= \sqrt{\frac{2}{(2\ell+1)f_{sky}}} C_\ell + f_{sky} w_\ell^2 \tag{1.44}$$

where w_ℓ encapsulates the instantaneous sensitivity of the instrument, accounting for the various sources of time-domain noise and the angular resolution of the experiment. In the high S/N limit where $C_\ell \gg w_\ell^2$ (e.g. in the case of a N_{eff} measurement), the first term dominates and $\Delta C_\ell^{tot} \propto f_{sky}^{-1/2}$, driving one to survey as much of the sky as possible. In the low S/N limit where $C\ell \ll w_\ell^2$ (e.g. in the case of an upper limit on r), the second term dominates and $\Delta C_\ell \propto f_{sky}$, driving one to choose a smaller patch of the sky.[10]

[10]This picture becomes inexact as soon as many realistic complications enter - the presence of foregrounds and gravitational lensing noise, the need for a sky patch larger than the angular scale of interest, the existence

CMB instruments are typically either constructed on satellites, high-altitude balloons, or ground-based telescopes. Since the Earth's atmosphere is not completely transparent in the microwave regime, there are sensitivity and stability benefits associated with satellite and balloon measurements. Ground-based telescopes are typically located at high altitude and in dry, stable climates to minimize the negative effects of the atmosphere on their observations.[11] From the ground, experiments are able to take advantage of newer technologies without the risks associated with rocket launches and balloon flights while also incorporating larger reflectors which allow for high angular resolution.

The existence of microwave emission from sources other than the CMB presents a major design consideration for CMB measurements, especially those designed to measure large angular scales. Galactic foregrounds are most problematic for CMB measurements, and for the low-ℓ polarization measurements that are a major focus in the field give rise to two primary sources: polarized thermal emission from spinning dust grains and synchrotron radiation. Both are highly dependent on galactic latitude, so to avoid foreground contamination it is desirable to choose a survey area in a relatively "clean" part of the sky. At high galactic latitudes, the polarized dust and synchrotron emission may be crudely approximated by power laws in ℓ [11], [12]:

$$\frac{\ell(\ell+1)}{2\pi}C_\ell^{dust} \propto \ell^{-2.42} \tag{1.45}$$

$$\frac{\ell(\ell+1)}{2\pi}C_\ell^{sync} \propto \ell^{-0.6} \tag{1.46}$$

and are shown in Figure 1.5(a). A measurement of the frequency dependence of their emission is also shown in Figure 1.5(b). The general strategy followed by current and future experiments is to exploit the strong spectral distinctions between the CMB and polarized foregrounds. By observing in multiple frequency bands, component separation techniques may be employed which significantly mitigate foreground contamination.

Another challenge for inflation searches in the CMB polarization is that the sensitivity is partially limited by the presence of lensing B-modes. To extend the reach of future experiments to smaller and smaller values of r, the removal of lensing B-mode power from the measured maps via a process called *delensing* must be used [13, 14, 15]. In short, by combining a measurement of E-modes (the source) with a measurement of cosmic structure (the lens), one can undo the lensing operation and gain additional sensitivity to primordial B-modes. Since gravitational lenses is nonlinear and mixes angular scales, this puts a requirement of high angular resolution (either internally or from a separate survey on the same patch of sky) on CMB experiments. While there are multiple ways to measure the lensing potential, using the CMB polarization itself is expected to be the most sensitive technique in the long-term [16].

of atmospheric and instrumental 1/f noise, etc.

[11] The two most popular observing sites are the Atacama Desert in Chile and the geographic South Pole, though others - such as Mauna Kea, the Canary Islands, and the Tibetan Plateau - have also received attention.

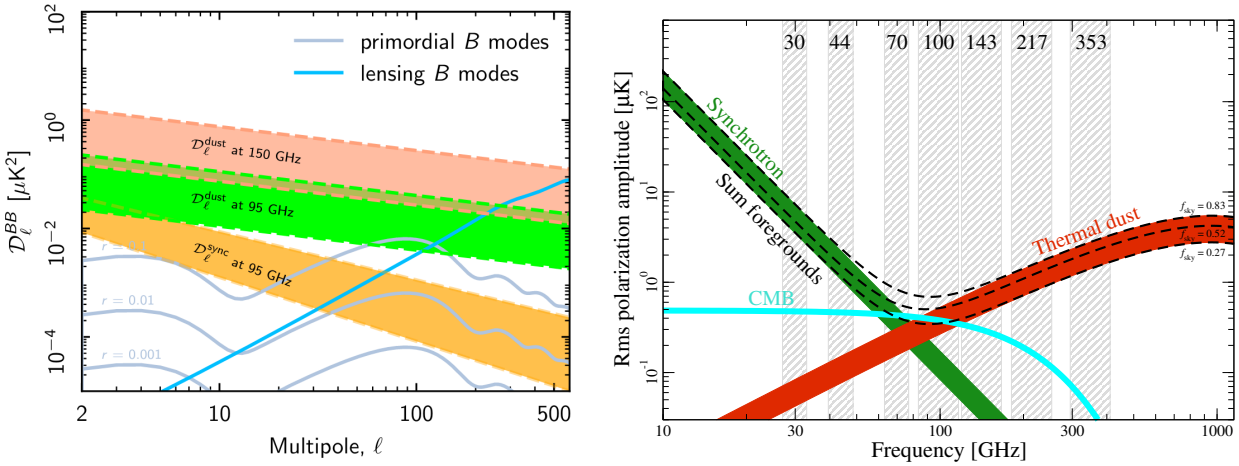

Figure 1.5: The spatial and spectral dependences of foregrounds as measured by the Planck satellite. (a) shows the dust and synchrotron B-mode power at 95 and 150 GHz for a range of fractional sky coverages [11]. (b) shows the RMS amplitude of $P = \sqrt{Q^2 + U^2}$ at high galactic latitudes, smoothed at 40 arcminute scales, for a range of fractional sky coverages [5]. The CMB component drops off at high frequencies because of the use of Rayleigh-Jeans units.

1.6 State of the field

The state-of-the-art for most CMB anisotropy imaging comes from the recent cosmology survey of the Planck satellite [5]. At the high-ℓ and high-sensitivity[12] frontiers, a variety of ground- and balloon-based instruments have continued to make improved measurements. Recent high-sensitivity instruments focused on measuring large angular scales have included the BICEP/Keck family of instruments [17], SPIDER [18], and CLASS [19] experiments. At smaller angular scales, several generations of cameras fitted in the Atacama Cosmology Telescope and South Pole Telescope have pushed the sensitivity at high-ℓ, most recently with the Advanced ACTPol [20] and SPT-3G [21] cameras. Occupying the overlap between these two are the POLARBEAR [22] and Simons Array [23] instruments. Further afield, a variety of near-term and long-term experiments are at various stages of design and construction including the BICEP Array [24], AliCPT [25], the Simons Observatory [26], CCAT-prime [27], CMB-S4 [28], and LiteBIRD [29].

Constraints on inflation are now in the regime where the CMB B-mode channel is the most important for sensitivity. Using this channel in isolation, the most stringent upper bound is $r < 0.072$ [8], though can be tightened to $r < 0.044$ with the addition of T and E information [3]. Current B-mode searches are also quickly becoming lensing-limited; the

[12] That is, where cosmic variance does not already dominate the measurement uncertainty

first demonstration of a reduction of uncertainty on r was recently shown [30], and similar analyses are likely to become standard in the figure. The next several generations of CMB experiments should be able to detect or rule out $r \gtrsim 0.001$, basically covering the entire parameter space of large-field models [10].

Cosmological constraints on neutrino masses are approaching interesting territory as well. By combining data from the CMB, tracers of large scale structure, and the background evolution of the scale factor, a limit of $\sum m_\nu < 0.11$ eV may be made [1]. Comparing this to the lower bounds of 0.06 eV in the case of the normal mass ordering and 0.11 eV in the case of the inverted mass ordering suggests that either a detection or a cosmological measurement of the mass ordering is in the near future. Depending on the value of $\sum m_\nu$, it may be measured by near-term CMB experiments, but in the longer term the CMB-S4 experiment expects to be able to measure even the minimum allowable value of 0.06 eV with high significance [10]. It is important to note that CMB lensing measurements of $\sum m_\nu$ must be combined with other measurements to break parameter degeneracies, most notably with the optical depth to reionization τ and the present-day value of the Hubble parameter H_0. In particular, an improved measurement of τ may come from CLASS [31] or LiteBIRD [29], and H_0 could come from DESI [32]. In the case that τ is measured to its cosmic variance limit,[13] future ground-based CMB measurements could achieve a one-sigma sensitivity as low as $\sigma(\sum m_\nu) \lesssim 15$ meV [10].

[13] via the CMB, that is - it may in principle be measured to better precision via the 21-cm hyperfine transition [33]

Chapter 2

The Simons Array Experiment

The scientific prospects of cosmic microwave background anisotropy studies have given rise to a healthy industry of ground-based imaging experiments that have been increasing in sensitivity at an astounding rate. The capabilities of these experiments are largely determined by their raw sensitivities, the range of accessible angular scales, and their ability to separate astrophysical foreground emission from cosmological signals. This chapter introduces the Simons Array, a new cosmic microwave background polarization experiment now coming online in the Chilean Atacama desert which pushes on all three of these measurement driving fronts relative to its predecessor experiment, POLARBEAR. An overview of the Simons Array design is given here, though the reader is directed to Chapters 3–4 for further details on the detector and readout technologies and Chapter 5 for details on the installation of the first Simons Array telescope in Chile.

2.1 Overview

The Simons Array is a ground-based telescope array, designed to measure the CMB polarization anisotropies from its observing site in northern Chile. It consists of three telescopes, pictured in Figure 2.1, and builds on the heritage of the POLARBEAR experiment [22], which operated from the same observing site from 2012–2017. As a nod to their predecessor, the three Simons Array instruments are also referred to as POLARBEAR-2a, POLARBEAR-2b, and POLARBEAR-2c.

A defining feature of the Simons Array is that it is designed for simultaneous sensitivity to angular scales relevant for CMB lensing measurements and those relevant for constraints of inflationary B-modes at the recombination bump. In particular, the Simons Array targets a constraint on or measurement of the inflationary tensor-to-scalar ratio r via B-mode measurements above $\ell \sim 50$ and a constraint or measurement of the sum of neutrino masses $\sum m_\nu$ via a measurement of the CMB lensing power spectrum. Furthermore, improved constraints are expected from the Simons Array on the scalar spectral index n_s and the effective number of degrees of freedom in light weakly-coupled particles N_{eff} via the Simons Array's

Figure 2.1: The Simons Array as seen from the West. Photo by Seth Pransky.

ability to measure the EE power spectrum at the resolution of a few arcminutes. Furthermore, as a sensitive CMB polarimeter, the Simons Array should be able to further constrain the exotic physics scenarios of cosmic birefringence and primordial magnetic fields.

The final constraining power that the Simons Array will have for each of these parameters in the ΛCDM model and its extensions will depend on many details not yet realized about each telescope. Nevertheless, some context may be gained via Fisher-based estimates using the instrument design parameters. 1-σ uncertainties on r, $\sum m_\nu$, and n_s have been projected to be 0.006, 40 meV[1], and 0.0015, respectively [23].[2]

An important feature of the Simons Array measurement strategy is the removal of astrophysical foregrounds from the observed sky. To such an end, a total of four observation bands are included so as to spectrally separate polarized foregrounds from the CMB. These bands are located within the windows of atmospheric transmission from the ground and are centered at approximately 95, 150, 220, and 280 GHz, as shown in Figure 2.2. The majority of the sensitivity is focused in the 95 and 150 GHz channels, where the CMB-to-foreground emission ratio is largest. The remaining sensitivity is divided between 220 and 280 GHz,

[1] when combined with DESI BAO

[2] These forecasted parameter constraints correspond to a survey footprint significantly larger than the current baseline footprint, but the level of impact that the survey size has on these forecasts is sub-dominant to uncertainties in assumptions about the instantaneous sensitivity of each telescope and the total observation time of the combined array.

which will primarily measure the (much brighter) polarized dust emission. Additional cross-correlation with external datasets may further improve the foreground removal ability of the Simons Array.

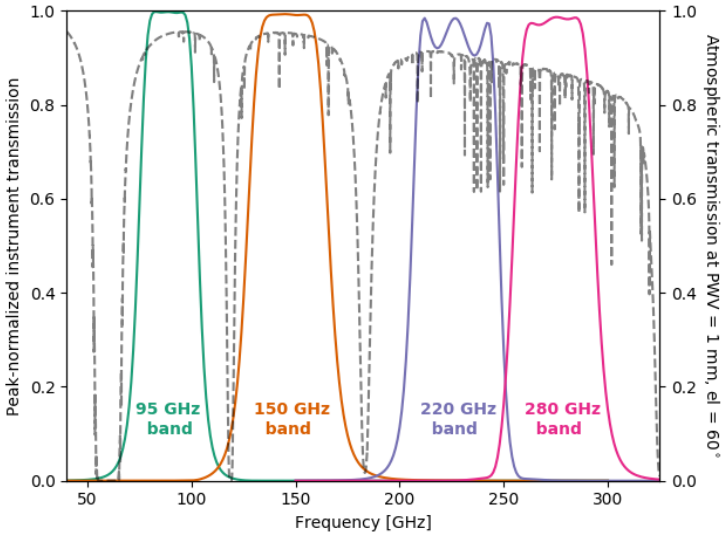

Figure 2.2: Design instrument passbands for the Simons Array, shown on top of the atmospheric transmission from the Chajnantor plateau during good conditions, as modeled by the AM software package [34].

The expected survey area further follows the intent to minimize atmospheric foreground contamination, as the chosen patches overlap minimally with the microwave emission from the galactic disc, demonstrated in Figure 2.3. Most of the survey weight is in the so-called southern galactic hole, which is most readily observed from the telescope site in Chile. The survey patch covers approximately 10% of the sky, and is optimized for cross-correlation with external datasets - in particular, surveys by the Simons Observatory Small Aperture Telescopes [26], the Dark Energy Spectroscopic Instrument [32], and the Hyper Suprime-Cam on the Subaru Telescope [35].

The form factors of the Simons Array instruments themselves are determined largely by the science drivers. To maximize sensitivity to the faint CMB polarization anisotropies, 22,680 individual detectors optically coupled to the sky. These detectors are distributed across three mid-sized instruments. In order to resolve sufficiently small angular scales for CMB lensing measurements, the diameter of the primary reflectors in the imaging optics is 2.5 meters. In order to reject low-frequency fluctuations in the unpolarized atmospheric thermal emission for inflation measurements, continuously rotating polarization modulators are placed in the optical chain of each telescope. The following section describes these instrument aspects in further detail.

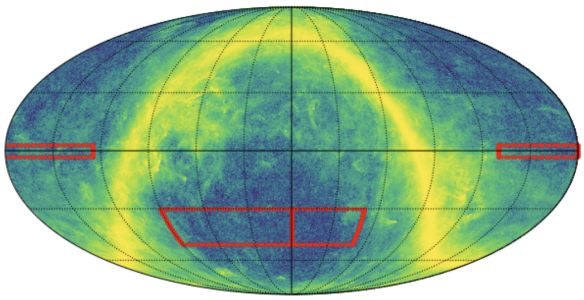

Figure 2.3: Estimated approximate survey footprint for the Simons Array, shown in equatorial coordinates on top of the Planck 353 GHz map to emphasize that relatively dust-free patches of the sky were prioritized to minimize foreground contamination. Figure courtesy of Aashrita Mangu.

2.2 Instrument Design

2.2.1 Observing site and telescopes

The Simons Array observing site is located in northern Chile at an altitude of 5200 m on the slopes of Cerro Toco, approximately 50 km from the town of San Pedro de Atacama. It uses the infrastructure of the preceding POLARBEAR instrument, and is adjacent to several other microwave and sub-mm observatories, as indicated in Figure 2.4.

This observing location has several advantages. First, the high elevation and dry climate together result in high atmospheric microwave transmission. Second, the mid-latitude location of the site in northern Chile provides access to nearly 80% of the sky. Finally, year-round access to the site is relatively convenient, requiring only a commercial flight and a short drive. Other observing sites such as the geographic South Pole and the Tibetan Plateau have received attention for CMB observations, with the South Pole. The South Pole offers more stable atmospheric conditions at the cost of accessibility and sky coverage. The Tibetan Plateau appears quite similar to the Chilean site but only recently has seen infrastructure development for CMB observations [36].

The three Simons Array telescopes are of identical optical design, and incorporate two reflectors arranged in an off-axis Gregorian configuration that satisfies the Mizugutch-Dragone condition, minimizing cross-polarization and giving a diffraction-limited field of view [37], [38], [39]. The illumination pattern on the primary reflector is 2.5 meters in diameter, and the field of view of the system is 4.5 degrees. The FWHM of the instrument illumination pattern on the sky is 3.5 arcminutes at 150 GHz.

The telescope design for the Simons Array comes from that of the POLARBEAR instrument [40], and in fact the third Simons Array instrument, POLARBEAR-2c, will involve re-using the telescope from POLARBEAR, replacing its cryogenic receiver with a new one. Each is dedicated to an important benefactor or contributor; these names, along with the

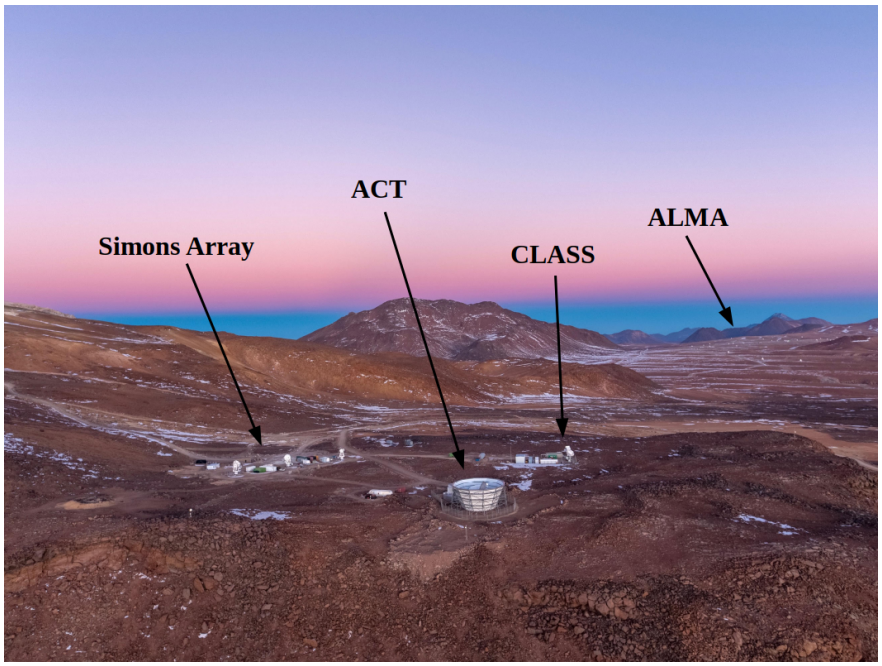

Figure 2.4: The Cerro Toco observing site as seen from the North, showing showing several of the adjacent microwave and sub-mm observatories. Photo by Debra Kellner.

respective positions and relationships to the cameras and observing frequencies, are given in Table 2.1.

	Position	**Telescope name**	**Band centers [GHz]**
POLARBEAR-2a	North	Nicholas Simons Telescope	95, 150
POLARBEAR-2b	South	Paul Simons Telescope	95, 150
POLARBEAR-2c	Central	Huan Tran Telescope	220, 280

Table 2.1: Nomenclature of the Simons Array telescopes and cameras

The anatomy of each telescope is described in Figure 2.5. Two angular motions are enabled via servo motors: in azimuthal angle, and in elevation angle. The telescope reflector, side baffling, and servo systems were built by General Dynamics SATCOM Technologies.[3] The baffling at the focus of the primary mirror, the cryogenic receiver and its enclosure, and the supporting electronics enclosures (called the *saddlebags*) were designed and built by the Simons Array collaboration. Notably, the secondary mirror is contained inside the receiver enclosure and is not visible in the images in Figure 2.5. The receiver and electronics enclosures are environmentally sealed and temperature controlled with ventilation and heating

[3] `https://www.gd.com/`

systems. Power lines, some electrical signal lines and helium lines for the refrigeration systems are routed through the telescope base and pass through special wraps which maintain constant routing length in both the azimuth and elevation motion directions.

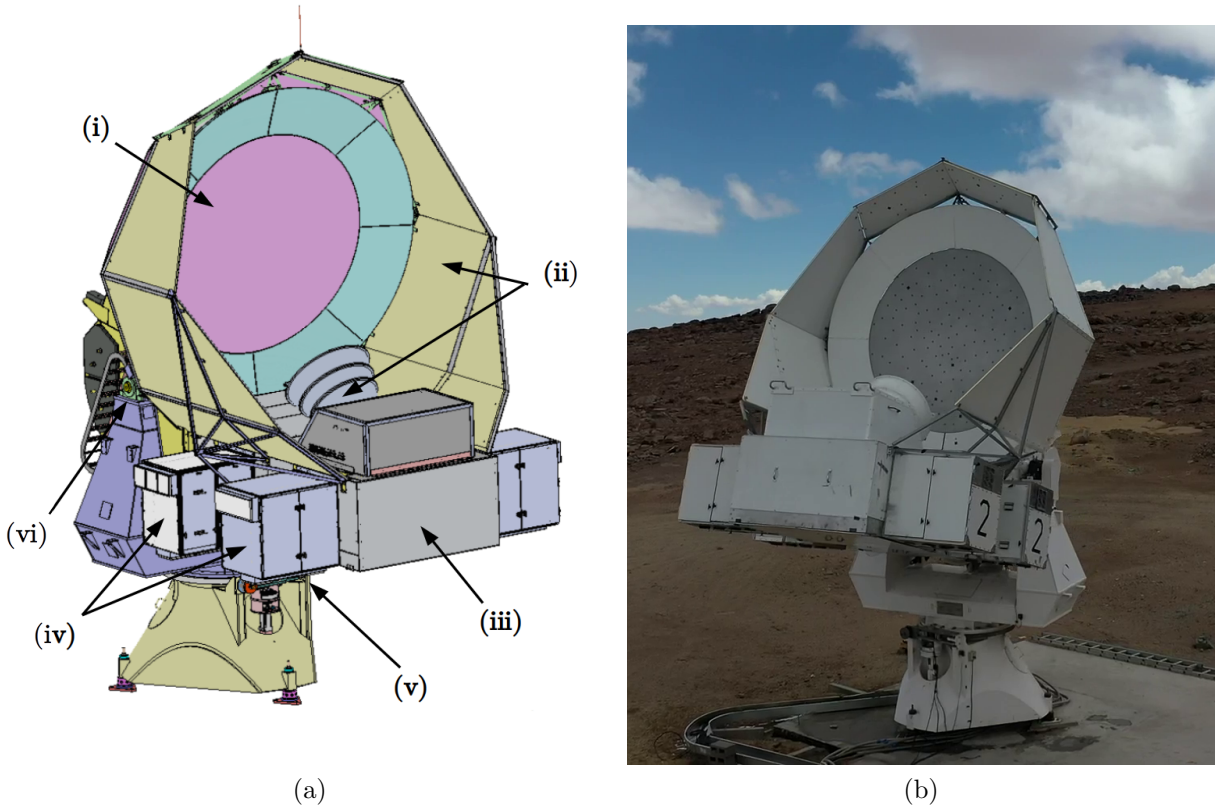

(a) (b)

Figure 2.5: The Simons Array telescope design. The CAD model in (a) shows (ii) the primary mirror, (ii) the co-moving baffling structure, (iii) the receiver enclosure which houses the secondary mirror, polarization modulator, and cryostat, (iv) the co-moving electronics enclosures, and the azimuth (v) and elevation (vi) bearings. The image in (b) shows the Nicholas Simons Telescope, the first in the Simons Array to be fitted with a cryogenic imaging receiver, with most but not all of its co-moving baffling installed. CAD image courtesy of Lindsay Lowry and photo courtesy of Nolberto Oyarce.

Telescope motions are controlled at a high level (i.e. which trajectory to follow on the sky) by custom software [41] and on a low level (i.e. motor control and feedback) with custom electronics provided by General Dynamics. The telescope can move as fast as $4^\circ/s$ in azimuth, but as will be discussed further in Chapter 5, the vibrations induced by such fast speeds may be undesirable for some purposes. Typical science observations of the CMB patch will involve motion with only the azimuth motor, but simultaneous motion in both

azimuth and elevation is possible and used for celestial source tracking during calibration observations.

2.2.2 Image-forming optics

The dual reflectors of an off-axis Gregorian configuration do not produce fully telecentric rays, and the focal surface is curved instead of planar. In order to couple to the microfabricated planar detector arrays that enable modern instrument sensitivities, then, a system of three reimaging lenses is used to create a planar optical focus with telecentric incoming rays from the sky, as indicated by the instrument cross-section with ray traces overlaid in Figure 2.6. These lenses provide an additional opportunity for a convenient baffle between the secondary mirror and the detector array, as will be discussed shortly. Additionally, a co-moving thermal calibration source is able to illuminate the focal plane via a small aperture in the secondary mirror. This thermal source may be turned on or off and modulated via a physical chopper blade, and is a necessary ingredient in the instrument calibration procedure.

The refractive reimaging lenses are constructed from high-purity amorphous alumina (Al_2O_3), which has good transmission and a high index of refraction at the CMB wavelengths ($n \approx 3.1$), and is available in the large 50 cm diameters desired for the Simons Array design. However, these lenses must be cooled for good transmission, and thus they are encased inside the cryostat with the detector array and thermalized to $T \approx 4$ K. A microwave-transparent vacuum window is then required between the lenses and secondary mirror; in POLARBEAR-2a and POLARBEAR-2b, at least, this window is constructed of a closed-cell cross-linked polyethylene block foam.[4]

An additional feature of the Simons Array optics design is that it includes multiple baffling points. Baffles prevent the intrusion of rays at large angles from entering the optical path, potentially introducing pickup of non-celestial polarization. In the time-reversed sense, they allow for truncation of the beam sidelobes as they evolve through the optical chain of the instrument. In both cases, the baffle is viewed as much easier to engineer to be stable. At the ambient temperature of the telescope, one baffle is installed surrounding the focus of the primary mirror, and is visible in Figure 2.6. This prime focus baffle also serves to enclose the receiver cabin, as it includes a microwave transparent window[5] to complete the environmental seal. Additionally, a cryogenic aperture stop is placed between the aperture and collimator lenses, cooled to $T \approx 4$ K. This latter baffle, also indicated in Figure 2.6, truncates the pixel beams formed by the lenslet-coupled planar antennas instrumenting the focal plane, controlling sidelobe pickup.

The high index of refraction of the alumina lenses necessitate anti-reflection (AR) coatings; otherwise, approximately 30% of the incoming radiation would be reflected away per alumina-vacuum interface. Furthermore, as each Simons Array camera simultaneously passes two observation bands, each with relatively large fractional bandwidth, a single-layer AR

[4]Plastazote HD30 by Zotefoams: `https://www.zotefoams.com/`

[5]Also constructed from Plastazote HD30, but a much thinner stack to maximize transmission and minimize emission and scattering. There is no requirement to sustain a pressure differential across this window

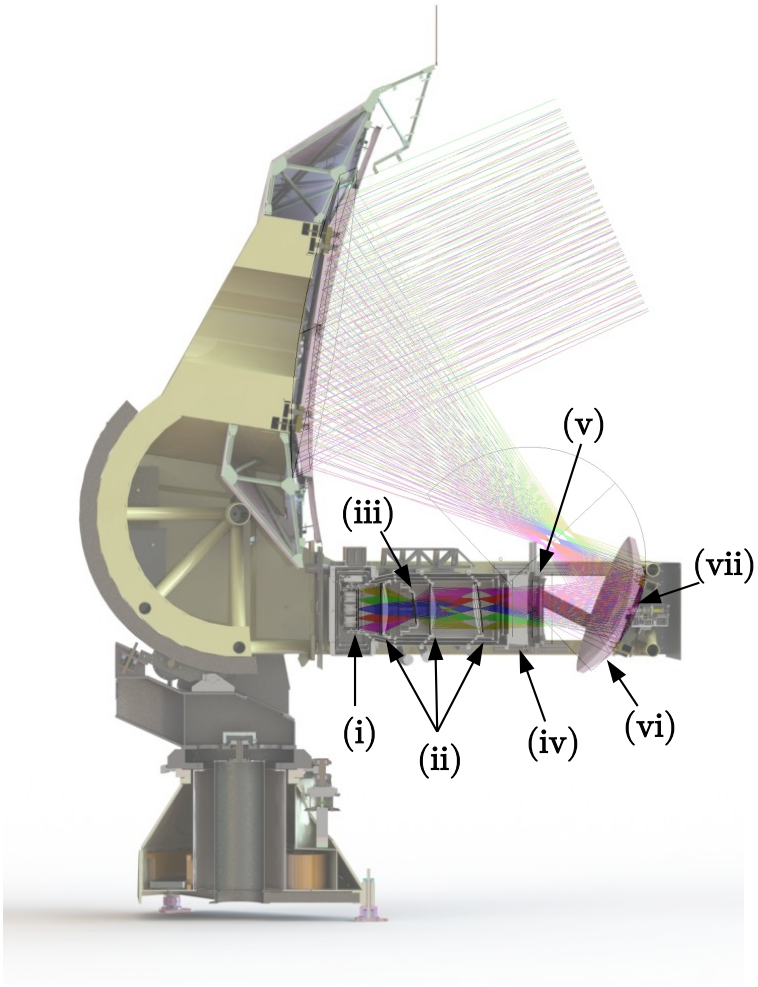

Figure 2.6: CAD cross-section of the POLARBEAR-2a instrument overlaid with ray traces from a geometric optics simulation. Visible in the cross-section are (i) the focal plane of the instrument where the detectors are placed, (ii) three reimaging lenses, (iii) a cryogenic aperture stop, (iv) the microwave-transparent vacuum window, (v) the ambient temperature continuously rotating half-wave plate, (vi) the secondary mirror, and (vii) the co-moving thermal calibrator. The POLARBEAR-2b and POLARBEAR-2c instruments are nearly identical, but each incorporate a slightly longer cryostat in which a cryogenic half-wave plate is placed.

coating is insufficient. Cryogenic AR coatings for large-diameter mm-wave optics are a major difficulty for modern CMB experiments, and a great amount of work has gone into the development of new coating technologies for the Simons Array. A particular challenge is that of reliable adhesion: the lenses must practically be fabricated at $T \sim 300$ K but operate at $T \sim 4$ K, causing differences in the coefficients of thermal contraction between the lens and AR coating materials to encourage delamination. For the Simons Array, a combination of thermally-sprayed ceramics, doped epoxies that act as their own adhesives, and separately adhered plastics have been developed to AR coat the various cryogenic optical elements. Several of these are pictured in Figure 2.7.

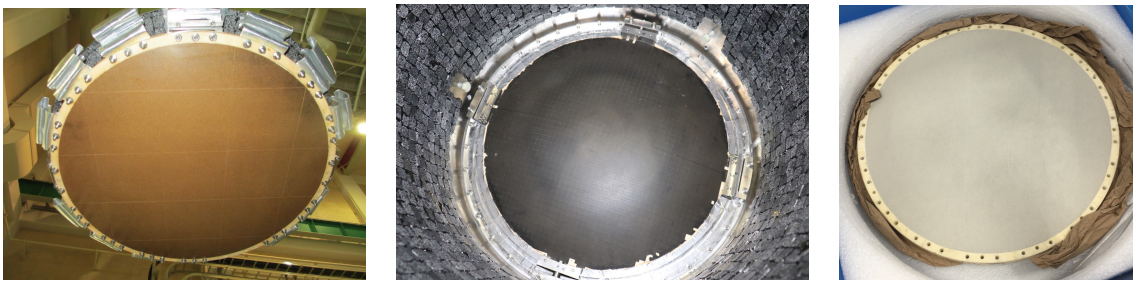

(a) (b) (c)

Figure 2.7: Photos of anti-reflection coating technologies developed for the Simons Array. (a) shows the Mullite-Skybond coating [42], deployed on the flat surfaces of the POLARBEAR-2a alumina optics, (b) shows the Stycast epoxy-based coating deployed on the curved surfaces of the POLARBEAR-2a alumina optics, and (c) shows the ceramic plasma spray coating [43], soon to be deployed in POLARBEAR-2b. Images (a) and (b) courtesy of Daiki Tanabe and image (c) courtesy of Lindsay Lowry.

2.2.3 Polarization modulators

A key aspect of the Simons Array observational strategy is the inclusion of active polarization modulation in the optical path. This modulation takes the form of a continuously rotating half-wave plate (HWP) placed approximately at the focus of the dual reflector system, as indicated in Figure 2.6. Continuously rotating HWPs utilize birefringent dielectric media to modulate the incoming celestial polarization while keeping the total intensity of the radiation unchanged. In POLARBEAR-2a, the HWP is placed outside the cryogenic receiver at ambient temperature. However, the presence of ambient temperature dielectric materials in the optical path requires a compromise in sensitivity (as both transmission through the waveplate is imperfect and the waveplate emits thermal radiation itself), so for POLARBEAR-2b and POLARBEAR-2c cryogenic HWP systems were developed. Both the warm and cold HWPs are placed in similar locations, with the cryostat length being extended to incorporate the extra optical element in the latter case.

The primary purpose of the HWPs in the Simons Array is to extend the accessible angular range of the instrument to larger scales. This is particularly important for inflationary science, where significant sensitivity can be gained if multiples near $\ell \sim 50$ or lower can be measured. Specifically, unpolarized thermal emission from the atmosphere, which fluctuates spatiotemporally with a red spectrum, can present a barrier to sensitivity at large angular scales. Modulation of the celestial polarization to a less-contaminated higher frequency for later demodulation presents a way around this barrier, and was demonstrated to good effect in the POLARBEAR experiment [44], [45]. Furthermore, HWP modulation stands to mitigate several systematic effects. In an experiment with no polarization modulation, the polarization state of radiation must be measured by differencing orthogonally polarized detectors within the same pixel. However, with a continuously rotating HWP, both polarization states are measured "simultaneously", mitigating systematics related to the differencing of detector pairs [44], [45].

For the Simons Array HWPs, monocrystalline sapphire was chosen as a birefringent material. Rather than a single sapphire plate, however, each HWP consists of a stack of three thinner plates in the Pancharatnam [46] configuration. This multi-plate configuration in which each plate is rotated relative to its neighbors was chosen because a single plate would be optimal for a single wavelength, but the Simons Array telescopes need to operate over a $\mathcal{O}(1)$ fractional bandwidth and minimizing the dependence of its optical properties on frequency is desirable. The POLARBEAR-2a HWP is mounted on a ball bearing rotation stage and driven via a belt coupled to a servo motor, pictured in Figure 2.8(a). To minimize thermal emission from adhesion layers, the plastic AR coating for the POLARBEAR-2a HWP is held on with a co-rotating vacuum system, the ballast for which may be seen surrounding the central plate. The vacuum is capable of holding for several weeks, and is re-evacuated during regular telescope maintenance. The POLARBEAR-2b and POLARBEAR-2c HWPs, being mounted inside the cryogenic receivers, are driven by a magnetically levitating superconducting bearing that dissipates very little thermal energy, also shown in Figure 2.8(b). To grip the HWP above the transition temperature of the superconducting bearing material, retractable gripper arms are incorporated into the cryostat design. The POLARBEAR-2a HWP is further described in [47], and the POLARBEAR-2b and POLARBEAR-2c HWPs are described in detail in [48].

2.2.4 Cryogenic design

The Simons Array design requires cryogenic cooling both of optical elements (lenses, filters, the aperture stop, and some baffling) and the detector arrays which sit at the instrument focal planes. Both of these purposes are achieved within a single cryostat per telescope, but conceptually each cryostat may be divided into a so-called *optics tube*, which houses the cryogenic optical elements, and *backend*, which contains the detector and readout components. Annotated cross-sections of the Simons Array cryostat designs, which differ slightly between POLARBEAR-2a, POLARBEAR-2b, and POLARBEAR-2c are shown in Figure 2.9. Each cryostat is cooled by two PT415 pulse-tube cryocoolers (PTCs) made by Cryomech

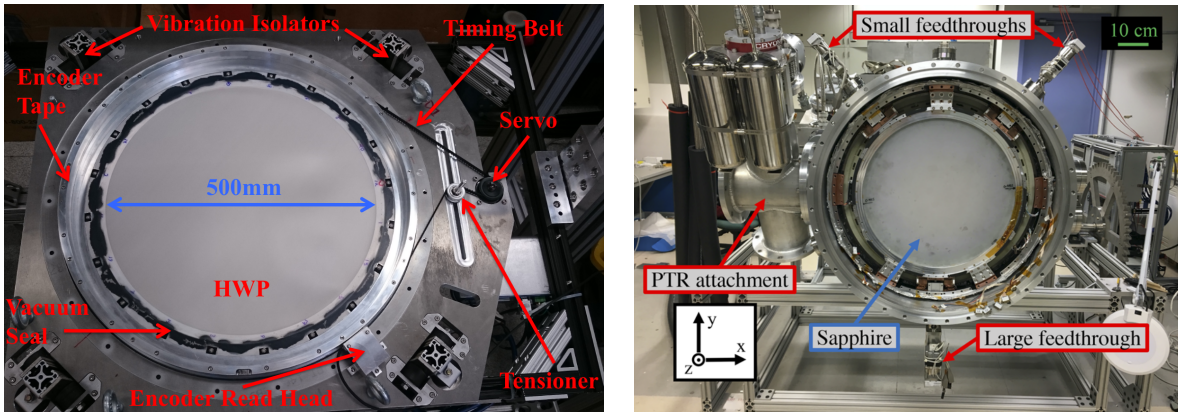

(a) (b)

Figure 2.8: Images of (a) the POLARBEAR-2a ambient-temperature half-wave plate and (b) the POLARBEAR-2b cryogenic half-wave plate, along with their mechanical assemblies. In the picture of the POLARBEAR-2b waveplate, the anti-reflection coating has not yet been applied. Images are courtesy of Charlie Hill and correspond to Figures 5 and 13 in [47] and [48], respectively.

Inc.[6], offering a heat sink at approximately 50 Kelvin with roughly 35 W of cooling power and another at approximately 4 Kelvin with roughly 1.5 W of cooling power. Conductive and radiative thermal loads on each heat sink are minimized via a design consisting of concentric aluminum shells mechanically supported by thermally insulating G10 rods and surrounded from radiative absorption by loose multi-layer aluminized mylar reflective blankets.

As each cryostat is open to incident radiation via a transparent window, multiple optical filters are incorporated throughout the system to minimize radiative absorption by the lenses and detectors. Immediately inside the vacuum window, a stack of radio transparent multi-layer insulation (RT-MLI) [49] immediately filters infrared power. A 2 mm thick flat plate of alumina additionally serves to absorb infrared radiation onto the 50 K heat sink of the optics tube PTC, protecting the lenses from the additional radiative power. As the lenses are made of alumina, they also serve to further filter out-of-band infrared power before it reaches the detectors. Finally, multiple low-pass metal-mesh filters (MMFs) constructed from alternating layers of polyethylene and metal mesh [50] are incorporated at both the cold aperture stop location ($T \approx 4$ K) and directly in front of the detector array ($T \approx 0.4$ K). In POLARBEAR-2a, the cutoff frequencies of the two filters placed at $T \approx 4$ K are 360 and 261 GHz; the cutoff frequency of the filter placed at $T \approx 0.4$ K is 171 GHz.

Additionally, each backend is surrounded by an approximate Faraday cage which serves to protect the SQUID array amplifiers (described in Section 2.2.5 and in more detail in Section 4.4) from electromagnetic interference (EMI). The isothermal portions of this cage

[6] https://www.cryomech.com/

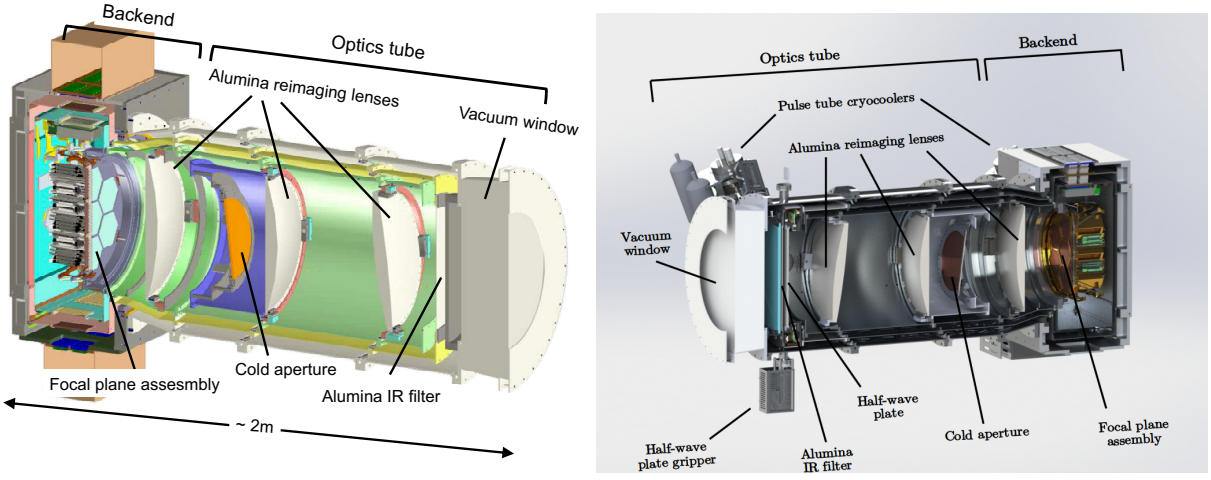

Figure 2.9: CAD cross-sections of the Simons Array cryogenic receivers. (a) shows the receiver design for POLARBEAR-2a and is courtesy of Masaya Hasegawa. (b) shows the receiver design for POLARBEAR-2b, which notably incorporates the waveplate inside the cryostat, and is courtesy of Lindsay Lowry.

are simply formed by tightly bolted metal joints, but the portions which span between heat sinks of the refrigeration system are constructed from thin aluminized mylar sheets. On the outside of the cryostat where continuous metal interfaces are not possible (such as at vacuum o-ring surfaces), specialty radio frequency (RF) gasketing is inserted to significantly damp transmission of potentially problematic radiation in the ∼MHz and ∼GHz ranges.

Using the $T \approx 4$ K heat sink of the backend PTC system, additional cooling for the detector array and the final MMF is provided by a multi-stage helium sorption refrigeration system provided primarily by Chase Cryogenics[7]. The details of this final refrigeration system differ somewhat between POLARBEAR-2a, POLARBEAR-2b, and POLARBEAR-2c, but in short it serves to cool the detectors to $T = 0.3$ K and simultaneously provides multiple intermediate heat sinks. These fridges operate by closed-cycle adsorption pumping on liquid He-4 and He-3, and require periodic recycling once per 1-3 days. The recycling procedure re-condenses liquid helium via controllable gas-gap heat switches and resistive heaters on the adsorption pumps, repeated in sequence for each of the several helium reservoirs chained in series within each fridge.

POLARBEAR-2a incorporates the "Berkeley He-10" design fridge from Chase Cryogenics. As the Simons Array design evolved, improved options became available. For POLARBEAR-2b, the newer "Gas-Lite 10" design was chosen, backed by a custom single-stage He-4 "booster" fridge. For POLARBEAR-2c, the need for a booster fridge was avoided by

[7] https://www.chasecryogenics.com/

additional helium charging of the Gas-Lite 10 design as available from Chase Cryogenics. Overall, however, the available cooling power is $\mathcal{O}(5)$ μW at 0.3 K, $\mathcal{O}(50)$ μW at 0.4 K, and $\mathcal{O}(200)$ μW at 1-2 K across all refrigeration implementations.

2.2.5 Detectors and readout

The reader is referred to Chapter 3 for a more detailed description of the Simons Array detectors and Chapter 4 for their accompanying readout electronics; merely a short overview is given here.

The sensitivity of modern CMB instruments is strongly driven by the number of detectors simultaneously observing the sky. In the Simons Array, a total of 5,670 pixels will simultaneously observe the sky; each pixel measures two linear polarizations in two colors, resulting in a total of 22,680 detectors. As demonstrated in Figure 2.6, the telescope optics serves to convert physical offsets on the focal plane to angular offsets on the sky. Collectively, the focal plane pixels observe non-overlapping regions of the sky across the telescope's 4.5° field of view. Through repeated telescope scans, disparate detectors will observe the same region of the sky, allowing for the co-addition of their maps and therefore a reduction in the overall noise.

The Simons Array pixels are evenly distributed across the focal planes of the three telescopes. One of these instrumented focal planes is pictured in Figure 2.10, showing that within each telescope the detectors are further evenly distributed within 7 hexagonal *modules*. This modularization not only assists in the high-throughput fabrication of detectors and their associated hardware, but is also required because the collecting area of the focal plane exceeds the maximum area of a silicon wafer that may be lithographically processed, as is required by the detector fabrication.[8]

Each focal plane array pixel focuses telecentric rays incident on the focal plane via hemispherical lenslets onto microlithographed planar antennas in a 1:1 ratio. The vacuum-lenslet transition involves a large change in dielectric constant, so the lenslets also must be AR coated; the black coloring visible in Figure 2.10 is characteristic of the epoxy-based coating employed, which is similar to the coating on several of the large-diameter optical elements. The antennas are broadband and polarization sensitive, and each polarization's feeds are split with on-wafer filters to transition-edge sensor (TES) bolometers, which are the detector elements transducing slow changes in $\mathcal{O}(100$ GHz) optical power to slow changes in electrical current. The antennas, filters, and TES bolometers are fabricated together in 6″ diameter silicon wafers with lithographic techniques, while the coupling lenslet arrays are hand-assembled from commercially available silicon hemispheres.

With such large detector counts, the wiring complexity, cost, and thermal load on the refrigeration system necessitate a multiplexed readout scheme to reduce the number of wires

[8] At least in typical academic nanofabrication facilities. Industrial production lines now are able to yield wafers with significantly larger diameters, but this technology has not yet reached the field of cosmology instrumentation.

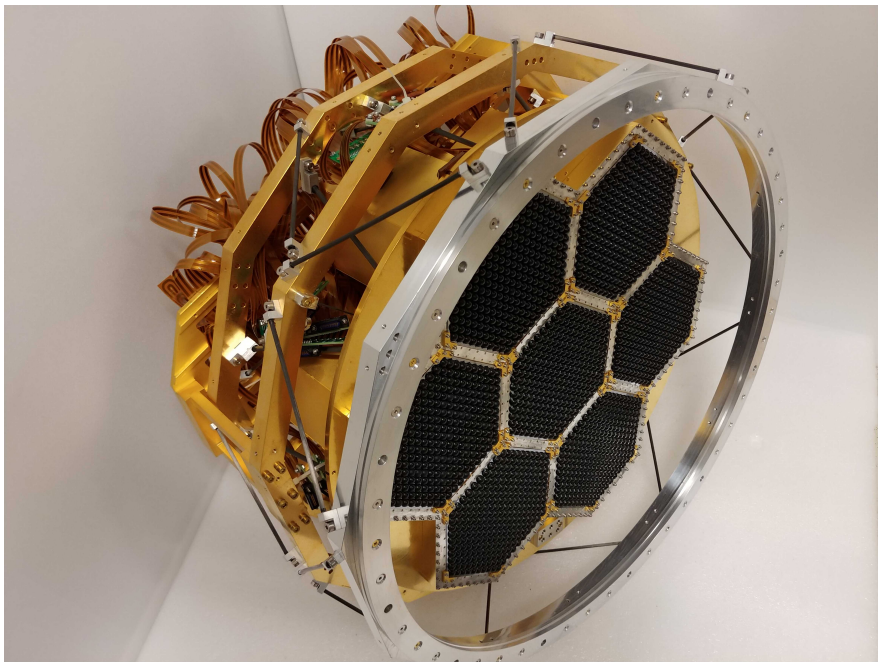

Figure 2.10: Picture of the POLARBEAR-2b focal plane array and its associated packaging hardware, excluding the aluminized mylar RF shield which spans between the $T \approx 0.3$ K detector array and the $T \approx 4$ K mount point, as well as the $T \approx 0.4$ K metal-mesh low-pass filters. Image courtesy of Jennifer Ito.

inside the cryostat. The Simons Array utilizes a newly developed digital frequency-division multiplexing (DfMux) technique, which combines the bias and readout of 40 channels over a single conductor pair. By amplitude-modulating sinusoidal carrier tones in the 1–5 MHz frequency range, signals are able to be combined in non-overlapping regions of frequency space and subsequently demodulated by ambient temperature digital electronics. To channelize the system, each detector in a multiplexer unit is wired in series with an LC resonator having a unique resonance frequency. Notably, the resonators are packaged behind the detector arrays as visible in Figure 2.10, enabling efficient use of the telescope focal plane area. The summed signals from each multiplexer are amplified once (at $T \approx 4$ K) inside the cryostat by a superconducting quantum interference device (SQUID) array before the final cable run to the first ambient temperature amplifier.

2.2.6 Data acquisition and management

Several categories of data are essential to gather and distribute in the Simons Array: data from the readout electronics measuring the responses of the TES bolometers, encoder position information from the telescopes themselves as they scan across the sky, encoder position information from the continuously rotating half-wave plate polarization modulators, and a

variety of auxiliary monitors for cryostat temperatures, weather conditions, helium pressures, etc. The data rate is dominated by the first source: each detector sample is 8 bytes, and with a sample rate of 152.59 Hz[9] the entire observatory will generate ∼60 MB/s. A detailed description of the data acquisition and transfer is given in [41]; what follows here is a brief overview.

Data collection from the readout electronics uses a slightly modified version of the `spt3g_software` package[10]. The readout boards stream detector samples over ethernet to the control computer operating in a container adjacent to the telescopes, where it is temporarily buffered on disk. Data from the continuously rotating half-wave plates is also collected using this same software process. Simultaneously but separately, the telescope control software (`GCP`, for Generic Control Program) which communicates with the azimuth and elevation servo motor systems runs its own collection process for the telescope encoder data and writes this information to disk. Finally, the acquisition of the remaining miscellaneous housekeeping data streams are gathered with a custom software package called `slowdaq`, which is easy to extend to semi-arbitrary data sources but not necessarily optimized for high-performance offline analysis.

In a semi-realtime process running on a separate machine, the buffered data from the detectors, HWP encoder, and telescope encoders is repackaged into an easily compressible format convenient for offline analysis. This compressed data, along with separately compressed `slowdaq` data files, are transferred to the nearest town of San Pedro de Atacama via a ∼MHz radio link. Once off the mountain, the data is distributed to computing storage sites across the globe at Simons Array collaborating institutions. The overall data collection and transfer process is depicted schematically in Figure 2.11.

2.3 Status

Construction of the Simons Array telescopes and cryogenic receivers has proceeded largely in parallel, with the installation and verification of all 3 telescopes completed in advance of their cameras. The integration and laboratory verification of the three cryogenic receivers has been split between the three leading project institutions: POLARBEAR-2a at KEK, POLARBEAR-2b at UC San Diego, and POLARBEAR-2c at UC Berkeley. A partially parallelized strategy was adopted for the construction of the cryogenic receivers, with a time-ordered focus on POLARBEAR-2a, followed by POLARBEAR-2b, followed again by POLARBEAR-2c.

Laboratory integration and testing of the camera for the first Simons Array instrument, POLARBEAR-2a, was completed in 2018. Upon installation on its mount in the North telescope, commissioning observations began at the very end of 2018. Throughout the 2019 calendar year and the beginning of 2020, the instrument underwent a variety of commissioning observations, calibrations, and repairs. After a shutdown of the observing site from the

[9]The sample rate is driven by the desire to resolve $\mathcal{O}(1)$ arcminute scales on the sky given a $\mathcal{O}(1)$ deg/s telescope scan speed, with some additional margin.

[10]`https://github.com/CMB-S4/spt3g_software`

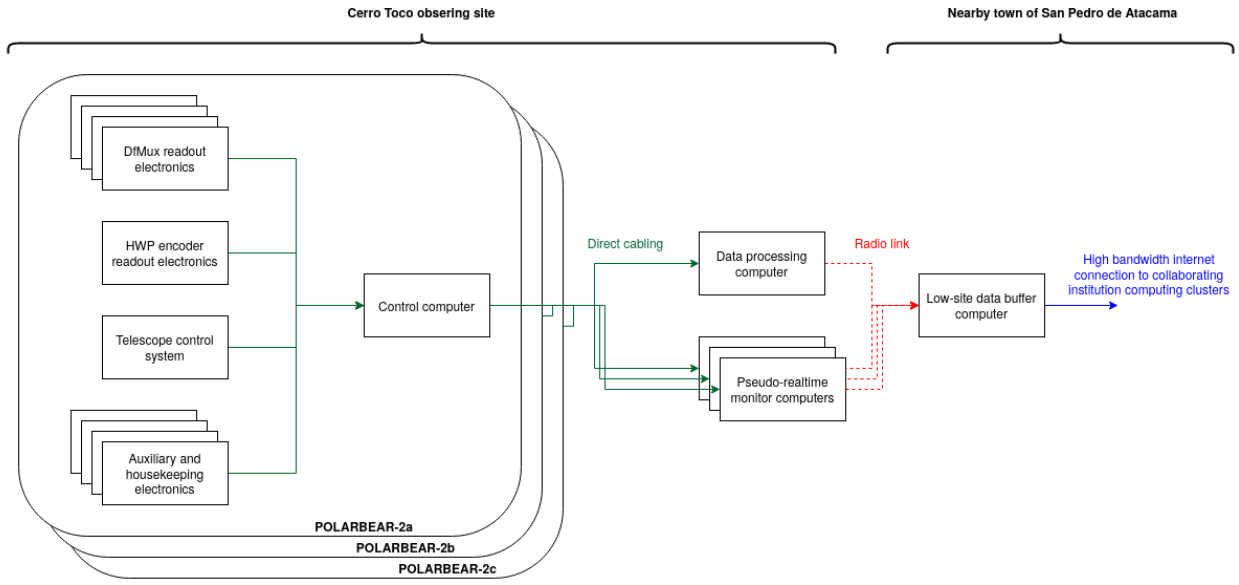

Figure 2.11: Simplified schematic of the Simons Array data flow.

COVID-19 pandemic, a major cryogenic refurbishment was performed on-site, with observations restarting in early 2021. At the time of this writing, the instrument is currently being characterized with its new cryogenic hardware, and plans for regular scientific observations are being finalized. Chapter 5 of this thesis presents in greater detail the deployment and commissioning of POLARBEAR-2a.

The POLARBEAR-2b receiver was determined ready for shipping in late 2019, and installation on-site began in early 2020, though was also paused through the calendar year due to the COVID-19 pandemic. At the time of this writing, on-site integration of the POLARBEAR-2b camera with its telescope is underway.

Construction of the POLARBEAR-2c receiver remains in progress, with multiple successful thermal cycles incorporating a partial set of components thus far. Furthermore, many detector and readout elements are at advanced stages of fabrication and procurement. However, further development is needed to finalize the optical elements, as the higher 220 GHz and 280 GHz bands require changes relative to technologies already verified in POLARBEAR-2a and POLARBEAR-2b.

Chapter 3

Cryogenic Detector Arrays

One of the driving technology directions for cosmic microwave background imaging measurements is the scaling up of detector counts to improve sensitivity. The Simons Array takes a particularly ambitious step in this aspect with more than an order of magnitude increase over its predecessor experiment, POLARBEAR. While modern photolithography techniques have played a central role in this effort, the packaging together of all the detector elements also presents a notable challenge. In this chapter, the detector arrays developed for the Simons Array are described, with particular focus on the cryomechanical embedding of the detectors in their cameras.

3.1 Antenna and sensor technology

The Simons Array focal planes are instrumented with lenslet-coupled, multi-chroic, and polarization-sensitive planar antennas whose excitations are detected by transition-edge sensor (TES) bolometers operating at a fraction of a Kelvin. As discussed herein, detector count is an important sensitivity driver; scalability thus is a central theme in these technologies. Here follows an overview of the principles of operation for these antennas and detectors.

3.1.1 Optical coupling

For simultaneous observations of the CMB with multiple pixels, planar antennas are an attractive design choice; they may be reliably fabricated in mass on flat silicon wafers and offer broader bandwidth than the common alternative of horn-based radiation collection. However, short of deliberate beam-forming with antenna phasing techniques (e.g. as in [51]), one typically needs additional coupling optics to create a desirable radiation pattern from a planar antenna. For multi-chroic polarization-sensitive CMB observations, a particularly powerful combination identified and developed in [52] and [53] is that of a sinuous antenna behind a hemispherical silicon lenslet. Together with the silicon wafers on which the antennas

and lenslets are housed, the lenslet hemisphere approximates an ellipsoidal lens with the antenna at one of the foci. This arrangement is depicted schematically in Figure 3.1(a).

Coupled in this manner, the sinuous antenna/lenslet combination forms a radiation pattern with a nearly Gaussian main lobe whose width may be tuned to the telescope optics. The FWHM of the main lobes in POLARBEAR-2a and POLARBEAR-2b, for example, are approximately 30° and 18° for the 95 GHz and 150 GHz bands [54]. The antenna also has a small backlobe response, but in the Simons Array this is controlled by illuminating the back of the antenna with 0.3 Kelvin blackbody radiation from the antenna wafer packaging (discussed further in 3.2); as a result, only the time-varying main lobe response contributes to the signals detected by the TES bolometers. As the lenslets and planar fabrication wafers are constructed from silicon, a high dielectric material with $n = 3.1$, an anti-reflection (AR) coating is required. An epoxy-based multi-layer coating similar to the large diameter reimaging lens coatings is used in the Simons Array [54].

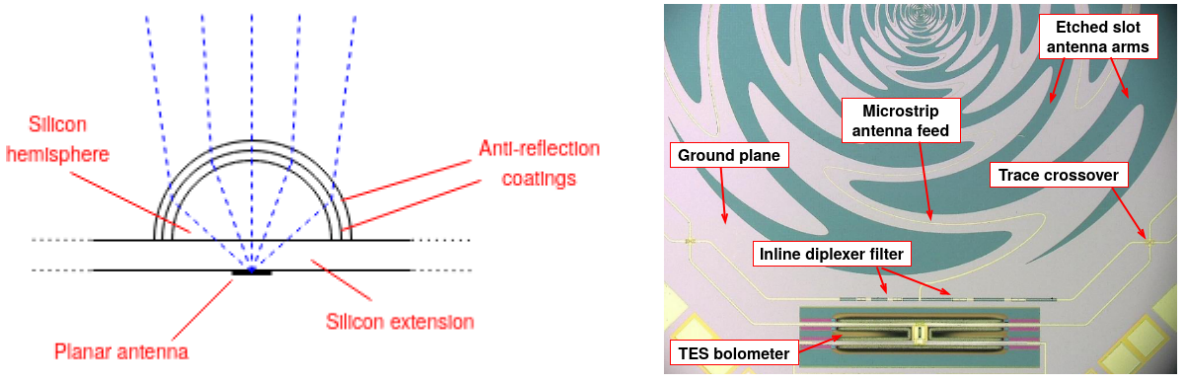

(a) (b)

Figure 3.1: Design of the Simons Array detector pixels. Telecentric rays from the telescope imaging system are focused onto a planar antenna via individual offset hemisphere lenslets which each approximate an elliptical lens, shown diagrammatically in (a). Electrical excitations in the planar antenna arms are transmitted to TES bolometer detectors via microstrip feedlines, as indicated in the micrograph of a detector pixel in (b). Inline bandpass filters and microstrip crossovers route two colors from each antenna polarization to a unique detector for a total of 4 optical detectors per pixel.

The 4-arm sinuous antenna is self-complementary[1] - allowing it to be fabricated by etching its arms out of an otherwise continuous ground plane - and self-similar[2] - enabling nearly abribtrary bandwidth. The slot construction of the antenna enables each of its two polarizations to be fed differentially with microstripline feeds. The broadband nature of the

[1]meaning it is identical to its negative - if all free space and conducting materials were swapped, it would be identical

[2]meaning that it appears identical when viewed on different length scales

sinuous antenna enables simultaneous observation of multiple frequency bands, desirable for spectral-based separation of astrophysical foregrounds from the CMB. The Simons Array observes only 2 colors per antenna, though more are possible (e.g. as implemented in [21]). Each color is split by on-chip bandpass filters to be directed to individual detectors. A total 2 colors $\times$ 2 polarizations = 4 optical detectors per antenna are included in each pixel. For calibration purposes, 2 additional "dark" detectors are fabricated in each pixel, though only a small fraction of these are electrically connected and read out. A partial micrograph of a Simons Array sinuous pixel is shown in Figure 3.1(b), demonstrating many of the design and construction details.

3.1.2 TES bolometer detectors

The electrical excitations of the antenna feeds are deposited via Joule heating as thermal power and detected by TES bolometers. A bolometer is a thermal detector consisting of an isolated thermal mass (often called the "island") whose temperature is modulated by the optical signal of interest and whose temperature fluctuations are sensed by a thermistor. In the case of a TES bolometer, the thermistor is a thin-film superconductor operating in the middle of its superconducting transition where the resistance-temperature relationship is extremely steep. The bolometer island is weakly coupled to a thermal bath, so that incoming optical power and electrical power may be balanced so as to hold the island temperature at the critical temperature of the TES. This arrangement is depicted schematically in Figure 3.2(a), and an actual fabricated device is also visible in Figure 3.1(b).

A principal reason for the ubiquitousness of TES bolometers in the field of CMB observations is their ability to be mass produced with modern silicon-based lithography techniques. In the Simons Array, the bolometers are constructed from trench etched low-stress silicon nitride; the thin silicon nitride "legs" form the weak thermal link to the thermal bath. The thermal mass of the bolometer island is tuned by careful deposition of a high heat capacity metal, palladium. The TES material is constructed from aluminum doped with $\sim$4000 ppm manganese, which reduces the critical temperature relative to un-doped aluminum (1.2 K) to about 440 mK. A simple thin film of titanium forms the antenna load resistor, and superconducting niobium microstrip leads route signals to and from the bolometer. Further details on the antenna and detector fabrication can be found in [55].

Several properties of TES bolometers are relevant for their use in large detector arrays, as in the Simons Array cryostats. Here follows a brief review of the relevant detector theory; the interested reader is directed to [56] and [57] for more thorough treatments.

For small signals, the electro-thermal system of a TES bolometer is linear and we may use single Fourier components for simplicity. If one considers an optical power comprising of a steady-state component and a small time-variable Fourier component - and likewise for the island temperature and resulting electrical power - for a DC voltage biased TES bolometer

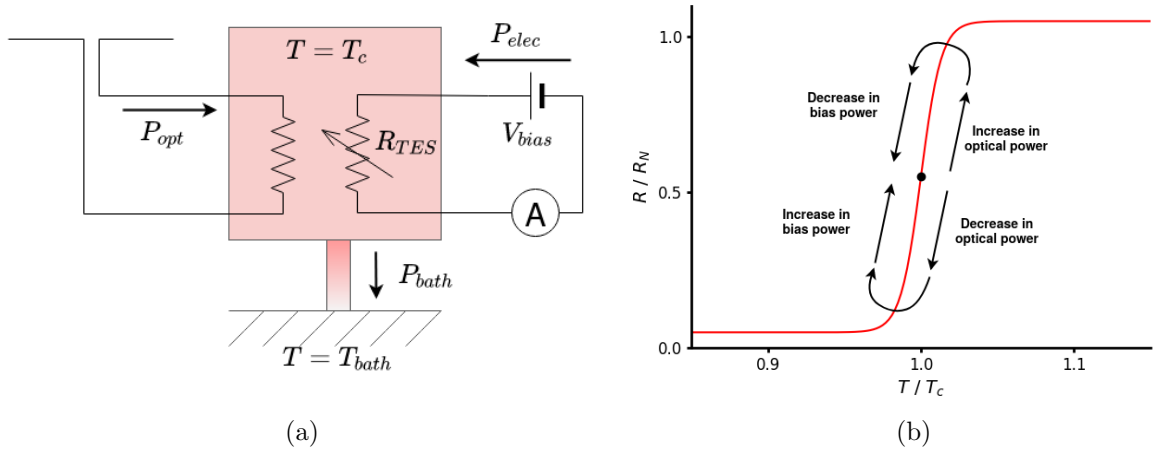

(a) (b)

Figure 3.2: Schematic description of a voltage-biased antenna-coupled TES bolometer. The electro-thermal circuit is depicted in (a); the bolometer consists of an isolated mass connected weakly to a thermal bath at $T = T_{bath}$ and a transition-edge sensor (TES) thermistor. Optical power P_{opt} from the antenna and electrical power P_{elec} together heat the bolometer "island" to the thermistor's transition temperature T_c and balance the thermal power P_{bath} lost to the bath via the weak thermal link. The cartoon in (b) depicts how, when voltage biased, the resulting change in P_{elec} acts to oppose any change in P_{opt}, giving rise to negative feedback. This electro-thermal feedback (ETF) removes the need for feedback to keep the detector biased in the middle of the TES transition.

biased in the middle of its superconducting transition

$$P_{opt}(t) = P_{opt,0} + \delta P_{opt} e^{i\omega t} \tag{3.1}$$
$$T(t) = T_c + \delta T e^{i\omega t} \tag{3.2}$$
$$P_{elec}(t) = P_{elec} + \delta P_{elec} e^{i\omega t} \tag{3.3}$$

then conservation of energy for the system may be written as

$$P_{opt,0} + \delta P_{opt} e^{i\omega t} + P_{elec} + \frac{dP_{elec}}{dT} \delta T e^{i\omega t} = \frac{NA}{L} \int_{T_{bath}}^{T_c} k(T') dT' + (g + i\omega C) e^{i\omega t} \tag{3.4}$$

where C is the island heat capacity and g is the dynamic thermal conductance $\frac{dP}{dT}$ of the N bolometer legs of cross-sectional area A, length L, and thermal conductivity k. The left-hand side of (3.4) represents the energy flow of the optical and electrical inputs, while the right hand side represents the energy flow to the thermal bath and the variation in the energy stored in the island thermal mass. Collecting time-varying terms and noting that

$$\frac{dP_{elec}}{dT} = \frac{d(V^2/R)}{dT} = -\frac{V^2}{R^2} \frac{dR}{dT} = -\frac{\alpha P_{elec}}{T_c} \tag{3.5}$$

where $\alpha \equiv \frac{d\ln R}{d\ln T}$ is a common parameterization of the TES transition shape, one finds

$$\delta P_{opt} = \left(\frac{\alpha P_{elec}}{T_c} + g + i\omega C \right) \delta T \tag{3.6}$$

It is worth noting here the phenomenon of electro-thermal feedback: the derivative in (3.5) is negative, implying that TES bolometers (for which $\alpha > 0$) self-stabilize when voltage biased. This is illustrated further in Figure 3.2(b). In the current-biased case, TES bolometers are unstable. As will be discussed in Section 4.6, parasitic impedances Z_{par} in series with the TES thermistor due to cabling in the readout circuit may partially spoil the voltage bias. In general, one desires $|Z_{par}| \ll R_{TES}$ for stable operation.

Under a DC[3] voltage bias, each TES bolometer acts to convert optical power changes δP_{opt} into changes in electrical current δI_{elec} via the *power-to-current responsivity*

$$S_I \equiv \frac{dI_{elec}}{dP_{opt}} = \frac{1}{V_{elec}} \frac{dP_{elec}}{dP_{opt}} \tag{3.7}$$

$$= \frac{1}{V_{elec}} \frac{-\left(\frac{\alpha P_{elec}}{T_c}\right)\delta T}{\left(\frac{\alpha P_{elec}}{T_c} + g + i\omega C\right)\delta T} \tag{3.8}$$

$$= -\frac{1}{V_{elec}} \frac{\mathscr{L}}{\mathscr{L}+1} \frac{1}{1+i\omega\tau} \tag{3.9}$$

where $\mathscr{L} = \alpha P_{elec}(gT_c)^{-1}$ is the DC loop gain and $\tau = C(g(\mathscr{L}+1))^{-1}$ is the effective time constant of the detector. The result in (3.9) has important consequences for large arrays of TES bolometers: for detectors in the high loop gain limit ($\mathscr{L} \gg 1$), their low-frequency responsivities are dependent only on the electrical bias parameters. This helps ensure uniformity across large quantities of detectors whose realized properties might otherwise have large variations across the array.[4]

For the aluminum manganese TESs fabricated for the Simons Array, the logarithmic transition steepness α increases as the TES is cooled its normal state into the middle of the transition. As a result, the loop gain $\mathscr{L}$ increases and the effective time constant τ decreases as the detector is biased deeper and deeper. Meanwhile, the power-to-current responsivity S_I increases simply because lowering the voltage bias is being lowered. These practical effects are simultaneously demonstrated in Figure 3.3, demonstrating that the detectors increase their effective DC gain and respond to faster optical signals as they are biased deeper in their transitions. In practice, one typically strives to bias detectors as deep as is possible without running into stability concerns from series impedances. See Section 4.6 for further details.

[3]In the AC voltage biased case, as is actually relevant for the Simons Array, the responsivity requires a slight modification to $S_I = -\frac{\sqrt{2}}{V_{bias,\,RMS}} \frac{\mathscr{L}}{\mathscr{L}+1} \frac{1}{1+i\omega\tau}$.

[4]It should be noted that the presence of an impedance in series with the TES, in addition to affecting the electro-thermal feedback stability, results in a small boost in responsivity. This result is derived in [58].

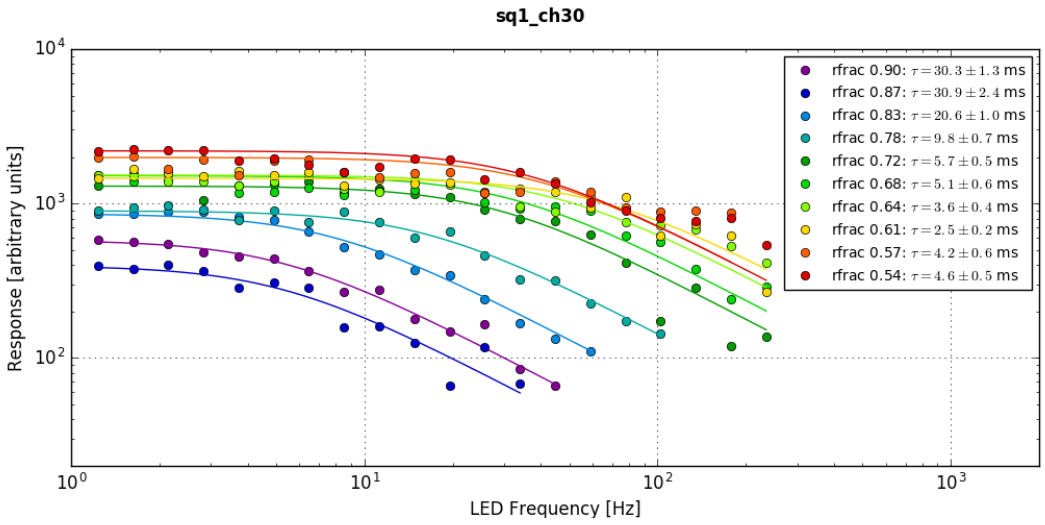

Figure 3.3: Example optical measurements for an example detector which demonstrate both the power-to-current responsivity and detector bandwidth increasing as it is progressively biased deeper into the TES superconducting transition.

Another feature of TES bolometers relevant for massive modern arrays - in which microphonic heating of T_{bath} is conceivable as a result of the finite mechanical stiffness of its mounting hardware - is that with a fixed voltage bias, fluctuations in the T_{bath} can modulate the detector properties at a small level. Conceptually, it is the first term on the right hand side of (3.4) in which this effect enters; the resulting fractional change in the DC responsivity may be approximated as

$$\frac{dS_I/dT_{bath}}{S_I} = \frac{-\alpha N A k(T_{bath})}{\mathscr{L}(\mathscr{L}+1)gT_cL} \tag{3.10}$$

via the implicit T_{bath} dependence of $\mathscr{L}$. Efforts to minimize this effect in the Simons Array will be detailed further in Section 3.2 and Section 5.3.

Finally, a brief discussion of noise is essential for understanding the use of TES bolometers in large arrays to observe the CMB. In general, several sources contribute to noise[5] in an optically-coupled voltage-biased TES bolometer:

1. Johnson noise from the finite resistance of the TES
2. Fluctuations in the thermal carriers transferring thermal power from the bolometer island to the thermal bath

[5]Specifically, white noise - this picture breaks down when considering extremely slow (i.e. 1/f fluctuations) or very fast (i.e. environmental RF pickup) contributions. The latter contributions are typically engineered away or transient and flagged for removal in offline analysis. The former contributions are of great importance for low-ℓ science, and are the reason for the extensive engineering that goes into instrumental stability and mitigation of atmospheric 1/f fluctuations.

3. Fluctuations in the occupation number of the incoming optical radiation
4. Electrical noise resulting from the bias and readout circuitry

Noise in a detector may be quantified by the *noise-equivalent power* (NEP), the equivalent optical power of a noise source in consideration contributes per Hz of bandwidth. The above noise sources are typically Gaussian and uncorrelated, so their amplitudes add in quadrature. Moreover, if multiple detectors are used simultaneously, the independent observations they contribute further add in quadrature.[6] Thus,

$$NEP_{total} = \sqrt{\frac{NEP^2_{Johnson} + NEP^2_{thermal} + NEP^2_{photon} + NEP^2_{readout}}{N_{det}}} \tag{3.11}$$

The first and last noise sources, however, are fundamentally current noise sources while the remainder are fundamentally power noise sources. A more convenient representation is sometimes the *noise-equivalent current* (NEI), for which the detector responsivity is needed to convert to a NEP:

$$NEP_{total} = \sqrt{\frac{\left(\frac{1}{S_I} NEI_{Johnson}\right)^2 + NEP^2_{thermal} + NEP^2_{photon} + \left(\frac{1}{S_I} NEI_{readout}\right)^2}{N_{det}}} \tag{3.12}$$

The low-frequency NEP for a high-loop gain Johnson noise for an AC voltage biased TES bolometer biased to a resistance R_{TES} at its transition temperature T_c and with negligible parasitic series impedance is simply

$$NEP_{Johnson} = \left|\frac{1}{S_I}\right| \frac{\sqrt{4k_B T_c R_{TES}}}{R_{TES}} = V_{bias,\,RMS} \sqrt{\frac{2k_b T_c}{R_{TES}}} \tag{3.13}$$

For example Simons Array parameters $R_{TES} = 1\ \Omega$, $T_c = 440$ mK, and $V_{bias,\,RMS} = 2\ \mu$W, one finds $NEP_{Johnson} \approx 7$ aW/$\sqrt{\text{Hz}}$.

For a bolometer with primarily insulating legs such that the dominant thermal carriers are phonons, the thermal carrier fluctuation noise-equivalent power is [53]

$$NEP_{thermal} = \frac{8\sqrt{k_B P_{bath} T_{bath}}}{3} \sqrt{\frac{(T_c/T_{bath})^9 - 1}{[(T_c/T_{bath})^4 - 1]^2}} \tag{3.14}$$

For example Simons Array parameters $P_{bath} = 10$ pW, $T_{bath} = 0.25$ K, $T_c = 0.44$ K, one finds $NEP_{thermal} \approx 23$ aW/$\sqrt{\text{Hz}}$.

The photon noise NEP_{photon} is more complicated to compute, as it depends on the integrated spectra of all radiation sources in the optical path - including both the atmosphere and every refractive optical element in the experiment. A full model of the experiment

[6] Assuming each detector is observing an uncorrelated patch of the sky. If the detector beams overlap, then a more complicated treatment is required. No appreciable overlap occurs in the Simons Array design.

is required an the calculation is typically done numerically (see [53], [59] for examples). However, values for detectors across observation bands and cryostat configurations in the Simons Array typically lie in the 25–50 aW/$\sqrt{\text{Hz}}$ range.

The sources contributing to readout noise are described in detail in Section 4.8. For context, however, a typical achieved readout noise is $NEI_{readout} \approx$15 pA/$\sqrt{\text{Hz}}$, corresponding to $NEP_{readout} \approx 21$ aW/$\sqrt{Hz}$ for a high loop gain detector with $V_{bias,\,RMS} = 2\ \mu$V.

It should be noted that of all the aforementioned noise sources, the photon noise presents the most fundamental noise floor. Some engineerability exists due to its dependence on the instrument refractive optics, but the sky emission is unchangeable.[7] Modest improvements in overall sensitivity may come from reductions in the quadrature contributions of $NEP_{thermal}$ and $NEP_{readout}$, but it is clear from (3.12) that substantial improvements in raw sensitivity must come through increases in detector count. This, ultimately, is the reason that modern CMB experiments incorporate thousands of detectors, build optics systems with large collecting areas, require highly multiplexed readout electronics, and utilize high performance parallel computing techniques for offline data analysis.

3.2 Modularization and packaging

The scaling up of detector count in the Simons Array relative to POLARBEAR has been significantly enabled by advances in the lithographed fabrication of TES bolometers and their antennas. In particular, the Simons Array devices are fabricated on 6" diameter silicon wafers (POLARBEAR fielded 4" wafers), which are harder to yield from a nanofabrication perspective but enable more efficient use of the valuable focal plane area. As the area-to-perimeter ratio A/P of a hexagon of diameter D scales as $A/P = D\sqrt{3}/8$, less dead space is required for mounting hardware at the periphery of each wafer. This does, however, place additional difficulties on the mechanical mounting, thermalization, and connectorization of the wafers.

The lenslets which focus the telescope's telecentric rays onto each sinuous antenna are arrayed into position via a silicon wafer with identical footprint to the detector wafer. Deep reactive ion etched pockets enforce accurate positioning of the lenslets with respect to this wafer, which is later aligned as a whole to the antenna wafer. Individual lenslets are first anti-reflection coated and then subsequently epoxied into their pockets. One such populated lenslet wafer is shown in Figure 3.4(a), and further details can be found in [54] and [60].

The pixels housing the planar antennas and their associated TES bolometer detectors are as described in Section 3.1.2. A total of 271 pixels are included in each wafer, pictured in Figure 3.4(b). When arraying many pixels together, the two polarization orientations of pixels - Stokes Q and Stokes U - must be distributed in approximately equal quantities across the wafer. Additionally, the sinuous antenna has a handedness, so to mitigate potential

[7] Of course, one can choose an observing site with minimal atmospheric thermal emission or launch a CMB instrument on a satellite. The Simons Array already operates at one of the best ground-based sites in the world, however.

systematics arising from this handedness, mirror copies of the "A" handedness are included in equal quantities as a "B" type. The wafers are oriented such that during constant elevation scans of the sky, the four pixel types - QA, QB, UA, and UB - cross over the same sky area in rapid succession. Wiring for the TES bias and readout leads is routed to bonding pads on the perimeter of the wafer. Further details about the design and fabrication of the detector wafers may be found in [53], [61], and [55].

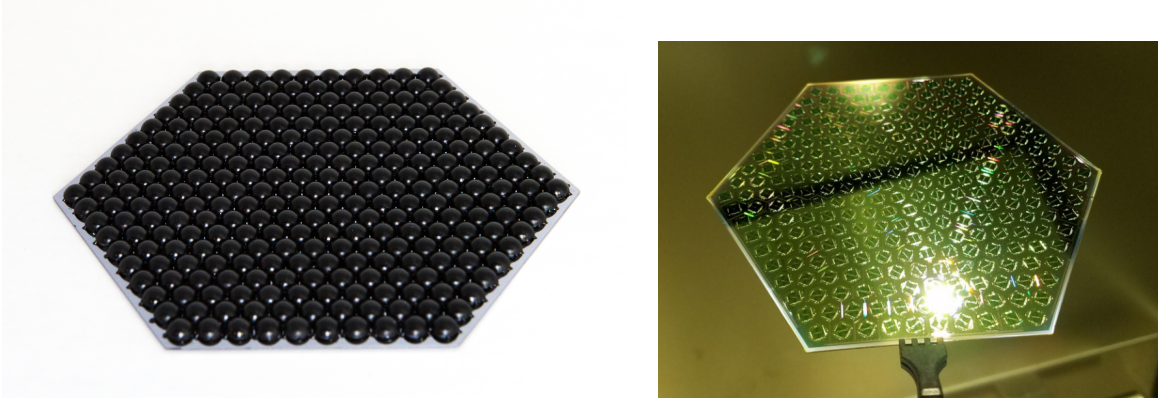

(a) (b)

Figure 3.4: Pictures of the (a) lenslet wafers and (b) detector wafers that mate together in each detector module. Images courtesy of (a) Praween Siritanasak and (b) Christopher Raum.

The embedding of these lenslet and detector wafers in the larger cryogenic system must satisfy several important requirements. Namely:

1. The wafers must be reliably mechanically constrained, satisfying a relative alignment tolerance of 25 μm between the lenslet and detector wafers.
2. A solution for controlling the response of the antenna backlobes must be included.
3. The detector wafer must thermalize stably at the desired bath temperature T_{bath} for detector operation.
4. The TES bias and readout lines must be routed off-wafer with high yield and low parasitic impedance.
5. The packaging must include the channelizing resonators required by the multiplexed readout.
6. The embedding must be compatible with the Faraday cage surrounding the SQUID array amplifiers.

The solution to these constraints in the Simons Array is pictured in Figure 2.10. The individual lenslet/detector wafer pairs are packaged into interchangeable *detector modules*,

7 of which instrument each telescope's focal plane. The 7 modules are mounted together in a single thermomechanical structure which acts as a mechanical buffer between the sorption refrigerator and the detector module hardware and also incorporates mounts for heat sinking of the readout cables and Faraday cage material.

The design of each individual detector module is shown in Figure 3.5. The unpatterned sides of the lenslet and detector wafers mount together, clamped via screws between two pieces of an iron-nickel alloy whose thermal contraction is nearly matched to that of silicon.[8] Aluminum wire bonds route signals off-wafer to isothermal flexible tinned copper flexible cables, which in turn terminate in a standardized flexible printed circuit (FPC) connector. This connector mates the detectors with the multiplexed readout channelizing resonators, described in detail in Section 4.3. A back plate behind the planar antennas hosts a $T \approx 0.3$ K blackbody to uniformly illuminate the antenna backlobes and also serves as a mount point for the readout resonator mounting boards. The resonator boards are further surrounded by a gold plated copper can, which provides an additional cooling path and further serves as a radiation shield for the printed circuit board (PCB) components of the module which have fairly high emissivity.

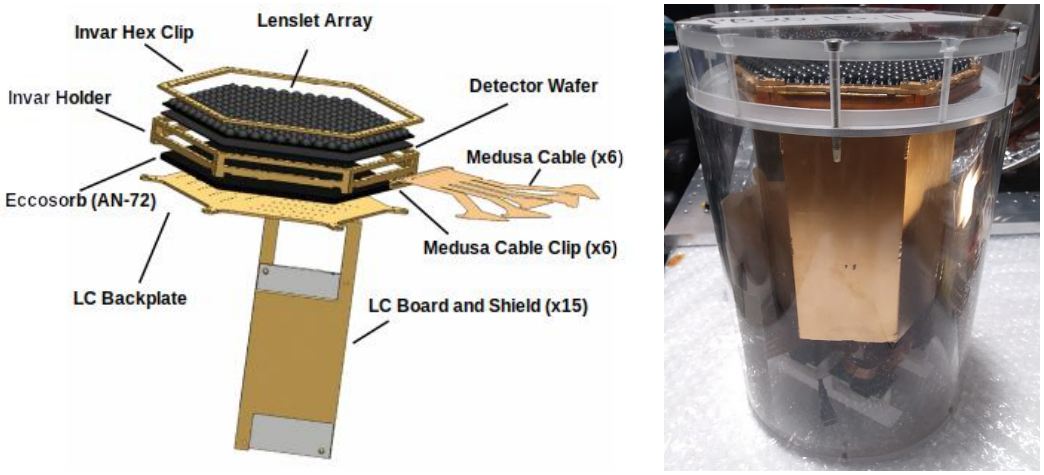

(a) (b)

Figure 3.5: Exploded CAD model (a) and image (b) of a Simons Array detector module inside a plastic container commonly used for shipping and handling. The CAD model does not include the radiation shield around the LC boards, which is the gold-plated hexagonal can in the picture.

As the Simons Array in its full configuration requires 21 fielded detector modules,[9] a robust and high-throughput assembly process is needed. The procedure developed for as-

[8] A more conventional metal mount - copper, for example - would thermally contract upon cooling enough to shatter the brittle silicon wafers. The alloy in use is 64FeNi, known commonly as *invar*.

[9] In practice, R&D modules and field spares increase this number significantly

sembling the detector modules is illustrated in Figure 3.6. Critically, the alignment and handling of the brittle bare silicon wafers is handled by fabrication engineers before the wafer leaves the clean room, aiding in the robustness of the procedure. The attachment, bonding, electrical inspection, and routing of the off-wafer flexible cables are crucially able to be performed by a technician operating a robotic wirebonder, increasing the reliability and speed of the process. Thus far, graduate students and postdocs have assembled the readout hardware onto the bonded wafers, but there is no reason this final assembly process couldn't be technician-based if needed as well.

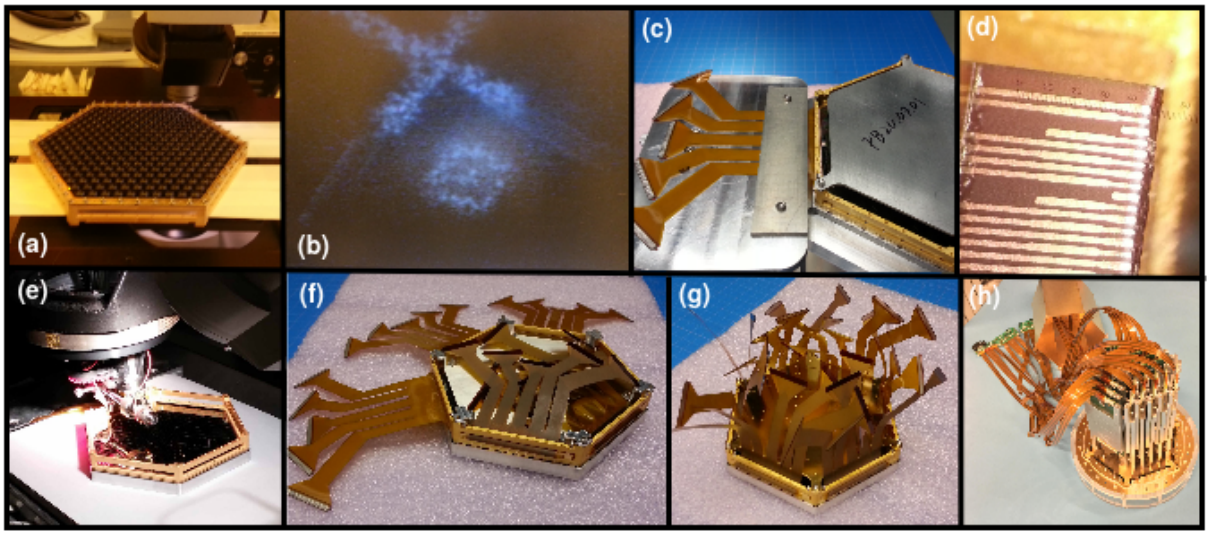

Figure 3.6: Assembly procedure for the Simons Array detector modules. First, the lenslet wafer and detector wafer are (a) aligned with an infrared microscope, utilizing pre-etched features in both wafers. A typical microscope image showing the alignment of features is shown in (b). The flex cables are then mounted (c) with the aid of an optical microscope, taking care to align the wirebond pads of the cable (d) to those on the detector wafer. The flex cable and detector wafer are robotically wirebonded (e), and electrically tested. Wirebonds on channels with shorts are removed by hand. After bonding, the flex cables are woven through the invar detector holder (f) so as to allow close-packing of the 7 modules in each cryostat. The antenna backshort and readout mounting plate are then installed (g), allowing the LC boards to be attached (h), completing the module.

An important feature of the assembly process is a room temperature electrical check of the wafer after it has been wirebonded but before the channelizing resonators have been attached. A time-division multiplexed resistance measurement system was developed which automatically sweeps through connections of interest on a single multiplexer module via the FPC connector at the end of the off-wafer flexible cable. Motivated by the most common fabrication faults, the resistance between each pair of TES leads, the resistance to nearest-

neighbor leads, and the resistance to the ground plane are measured. All 3,570 resistances per wafer may be measured within a matter of a few hours, limited by a combination of the auto-ranging functionality of the commercial multimeter in use and by the repetitive nature of disconnecting and reconnecting the flex cables into the measurement interface board. From this resistance data, shorts are identified and manually removed by disconnecting their associated wirebonds.[10] Additionally, maps such as the one shown in Figure 3.7(a) and long-term trends as shown in Figure 3.7(b) are produced, which provide valuable feedback for the fabrication team.

The structure in which the detector modules are collectively mounted is called the focal plane tower (FPT), so-called due to its multi-tiered structure. Originally, the structure shown in Figure 3.8(a) was designed for the POLARBEAR-2a instrument. As the design of the Simons Array progressed, however, the mass of the detector array to be supported and the thermal loads incident upon the sorption fridge heat sinks increased. To alleviate these, the stiffer, more insulating structure shown in Figure 3.8(b) was designed. The POLARBEAR-2b and POLARBEAR-2c cameras will use this structure, and furthermore in late 2020 it was also retrofitted into POLARBEAR-2a. While POLARBEAR-2a did perform initial commissioning observations with the original FPT, the following descriptions apply only to the replacement FPT.

The FPT is a multi-stage thermal isolation structure which is thermally anchored to each substage of the millikelvin fridge and provides thermal intercepts for the detector wiring and a radio frequency (RF) shield at 4 K, 1-2 K,[11] 350 mK, and 250 mK. Additionally, there is a 350 mK stage where the final IR bandpass metal mesh filters (MMFs) are located [50]. Thermal isolation of each stage is provided by carbon fiber rods which are epoxied to aluminum 6061 (Al6061) alloy feet. The 1 K ring and 350 mK rings are made of Al6061 as opposed to copper to minimize weight and thermal mass while maintaining structural strength. The bolometer stage (250 mK) is made from copper 101 (C101) alloy. The majority of all metal parts, excluding the Al6061 carbon fiber feet, is plated with gold to a thickness of 1.27 μm to reduce emissivity and increase the contact conductance of the heatstraps anchoring each FPT stage to its corresponding millikelvin fridge substage.

3.3 Cryogenic design

The cryogenic design of the FPT was motivated by both "AC" and "DC" concerns. At "AC", one desires to avoid coupling vibrations to the cold stages which can cause microphonic heating during observations. At "DC", it must provide sufficient isolation to its contents

[10] Unintended low-impedance paths for current in the cryogenic circuit stand to overload the SQUID amplifier. This can result in the loss of all 40 channels within a multiplexer, so the conservative approach of removing every discovered short was chosen.

[11] The POLARBEAR-2a fridge provides a heat sink closer to 2 K, while the POLARBEAR-2b and POLARBEAR-2c fridges provide heat sinks closer to 1 K.

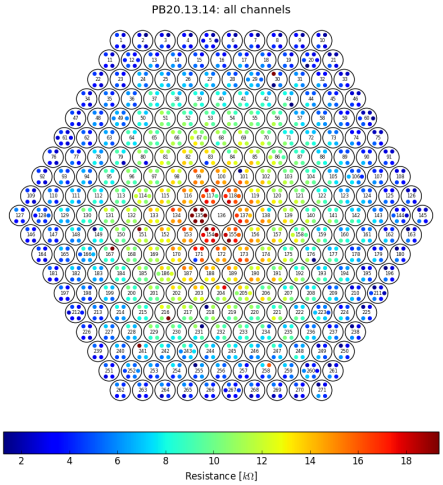

(a)

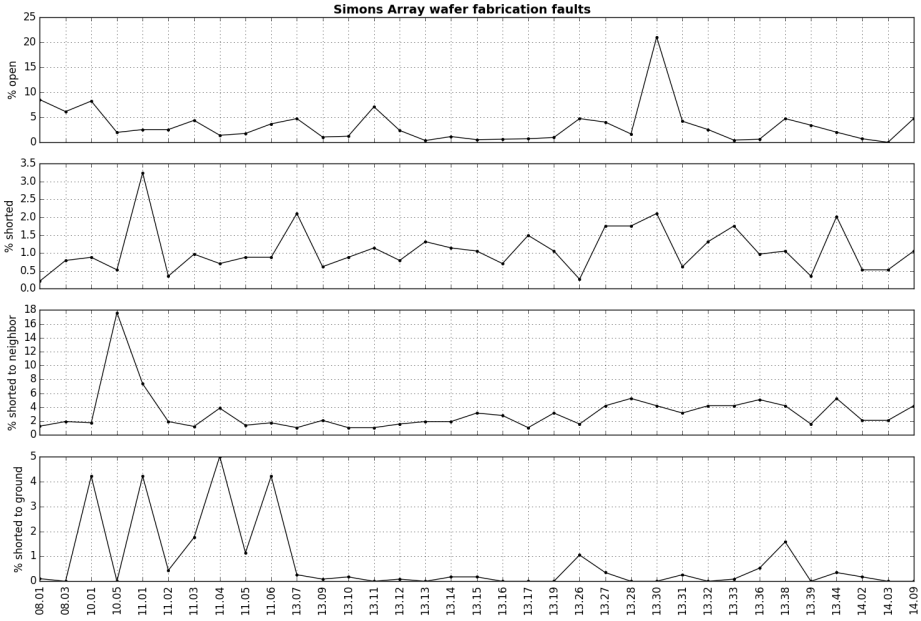

(b)

Figure 3.7: Example analysis outputs from the room temperature wafer screening procedure. (a) shows a map of the measured channel resistances, which at room temperature are dominated by the normal-state Nb traces which decrease in length radially across the wafer. Several outliers are visible by eye, and are later addressed by manually removing the associated channel wirebonds. (b) demonstrates the capabilities of this system to track both short-term and long-term trends in wafer fabrication. As an example, the switch from silicon oxide as a microstrip dielectric material to silicon nitride is clearly visible as a drastic reduction in the number of ground plane shorts between wafer versions 11 and 13.

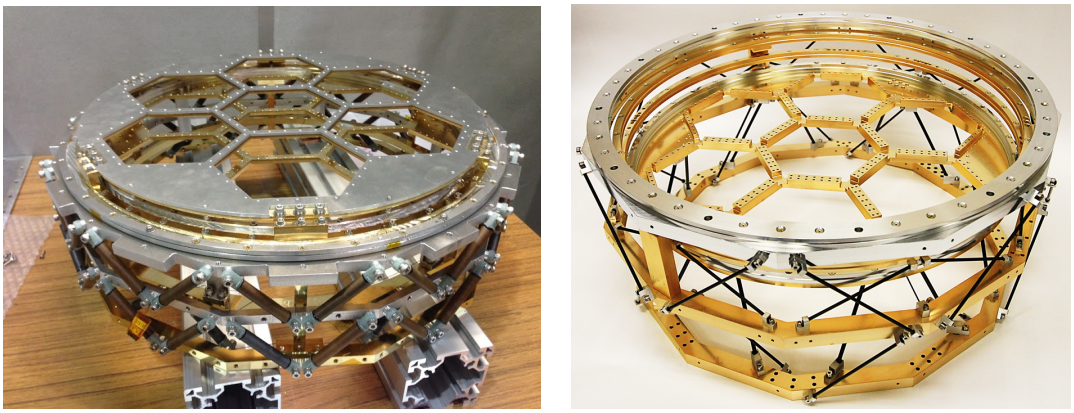

(a) (b)

Figure 3.8: Pictures of the mechanical support structures which hold the 7 detector modules in each cryostat and thermally insulate them from the $T \approx 4$ K cryostat environments. The image in (a) shows the structure used for initial commissioning of POLARBEAR-2a. The image in (b) shows the structure installed in POLARBEAR-2a in late 2020 and that is used in POLARBEAR-2b and POLARBEAR-2c. Pictures courtesy of (a) Masaya Hasegawa and (b) of Aritoki Suzuki.

that the millikelvin refrigerator can sustain a cold duty cycle consistent with high observing efficiency of the CMB.

The cryostat at large is expected to act as a low-pass filter for external vibrations coupling in to the FPT, as the masses of the 50 K and 4 K shells are large and the G10 supports on which they are mounted are relatively few.[12] The FPT was designed to be significantly stiff as to have a first mechanical resonance above the cutoff of the cryostat. Determining in advance the resonance requirements of the structure is extremely nontrivial given the complexity of the cryostat environment and poorly constrained vibration spectrum of the telescope; the design choices were made to simply maximize the FPT resonance frequency while simultaneously satisfying its thermal and spatial constraints.

The mass of material cooled to 250 mK in each Simons Array cryostat is approximately 15 kg. Furthermore, the spatial extent of the channelizing resonators which are mounted behind the detector wafers covers nearly all the available room inside the cryostat volume along the optical axis. Moreover, limited radial room exists for the FPT - only a few centimeters of radial extent is possible given the inner cryostat volume. Given these immediate constraints, a wedding cake truss design was chosen to maximize the bracing of the detector array both parallel to the optical axis and perpendicular, where it will necessarily be weaker. Struts consisting of pultruded carbon fiber tubes and rods were found in the design phase

[12] As a toy model, one can think of the cryostat inner shell as having a "large" mass m and its G10 mountings having a "small" spring constant k, in which case the resonant frequency $\omega = \sqrt{k/m}$ is "small".

to perform better than the commonly used DuPont Vespel[13] plastic.

The mechanical verification of the resulting FPT design is shown in Figure 3.9. During the design phase, finite element method simulations of the structure were performed in SolidWorks[14], predicting side-to-side and drum-like resonances at 70 Hz and 100 Hz. The actual fabricated FPT was then assembled with a test mass in place of the copper mounting plate onto which the detector modules bolt which matched the total mass of the detector array, and a shake table test resulted in measured resonances about 15% lower than simulated. Similar accuracy was found for simulations of similar truss structures, and is attributed to the simplistic nature of the CAD model required for convergence of the simulations.

The thermal design of the FPT is driven primarily by the conductive heat leaks it and its contents present to the heat sinks of the sorption refrigeration system. The rate of heat transfer dQ/dt onto a heat sink due to heat leaks through mechanical supports, cables, etc. is straightforward to model so long as the material properties and geometry are known. In the case of steady-state 1-dimensional heat conduction, Fourier's law implies that

$$\frac{dQ}{dt} = \kappa A \frac{dT}{dx} \tag{3.15}$$

where κ is the material thermal conductivity, A its cross-sectional area, and x the spatial dimension of interest. In most cases of interest, the low-temperature thermal conductivities of materials are strong functions of temperature; since a temperature gradient builds up across the material, it is usually the case that $\frac{d\kappa}{dx} \neq 0$. Integrating (3.15) gives

$$\frac{dQ}{dt} = \frac{A}{L} \int_{T_{low}}^{T_{high}} \kappa(T') dT' \tag{3.16}$$

where L is the support or cable length and T_{low} and T_{high} are the temperatures of either end - typically held fixed by refrigeration system heat sinks. For known material conductivities, material geometries, and heat sink temperatures, then, one may model the resulting heat leaks and compare to the measured capabilities of the refrigeration system.

The capabilities of the Simons Array millikelvin refrigeration systems have all been separately measured, resulting in known approximate relationships between the fridge hold time and the thermal power incident on each head. Together with a target hold time, these set requirements on the allowable conductive heat leaks due to the FPT and its contents. As discussed in Section 2.2.4, the cooling systems differ somewhat between POLARBEAR-2a, POLARBEAR-2b, and POLARBEAR-2c; combined with differing hold time targets, these set varying thermal requirements on the millikelvin hardware. Furthermore, the requirements are not particularly strict; the overall driver is the desire to lock daily observations to the rising and setting of the CMB patch, and one may always extend the duration of the fridge recycling procedure to meet a daily (or several day) schedule. Nevertheless, these soft targets are tabulated next to the modeled values in Table 3.1.

[13] https://www.dupont.com/products/vespel.html

[14] https://www.solidworks.com/

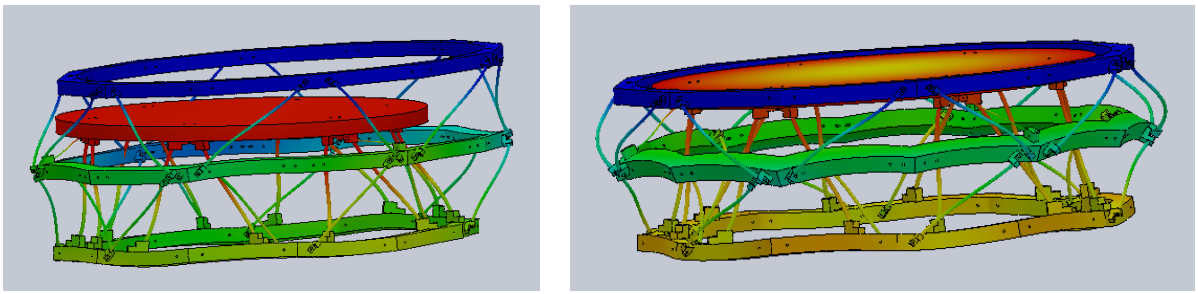

(a) (b)

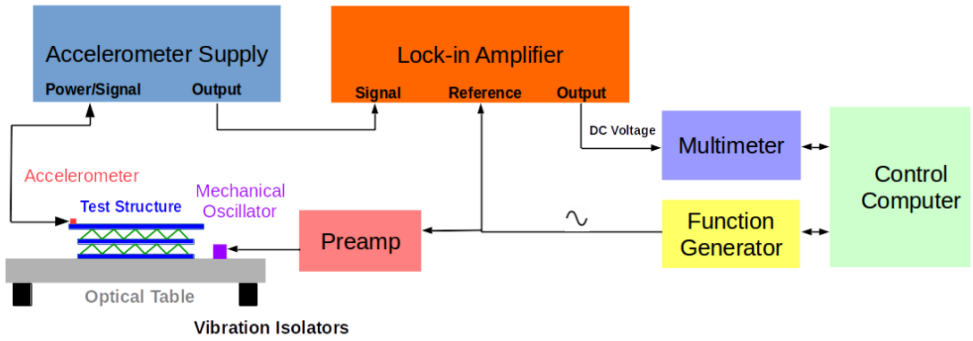

(c)

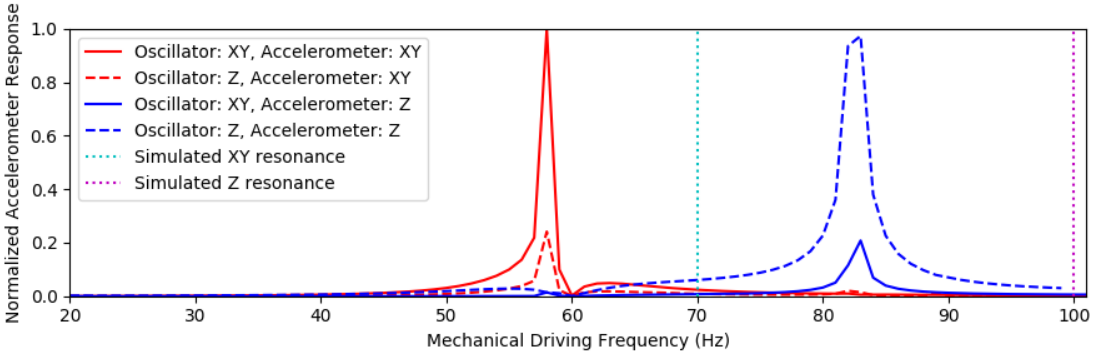

(d)

Figure 3.9: Simulation and measurement of the focal plane support structure's mechanical resonances. Finite element analysis simulations of a simplified model of the detector array were performed, predicting (a) a first resonance at 70 Hz involving a side-to-side shaking of the detector array and (b) a drum-like oscillation along the optical axis. Both illustrations of the resonant modes are shown with exaggerated scales for clarity. A schematic of the laboratory measurement setup used to verify these simulations is shown in (c), and the measured resonances are compared to simulation in (d). The lowest frequency resonances measured were indeed side-to-side and drum-like modes as expected, but at frequencies about 15% lower than simulated.

Overall, the loads on the millikelvin refrigerator may be divided into conductive loads and radiative loads. Three components contribute to the millikelvin conductive loading: the mechanical supports in the FPT, the readout cables, and the RF shield. By design, thermal radiation from elements internal to the cryostat is negligible, but radiation from the atmosphere that passes through the telescope optical chain is incident on various millikelvin components and contributes non-negligible loading.

The supports of the FPT are a combination of pultruded carbon fiber tubes manufactured by vDijk Pultrusion Products* [15] (DPP) and rods of the commonly used Graphlite pultruded carbon fiber. The cryogenic thermal conductivity of Graphlite has been well-measured [62, 63], but that of DPP was not known at the time of design. To verify this material, measurements of thermal conductivity along the tube axis were performed in the desired temperature range. Known amounts of power P_{app} were applied to one end of a sample and the resulting equilibrium temperature T_{high} was measured, while the other end was fixed at a base temperature T_{low} (see Figure 3.10 for a schematic). The thermal conductivity of DPP was found to be well approximated by a power law

$$\kappa(T) = \alpha T^{\beta}, \tag{3.17}$$

and the coefficient α and index β were obtained by fitting to Eq. (3.16). Due to cooling power limitations of the adsorption fridge used for testing, measurements were performed with $T_{low} \sim 300$ mK from a single-shot He-3 adsorption refrigerator, and separately with $T_{low} \sim 1.2$ K from pumped liquid He-4. The best fit in the 0.25 K—2 K range is $\kappa_{DPP}(T) = 4.17\ T^{1.21}$ mW/m·K, and the best fit in the 1.4 K—4.5 K range is $\kappa_{DPP}(T) = 7.59\ T^{0.61}$ mW/m·K.

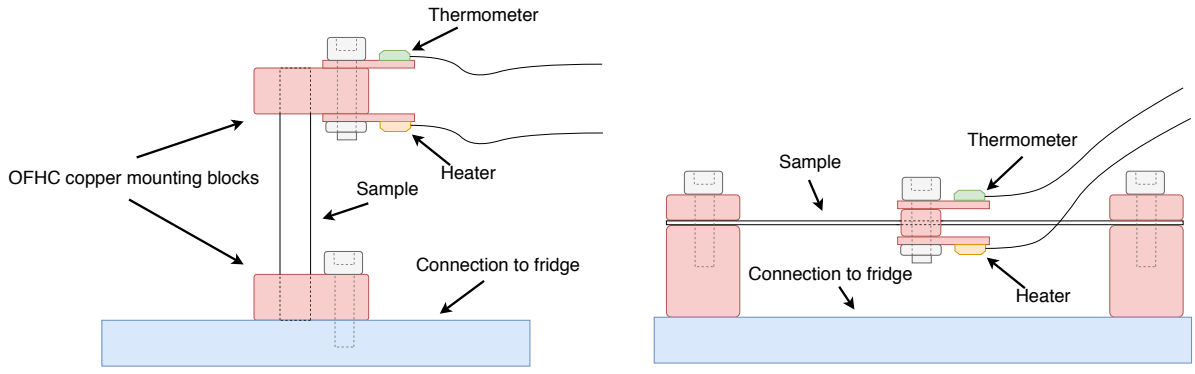

(a) (b)

Figure 3.10: asdf asdf be sure to cite Logan's SPIE

The readout cables are fabricated from a custom stack-up of polyimide, superconducting NbTi, photoresist, and adhesive layers. Although cryogenic thermal conductivities of poly-

[15] http://www.dpp-pultrusion.com/

imides and NbTi have been measured [64, 65], building an accurate thermal model of the combined cable is subject to large errors due to uncertainty in the properties of the remaining materials. Thus, a measurement of the cryogenic thermal conductivity of the readout cables was performed in a manner similar to that described above. Since the cables are flexible, they were held taut and clamped on opposite sides at T_{low}, while a central clamp with a heater and thermometer was used to apply power (see Figure 3.10). As the cross-sectional area of the cables is fixed but the distance between thermal intercepts in the FPT is not, the relevant quantity of interest is the thermal conductance per unit length, G/L. The best fit in the 0.25 K—1.5 K range is $G/L = 7.1\ T^{1.79}\ \mu$W/mm·K, and the best fit in the 1.4 K—6 K range is $G/L = 9.3\ T^{1.05}\ \mu$W·mm/K.

The RF shield is comprised of 300 Å of aluminum deposited on a 6.35 μm sheet of polyethylene terephthalate. The strong dependence of the cryogenic thermal conductivity of aluminum films on their purity motivated a measurement of a sample of the RF shield in a manner similar to that of the readout cables. Due to the sample's long time constant for equilibration and fridge hold time limitations, measurements were only performed in the 1.4 K—6 K range. Since the thermal conductivity will decrease more strongly below the critical temperature of the aluminum film, extrapolating measurements from this range provides an overly pessimistic estimate of the thermal loads at colder temperatures. Moreover, as the RF shield extends radially as well as vertically away from the focal plane, the relevant quantity of interest is the thermal conductivity multiplied by the thickness d of the shield, κd. The measured best fit is $\kappa d = 33.5\ T^{1.41}$ nW/K.

Optical loads which contribute to the thermal loading of the adsorption fridge include out-of-band radiation absorbed by the 350 mK metal mesh filter and in-band radiation absorbed by emissive lenslets on the focal plane. The particular estimation of these loads depends on the specifics of the optical design (and therefore differ between POLARBEAR-2a, POLARBEAR-2b, and POLARBEAR-2c), which will be detailed in an upcoming publication. For the purposes of estimating the thermal budget, conservative upper limits are quoted here.

A summary of the expected thermal loads on the He-10 fridge substages is given in Table 3.1. All conductive loads were calculated according to Equation (3.16) with known geometries and with temperatures measured from a cooldown with realistic thermal loads applied to each fridge intercept via resistive heaters.

As the POLARBEAR-2a cryostat was only recently retrofitted with the new FPT design hardware, it is too soon to comment on its thermal performance. A discussion of the thermal performance of the previous FPT design originally installed in POLARBEAR-2a is presented in Chapter 5. Nevertheless, laboratory characterization of the POLARBEAR-2b integrated cryogenic receiver has demonstrated sufficient hold time to operate on a 2-day sidereal schedule.

	Supports	**Cables**	**RF shield**	**Radiation**	**Total**	**Target**
2 K (POLARBEAR-2a)	13.4	36.4	25.8	0	75.5	<100
1 K (POLARBEAR-2b)	13.8	40.6	21.3	0	76.1	<150
1 K (POLARBEAR-2c)	13.8	40.6	21.3	0	76.1	<150
	4.9	9.3	5.5	<4.8	<24.5	<65
350 mK	0.8	1.8	0.9	<4.8	<8.3	<20
4.9	9.3	5.5	<4.8	<24.5	<65	
350 mK	0.8	1.8	0.9	<4.8	<8.3	<20
	0.8	1.8	0.9	<6.7	<10.2	<20
	0.2	0.3	0.1	<1.7	<3.1	<5
250 mK	0.3	0.1	0.1	<1.7	<2.0	<5
	0.3	0.1	0.1	<3.5	<3.8	<5

Table 3.1: Projected thermal loads in μW on the fridge intercepts in POLARBEAR-2a, POLARBEAR-2b, and POLARBEAR-2c (from top to bottom of each cell). In POLARBEAR-2a, the first intercept is at the heat exchanger at $T \approx 2$ K, POLARBEAR-2b and POLARBEAR-2c have separate He-4 reservoirs at $T \approx 1$ K. The targets were set by specifying that the sum of the hold time and recycling time exceed 24(72) hours for POLARBEAR-2a(POLARBEAR-2b and POLARBEAR-2c).

Chapter 4

Digital Frequency Division Multiplexed Readout

Hand-in-hand with the challenge of coupling more detectors to the sky for CMB observations are the tasks of operating and reading them out. As a result, detector readout is a driving technology for the field. The Simons Array collaboration, together with the SPT-3G collaboration, took on the task of developing a new readout system to incorporate the large increase in detector count relative to preceding instruments. This chapter describes said readout system, with particular focus on the cryogenic circuit components.

4.1 Overview

Conceptually, the electronics accompanying the detectors in a CMB experiment need only satisfy two requirements: they must provide adjustable voltage biases to the TES bolometers, and they must measure the time-dependent TES currents, eventually representing them as sequences of floating-point numbers in computer memory. Practically, however, they must interface with $\mathcal{O}(10^4)$ detectors cooled to $T \approx 0.3$ K at the center of a spatially constrained cryostat while maintaining a reasonably small footprint in the overall project budget and labor requirements. The prospect of 2 bias wires and 2 readout wires for each detector is simply untenable, and drives one to multiplex - combine many signals over a reduced number of wires - to manage complexity, reduce costs, and minimize the heat handling requirements on the refrigeration systems. All modern CMB instruments now incorporate multiplexed electronics, and along with the general trend of increasing detector counts, the multiplexing capabilities for CMB readout are also improving over time as the result of a great deal of development effort.

The Simons Array readout system is based on digital frequency-division multiplexing (DfMux). The DfMux scheme works by combining the bias and readout functions by utilizing a AC voltage biases for the TES bolometers. Specifically, the bias is of the form

$$V_{bias}(t) = V_b \sin(\omega_b t) \tag{4.1}$$

where a bias frequency ω_b is chosen to be much faster than the detector thermal time constant

$$\omega_b \gg \frac{2\pi}{\tau} \tag{4.2}$$

so that the electrical power seen by the detector is the time average over many cycles of the bias

$$P_{elec} = \frac{V_{bias}^2}{R_{TES}} = \frac{V_b^2 \langle \sin^2(\omega_b t) \rangle}{R_{TES}} = \frac{\frac{1}{2} V_b^2}{R_{TES}} = \frac{V_{bias,\,RMS}^2}{R_{TES}}. \tag{4.3}$$

In the Simons Array, typical values for $2\pi\omega_b$ are in the 1–5 MHz range, while typical values for $1/\tau$ are in the 100–1000 Hz range, easily satisfying (4.2). The treatment of AC voltage biased TES bolometers is then nearly identical to that given in Chapter 3, with the occasional prefactor factor of 2 or $\sqrt{2}$ in some equations.

Crucially, the AC bias gives rise to amplitude modulation of the bias tone by the low-frequency detector signal. The conductance $\sigma(t) \equiv \frac{1}{R_{TES}(t)}$ of a TES bolometer will consist of a constant part σ_0 that is merely a function of the depth in the superconducting transition to which it is biased and a time-varying part $\sigma_1(t)$ as a result of the changing optical signal:

$$\sigma(t) = \sigma_0 + \sigma_1(t). \tag{4.4}$$

When biased with a voltage of the form (4.1), the resulting current is

$$\begin{aligned} I(t) &= V_{bias}(t)\sigma(t) && (4.5)\\ &= V_b \sin(\omega_b t)(\sigma_0 + \sigma_1(t)) && (4.6)\\ &= (I_0 + I_1(t)) \sin(\omega_b t) && (4.7) \end{aligned}$$

which is the waveform for an amplitude-modulation of a carrier at frequency ω_b by a signal $I_1(t)$. To demonstrate the multiplexing utility of amplitude modulation, consider the simplistic scenario where $I_1(t)$ contains only a single Fourier component at frequency ω_s:

$$I_1(t) = I_1 \cos(\omega_s t). \tag{4.8}$$

In this case, the resulting TES current is

$$\begin{aligned} I(t) &= I_0 \sin(\omega_b t) + I_1 \cos(\omega_s t) \sin(\omega_b t) && (4.9)\\ &= I_0 \sin(\omega_b t) + \frac{I_1}{2} \left[\sin((\omega_b + \omega_s)t) + \sin((\omega_b - \omega_s)t) \right], && (4.10) \end{aligned}$$

demonstrating that the signal becomes encoded in the sidebands of the carrier, each containing half the amplitude of the original signal. This phenomenon is further illustrated in Figure 4.1 for the more realistic case of signals with nontrivial frequency content. By biasing each detector at a unique frequency, the sidebands of each carrier can be chosen to be non-overlapping in frequency space, enabling them to be unambiguously combined over a single cable run, which is the goal of multiplexed readout.

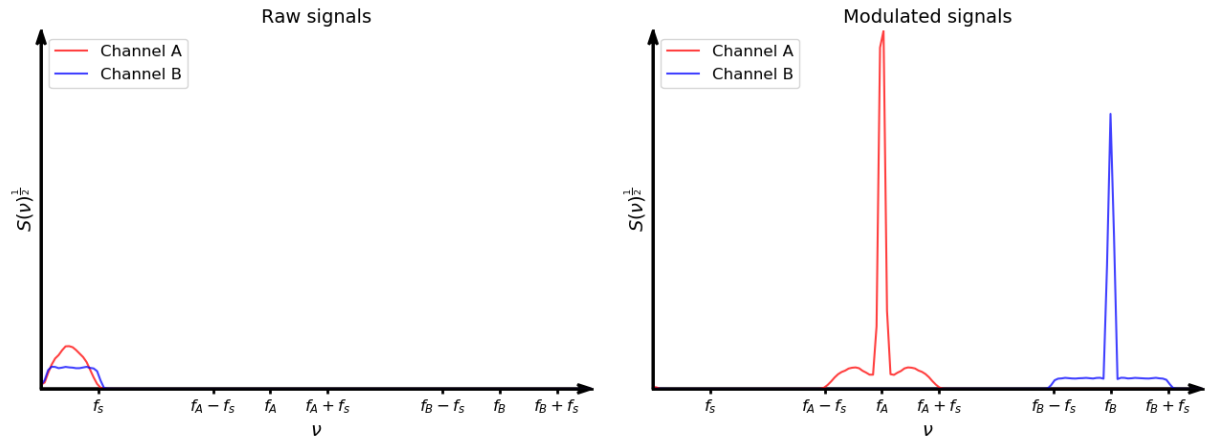

(a) (b)

Figure 4.1: A toy model demonstrating amplitude modulation in frequency space. The overlapping spectral densities of signals from two hypothetical channels are shown in (a). After amplitude-modulating carrier tones with frequencies f_A and f_B, the modulated signals shown in (b) no longer overlap spectrally and may be combined on a single conductor pair.

It is worth noting in these examples that because the sky signals result in only small perturbations to the TES resistances, the power in the carrier tone is much larger than the power in the signal (i.e. $I_0 \gg I_1$ and the central peaks at f_A and f_B in Figure 4.1(b) are large compared to their sidebands) even though it contains no science information. This imbalance has important ramifications for the dynamic range of the post-modulation amplification components, and will be discussed further shortly.

In the current DfMux implementation, the detector bias tones are produced at room temperature, where they may be conveniently generated away from the spatial and thermal constraints of the cryostat. Custom FPGA-based digital electronics handle both the tone generation and demodulation [66], [67]. In order to channelize the system, each detector is wired in series with a narrow bandpass filter which acts like a short at the detector bias frequency and an open at other frequencies. This way, individual wiring for each detector is only required isothermally at the coldest refrigeration stage inside the cryostat. A conceptual schematic of this frequency-division multiplexing scheme is depicted in Figure 4.2(a).

Physically, the bandpass filters are implemented with LC resonators, as shown in the electrical schematic in Figure 4.2(b) and described further in Section 4.3. To enforce that the bias carriers are stiff voltage sources, a shunt resistor with $R_{shunt} \ll R_{TES}$ is placed in parallel with the network of detectors and LC resonators. To minimize Johnson noise, this shunt resistance is located inside the cryostat at $T \approx 4$ K. Also inside the cryostat at $T \approx 4$ K is a transimpedance amplification stage formed by a superconducting quantum interference device (SQUID) array, described further in Section 4.4.

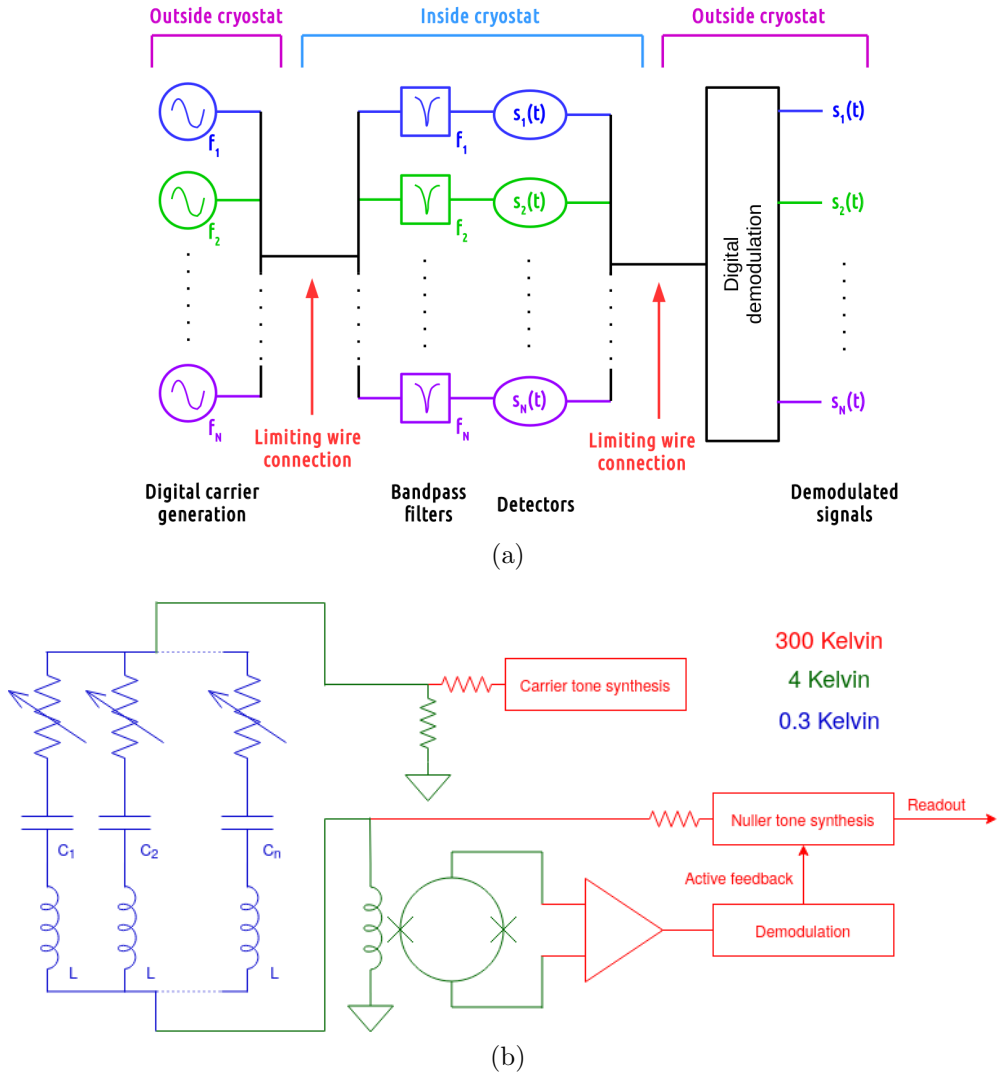

Figure 4.2: Conceptual (a) and electronic (b) schematics of the readout system employed in the Simons Array and SPT-3G experiments.

While SQUID arrays provide a good solution for the necessary cryogenic TES current sensing, they are nonlinear devices with limited dynamic range. As such, they are typically operated with some kind of feedback, and the current DfMux implementation is no exception. Stable analog feedback was not deemed feasible at ∼MHz frequencies with realistic cryogenic wiring, which contributes large frequency-dependent phase shifts from parasitic reactances. Instead, digitally-generated active feedback only applied in narrow frequency ranges centered on the carrier tones, was incorporated into the design. This digital active nulling (DAN) feedback nulls the input to the SQUID array, using the SQUID array only as an error monitor,

greatly enhancing the linearity and dynamic range, and extending the usable bandwidth of the entire system [68].

4.2 Context

The Simons Array readout is not the first frequency-division multiplexed TES readout system; DfMux was first used for scientific observations in the APEX-SZ and SPT SZ experiments [69], and the current version builds on an intermediate implementation used in the POLARBEAR [22] and SPTpol [70] experiments. The current iteration of DfMux readout was developed simultaneously for the Simons Array and SPT-3G [21] experiments; minor differences exist between the Simons Array and SPT-3G implementations, but for the most part they are the same. The most notable upgrades and updates to the current DfMux design from the POLARBEAR/SPTpol design are:

1. The multiplexing factor of 8x(12x) in POLARBEAR(SPTpol) was increased to 40x(68x) in the Simons Array(SPT-3G).
2. The carrier frequencies were increased from 0.3–1 MHz range to the 1–6 MHz range.
3. The SQUID array feedback paradigm was changed from a broadband flux-locked loop scheme to DAN.
4. The fabrication of the channelizing resonators was migrated to a fully lithographed, monolithic design in comparison to the previous mix of lithographed inductors and commercial surface mount capacitors

Some differences between the Simons Array and SPT-3G implementation may be worth noting. To achieve the larger multiplexing factor of 68x, SPT-3G utilizes more bandwidth: the maximum frequency channel is 5.2 MHz whereas in the Simons Array it is 4.6 MHz. The resonator chip designs also differ slightly in capacitor design and overall dimensions. Moreover, the operating resistance of the TES bolometers differs between the two experiments. The remainder of this chapter focuses on the Simons Array implementation; while most of it is applicable to SPT-3G, some specifics of crosstalk and noise will differ.

Currently, future iterations of DfMux readout are being developed [71], [72] for use in the LiteBIRD satellite [29] and possibly the CMB-S4 experiment [28]. A separate group is implementing a version of DfMux readout most similar to the POLARBEAR/SPTpol implementation independently for the LSPE/SWIPE experiment [73]. Additionally, another group is developing a similar system to DfMux to read out large arrays of TES calorimeters [74], [75].

Aside from DfMux, other multiplexing paradigms have been used to read out TES detectors and also show promise for future CMB observations. The first multiplexed TES readout and competitor to DfMux readout for the past several decades has been time-division multiplexed (TDM) readout, which reads out detectors in sequence using SQUID-based switches and has been used for multiple CMB experiments with a multiplexing factor of up to 64x

[76]. Another scheme in which detector signals are encoded using more general orthogonal functions, code-division multiplexing, has not been used for CMB observations but presents an alternative [77]. A new method in which TES signals modulate the resonance frequencies of microwave resonators via RF SQUIDs - the microwave SQUID multiplexer (μMux) - has been under recent development to achieve very large multiplexing factors [78], will be soon deployed in the Simons Observatory [79], [80] and AliCPT [25] experiments, and has been partially demonstrated with a retrofitted Keck Array camera [81]. In the future, hybrid techniques could be used to further utilize the available bandwidth of a microwave SQUID multiplexer [82].

4.3 Channelizing filters

As mentioned in Section 4.1, the bandpass filters which allow the AC bias tones to uniquely address single detectors are constructed from an inductor and capacitor wired in series with each TES.

4.3.1 Operating principle

To demonstrate how a series RCL combination forms a bandpass filter, one may compute the magnitude of its impedance:

$$|Z_{RCL}| = \left| R_{TES} + i\omega L + \frac{1}{i\omega C} \right| \tag{4.11}$$

which at the resonance frequency $\omega_r = (LC)^{-1/2}$ is simply the TES resistance R_{TES}. Away from ω_r, $|Z_{RCL}|$ diverges quickly. Thus, the LC resonator looks like a short on resonance and an open off resonance. The filter "pass" region may be understood by considering the frequencies above and below ω_r at which $|Z_{RCL}| = 2R_{TES}$:

$$\omega_+ = \frac{\sqrt{3}R_{TES}}{2L} + \sqrt{\frac{3R_{TES}^2}{4L^2} + \frac{4}{LC}} \tag{4.12}$$

$$\omega_- = -\frac{\sqrt{3}R_{TES}}{2L} + \sqrt{\frac{3R_{TES}^2}{4L^2} + \frac{4}{LC}}. \tag{4.13}$$

The frequency range $\Delta\omega$ within which the net impedance is "small" is then

$$\Delta\omega = \frac{\sqrt{3}R_{TES}}{L} \tag{4.14}$$

which notably is independent of the resonator capacitance. To keep the channel bandwidth constant for all the channels in a multiplexer, each resonator has the same inductance ($L = 60\ \mu$H) while the capacitance varies (20 pF $< C <$ 160 pF).

To form a full multiplexer, the TES-resonator series combinations are all wired in parallel, as shown in Figure 4.2(b). The parallel impedance of such a combination is shown for a real "comb" (so-called due to the shape of its impedance-frequency relation) in Figure 4.3. Practically, the component value choices for L and C are determined by several factors: the maximum feasible physical size, the maximum usable frequency, stability requirements for the TES bolometers (discussed in Section 4.6), and crosstalk requirements (discussed in Section 4.7). It should be noted that the impedance shown in Figure 4.3 has a maximum of $|Z_{comb}| \leq 20\ \Omega$; this is due to the parallel combination of a 20 Ω resistance with all the RCL legs whose function is to damp out an expected resonance formed by the ∼70 nH SQUID array input coil and the ∼1 nF parasitic capacitance of the cabling that connects the 250 mK hardware to the SQUID arrays.[1]

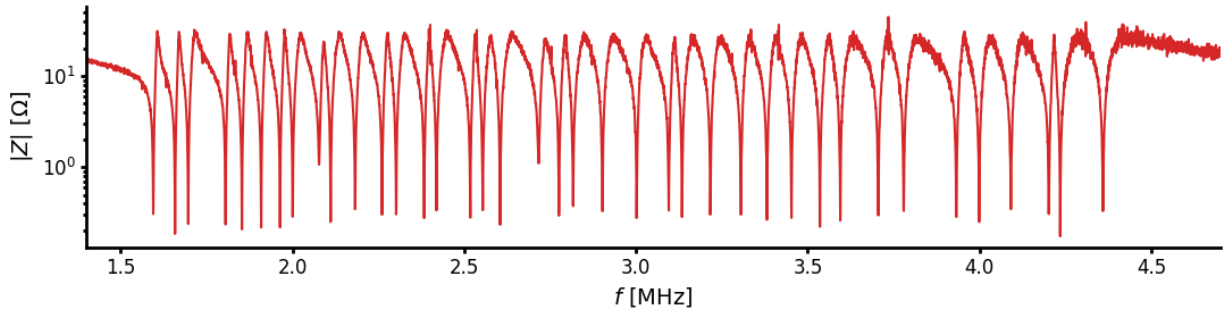

Figure 4.3: Magnitude of the impedance of the cryogenic parallel network for a Simons Array multiplexer module, measured across the "warm" ($T \approx 4$ K) ports of the NbTi cable. For this measurement, the TES bolometers were in a superconducting state; the resonance depths are then a measurement of the equivalent series resistance (ESR) in the cold circuit. The two 1 Ω calibration resistors are visible by eye at approximately 2.1 MHz and 2.7 MHz. A total of 39 out of 40 resonances were yielded in this module.

4.3.2 Physical implementation

The channelizing filters are physically fabricated in one monolithic chip containing the 40 resonators for a single readout module, as shown in Figure 4.4. The inductor and capacitor components are planar structures fabricated from a superconducting film. To allow for a single-layer fabrication process, the inductors are spiral inductors which require a wire bond to complete, and the capacitors are interdigitated capacitors. Two chips each are adhered and bonded to opposing sides of a custom printed circuit board, which is mounted directly

[1]The original build of resonators used for commissioning of POLARBEAR-2a through the 2019 season actually only had these damping resistors on a small fraction of the multiplexers, but they were added during the 2020/2021 refurbishment operation (see Chapter 5). The POLARBEAR-2b and POLARBEAR-2c multiplexers all incorporate this 20 Ω damping resistance.

behind the detector wafer at $T = 0.3$ K as described in Chapter 3, so that a total of 105 LC board assemblies are cooled in each Simons Array cryostat. This circuit board forms the beginning of the parallel RCL network; the bias tones and modulated signals are split and combined on the right side of the board as indicated in Figure 4.4. Each mounting board contains 5 layers: 1 central ground plane, 2 middle layers for routing lines underneath the LC chips, and 2 top layers for routing connections to and from the LC chips. A superconducting magnetic shield - fabricated from alloy 6061 aluminum - and a superconducting chip back plane - fabricated from the resonator film material - control the inductor fringing fields, preventing inter-module crosstalk and eddy losses in nearby normal metals. 38 of the 40 channels connect to TES bolometers via a commercial FPC connector[2] and the flexible tinned copper cables bonded to the TES wafer described in Chapter 3. The remaining 2 channels connect to 1 Ω surface mount resistors directly on the LC mounting board; these are used for calibration and debugging purposes.

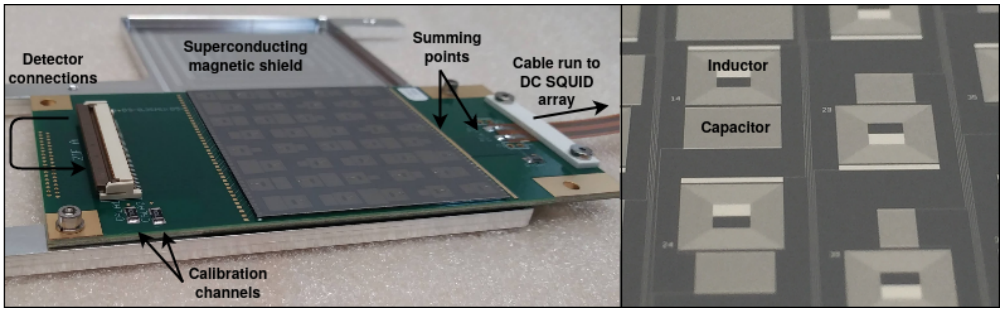

Figure 4.4: Annotated image of the LC resonators for a Simons Array readout module along with their packaging.

The LC chip fabrication process is relatively straightforward compared to that of the TES wafers. A negative image of the traces is first lithographically patterned in a photoresist layer onto a bare silicon wafer. The metallic layers are then deposited on both sides of the wafer, after which a liftoff procedure removes the metallic coating on top of photoresist. Finally, the wafer is diced into chips and assembled onto mounting boards. The natural material choice for most lithographed superconducting wiring layers is niobium (Nb), as it has a high critical temperature ($T_c = 9$ K), is mechanically tough, and is heavily used in the fabrication of the TES wafers. However, due to fabrication difficulties early in the development process, aluminum (Al) was adopted instead for the first production batch. The fabrication procedure for these devices is described in further detail in [83]. As Al films are non-ideal for resonator construction for several reasons discussed presently, a fabrication procedure for Nb-based resonators was developed and used for later batches. The initial commissioning of the POLARBEAR-2a instrument used these original Al LC devices, and their characterization will be further detailed in Chapter 5. The 2020/2021 refurbishment

[2]Hirose Electric Co. Ltd. FH16-90S-0.3SHW(05)

of POLARBEAR-2a included a replacement of these Al devices with Nb devices, so the entire Simons Array will only contain Nb LC resonators going forward.

4.3.3 Kinetic inductance effects

An important aspect of the resonators was highlighted due to the initial aluminum build - the effect of kinetic inductance on the resonator properties. In a superconductor, the inertial mass of the charge carriers can contribute to the total inductance of a circuit element at AC frequencies. This effect is exploited purposefully for a range of devices [84], but is not desirable for the channelizing filters in DfMux readout. In particular, kinetic inductance has a nonlinear dependence on temperature, diverging near the superconducting transition temperature of the material. For small currents near T_c, it may be approximated in the Landau-Ginzberg theory as [85]

$$L_k(T) = L_k(0)\left(\frac{1}{1-\frac{T}{T_c}}\right) \tag{4.15}$$

so that the resonance frequency of an LC resonator with both geometric inductance L and kinetic inductance L_k becomes temperature dependent:

$$f_r(T) = \frac{1}{2\pi\sqrt{C\left(L + L_k(T)\right)}} \tag{4.16}$$

The quasiparticle density near T_c also results in additional resistive loss. In the Simons Array hardware, this is difficult to match to theory, as multiple aluminum alloys (Al 6061 in the magnetic shield, aluminum silicon for the wire bonds) are involved in the construction of the LCs, some of which may transition at slightly different critical temperatures and contribute to the overall loss near 1.2 Kelvin.

The effects of the aluminum resonator kinetic inductances are demonstrated in Figure 4.5. An observable frequency shift is evident even at temperatures just above the transition temperature of the TES bolometers (which is around 440 mK), posing minor operational challenges discussed further in Section 4.6. An additional concern is the low-frequency stability of the detector array - with the aluminum resonators operating at $T/T_c \approx 0.25$ during CMB observations, 1/f fluctuations in the refrigeration base temperature could compromise low-ℓ sensitivity at a level difficult to constrain in the lab. Additional loss is also observed, but only notably so at temperatures very close to the superconducting transition around 1.1 K. This loss is discussed further in Chapter 5. For these reasons, the niobium resonator build is used in POLARBEAR-2b and POLARBEAR-2c, and was eventually retrofitted into POLARBEAR-2a; niobium has a transition temperature of 9 K, so that during CMB observations, $T/T_c \approx 0.03$.

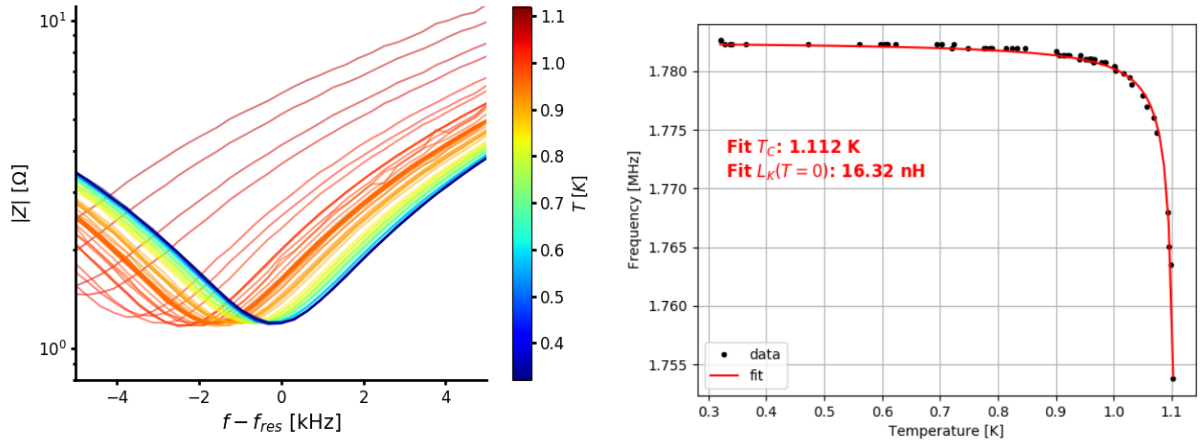

(a) (b)

Figure 4.5: Demonstration of the effect of the effect of kinetic inductance in the aluminum-based resonator build. The resonances are observed to shift downward in frequency and increase in loss as the temperature is raised, as shown in (a). The dependence on temperature is highly nonlinear, diverging at the superconducting transition temperature, as evidenced by the fitted curve in (b).

4.3.4 Two-level system coupling

Another physical phenomena new to the current version of DfMux readout is that of two-level system (TLS) noise. Superconducting lithographed microwave resonators are known to generically host fluctuating two-level tunneling states in amorphous dielectrics [84], [86]. The dielectrics may be residues from fabrication processes or even native oxide layers. As both the Al and Nb films in use form native oxide layers and no particular attention was paid to potential TLS-hosting layers during the fabrication process, there are several possible candidates for the manner in which the Simons Array resonators may couple to two-level systems. In microwave resonators with extremely high quality factors, parasitic TLS populations introduce a further temperature dependence into the resonant frequencies and losses of the resonators, though these effects have been constrained to be negligible for operations in the Simons Array resonators. The primary effect for DfMux readout of TLS coupling is their quantum mechanical fluctuations, which introduce a resonance frequency jitter. The characterization of this noise is discussed in detail in Section 4.8.

4.4 Cryogenic SQUID array amplification

Along with the LC resonators, another central circuit element in the DfMux readout system is the SQUID array ammeter. For noise reasons, a cryogenic amplification stage is typically

desired for TES readout, but the natural impedance of a thin-film superconductor is too low to be well-matched to a conventional transistor-based amplifier. SQUIDs - specifically DC SQUID arrays in this case - are a natural match with low input impedance, good noise properties, and relatively low power dissipation.

4.4.1 Principles of operation

A DC SQUID consists of a superconducting loop split into two halves by a pair of Josephson junctions, as drawn schematically in Figure 4.6. On its own, a DC SQUID loop can be used as a magnetometer, generating a voltage across the Josephson junctions in response to changes in magnetic flux through the loop. By intentionally coupling magnetic flux through the loop with an input coil inductor, a DC SQUID becomes an ammeter. Briefly, the operating principle of a SQUID combines the fact that magnetic flux through a superconducting loop is quantized in units of $\Phi_0 = \frac{h}{2e} \approx 2.07$ Wb and the fact that a Josephson junction can sustain both a supercurrent and a normal current, thereby maintaining flux quantization but developing a measurable voltage. A thorough treatment of DC SQUID theory is developed in [87].

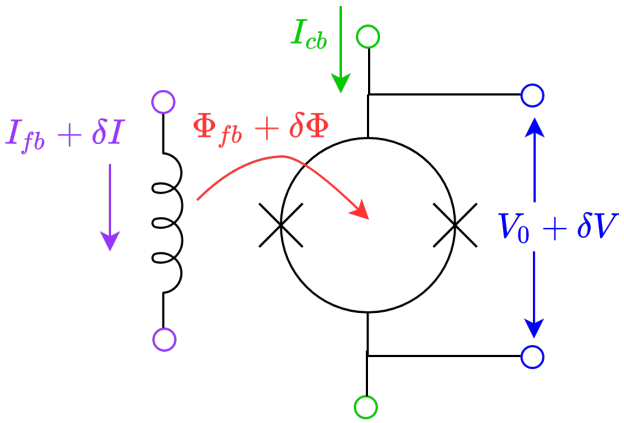

Figure 4.6: Conceptual schematic of a 6-port DC SQUID ammeter. An input coil inductor which is coupled to the main SQUID loop senses the signal current δI and is also used to apply a flux bias to the SQUID loop. The bias and signal currents induce an applied flux $\Phi_{fb} + \delta\Phi$ through the SQUID loop, which when given a proper current bias I_{cb} will induce a changing voltage $V_0 + \delta V$ across the SQUID junctions.

To operate a DC SQUID, it must be biased with a DC current I_{cb} exceeding the critical currents I_{crit} of the Josephson junctions. For $I_{cb} < 2I_{crit}$ (as the bias is split between the two), no voltage is able to develop across the junctions, as evident in Figure 4.7 for current

biases below 12 μA.[3] For $I_{cb} > 2I_{crit}$, the SQUID voltage responds to magnetic flux - or equivalently input coil current - in an approximately sinusoidal manner. As the current bias is further increased, the magnitude of the voltage swing decreases, resulting in a clear optimum current bias for sensitivity. The SQUID is also flux biased at a flux Φ_{fb} such that $dV/d\Phi$ (or equivalently dV/dI_{fb} as the flux bias is applied as a current via the input coil) is maximized. Biased in this manner, the SQUID measures fluctuations δI in the total current $I_{fb} + \delta I$ and transduces them to fluctuations δV on top of an offset voltage V_0. The coupling strength between the input coil and the SQUID loop is chosen such that, when operated with feedback[4] the fluctuations in flux are much smaller than a magnetic flux quantum.

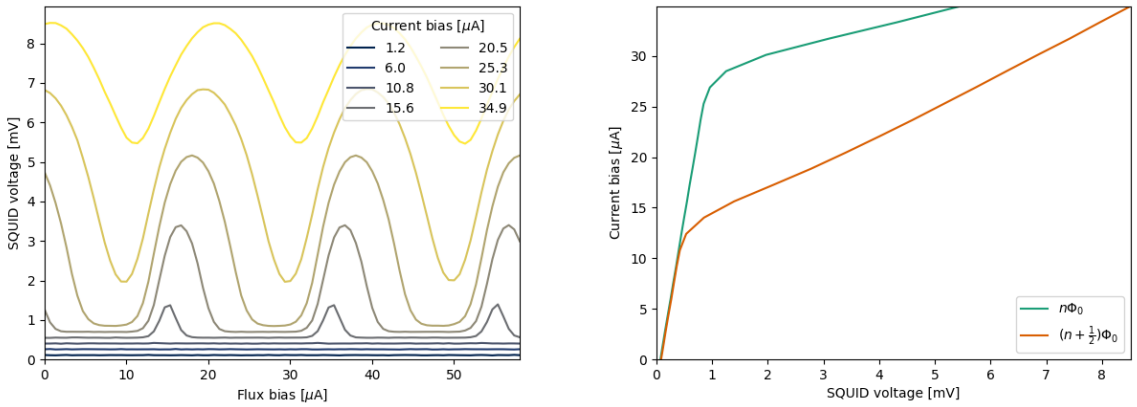

(a) (b)

Figure 4.7: The measured voltage-flux-current relationship for a Simons Array SQUID array. In (a), the relationship is shown at various fixed current biases I_{cb}, displaying the famous oscillatory voltage behavior of SQUIDs. In (b), the relationship is shown holding the applied flux at the values corresponding to integer and half-integer magnetic flux quanta through the SQUID loop. Together, these demonstrate that above a threshold current bias, the SQUID array transduces current through the input coil into voltage across the junctions. As the current bias is further increased, the peak-to-peak voltage swing is reduced, lessening the device sensitivity. These SQUIDs are slightly nonstandard in that they are asymmetric: the peaks and troughs of the $V - \Phi$ relation are not constant with I_{cb}, which has important electrical consequences as discussed in Section 4.8.

From an operational perspective, several parameters specify the role of a DC SQUID in the overall circuit. Since the SQUID is an amplifier, the input impedance (specified as an

[3]The careful reader will notice that a small, flux-independent voltage does develop, but this is due to parasitic resistances and not Josephson junction physics.

[4]In the case of the Simons Array DfMux readout, this is the Digital Active Nulling (DAN) feedback scheme.

inductance L_{in}), gain Z_{trans} (usually called the *transimpedance* as it takes a current input and outputs a voltage), and output impedance Z_{out} (often called the *dynamic impedance*) are of importance. Additionally, the values of the current and flux biases set requirements on the biasing electronics. Finally, the mutual inductance M between the input coil and the SQUID loop sets the scale of the periodicity of the input current to output voltage relationship. Typical values for the devices used in the Simons Array are given in Table 4.1.

Parameter	**Value**
L_{in}	50 nH
Z_{trans}	650 Ω
Z_{out}	750 Ω
I_{cb}	26 μA
I_{fb}	25 μA
M	25 μA/Φ_0

Table 4.1: Typical operational parameters for the SQUID arrays used in the Simons Array

4.4.2 Physical implementation

Practically, a single SQUID loop does not provide sufficient amplification for the purposes of DfMux readout. However, many SQUIDs may be combined in an array to improve their properties. Modern SQUID fabrication is sufficiently scalable to produce arrays of ∼100 SQUIDs. Combining SQUIDs in series notably increases their transimpedance, output impedance, input inductance, and noise. In parallel, the gain is unchanged while the input impedance, output impedance, and noise are decreased. More general combinations may be used for further optimization. In particular, the NIST SA13a SQUID arrays in use by the Simons Array contain 6 configurable banks of 64 individual SQUIDs in series. The configuration chosen is 3 series × 2 parallel [88].

Physically, the SQUID arrays are lithographically fabricated and diced into 4.5 mm × 4.5 mm silicon chips as shown in Figure 4.8. Due to the thermal power dissipated by the current bias, they must be mounted away from the detector array at the $T \approx 4$ K PTC heat sink with greater cooling capacity. To minimize pickup of undesired environmental magnetic fields, the SQUID array chips are mounted directly on top of sheets of niobium, which as a Type II superconductor pins magnetic flux in place to prevent time variation. The SQUID chips are further surrounded by a high permeability metal. Particular care to avoid the use of ferromagnetic metals in nearby hardware is also taken. The low-inductance connector on the left in Figure 4.8(b) provides the interface to the detector array and the standard PCI connector at the top leads to standard twisted pair cryowire and the first room temperature amplifier sensing the SQUID voltage.

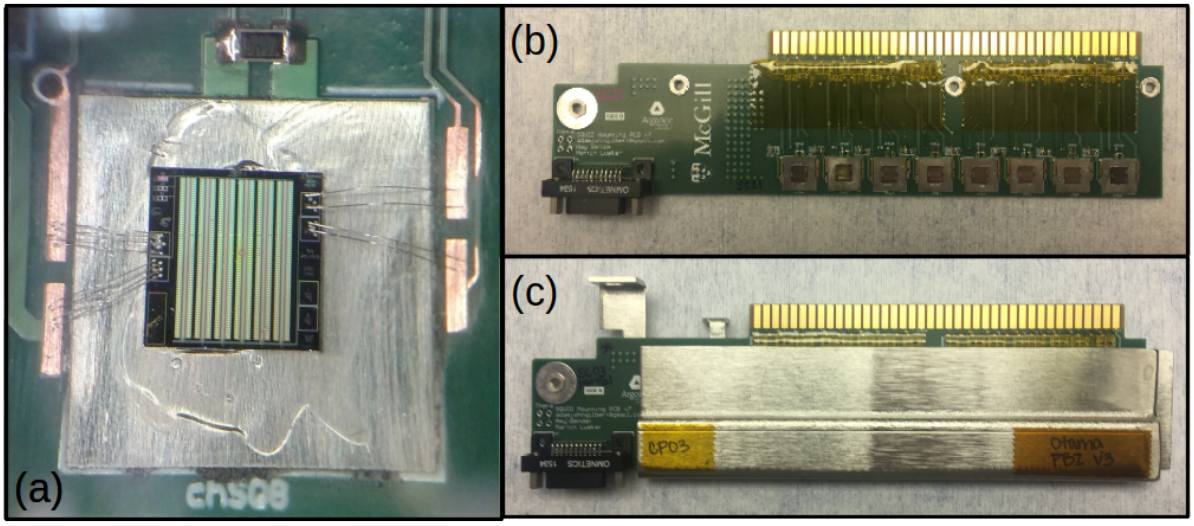

Figure 4.8: Images of Simons Array SQUID array chips and their embedding in the circuit. (a) Individual chips are mounted on thin foils of superconducting Nb to minimize time variation in environmental magnetic fields near the SQUID coils and wirebonded with multiple wires to minimize the inductance of the wirebond connection. (b) 8 chips each are mounted together on a custom printed circuit board which is thermally anchored at $T \approx 4$ K. The SQUID array input coils interface with the detector array via a standard 37-pin micro-D connector - visible in the lower left of the image - and the room temperature electronics interface with the SQUID biasing and readout via a standard PCI connection - visible in the upper right. (c) The SQUID chips collectively are further shielded from external magnetic fields inside a high-permeability metallic sleeve. Images in (b) and (c) courtesy of Lindsay Lowry.

4.4.3 Input inductance

A SQUID array parameter of particular importance to the higher frequency DfMux implementation in use in the Simons Array and SPT-3G is the input inductance L_{in}. For some purposes, the system is insensitive to this parameter - for example, from the point of view of the detector biases a virtual ground is created by the DAN feedback at the node where the nuller current is summed with the TES current, meaning that L_{in} does not modify the resonant frequencies of the multiplexed channels and does not weaken the TES voltage biases by dropping voltage across the SQUID input coil. However, current injected by the nuller will be necessarily split between the path through the SQUID input coil and the path through a RCL multiplexing leg and the bias resistance, as demonstrated in Figure 4.9. If the impedance of the path to ground via the SQUID coil is comparable to its competitor, then the current sharing between the SQUID input and the comb requires the nuller to "work harder" and effectively amplifies any noise sources between the SQUID and the DAN controller input. The quantitative effect of this current sharing is discussed in Section 4.8.

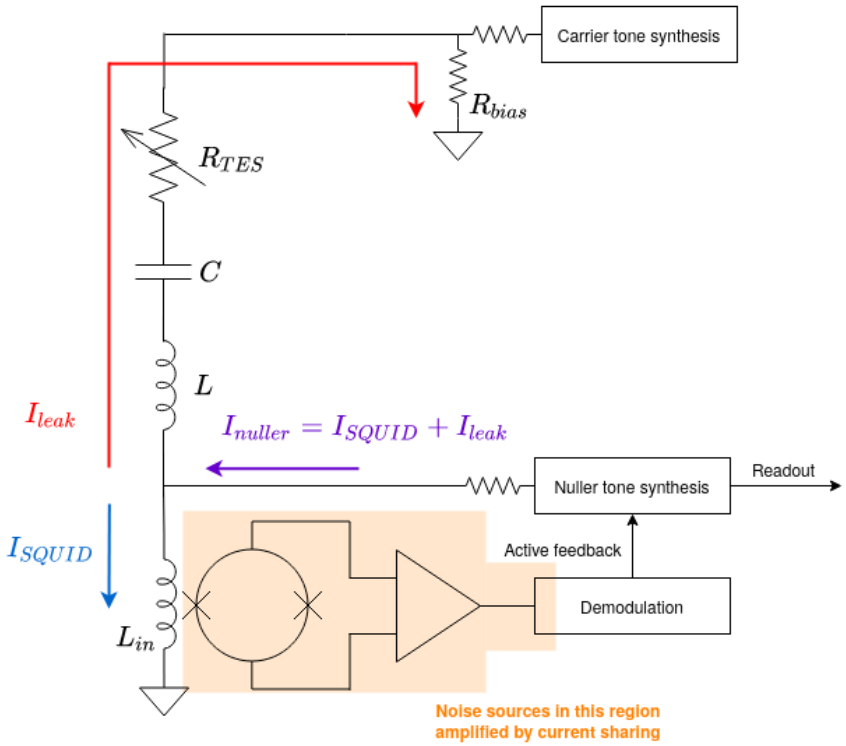

Figure 4.9: Schematic explaining the noise enhancement from current sharing. A single multiplexer channel is shown for simplicity. The on-resonance impedance of the path taken by I_{SQUID} is $i\omega L_{in}$, while the competing path taken by I_{leak} has impedance $i\omega L + (i\omega C)^{-1} + R_{TES} + R_{bias} \simeq R_{TES}$.

The inductance L_{in} may be conveniently measured *in situ* with minimal reliance on circuit modeling. By sweeping a fixed carrier voltage across a range of frequencies, the measured SQUID output voltage is dependent on the sum of the comb impedance and the SQUID input impedance. Separately, by similarly sweeping a fixed nuller current, the measured SQUID output voltage is dependent on the relative ratio of the comb and SQUID input impedances. Specifically, in a carrier sweep around a single channel with resonator inductance L and capacitance C, the measured SQUID voltage is

$$V_{SQUID}^{carrier\ sweep} = Z_{trans} I_{SQUID} \tag{4.17}$$

$$= Z_{trans} \frac{I_{carrier} R_{bias}}{R_{TES} + i\omega(L + L_{in}) + \frac{1}{i\omega C}} \tag{4.18}$$

which notably has minima at the modified frequencies $\omega_i = ((L + L_{in})C)^{-1/2}$. Similarly, for a nuller sweep,

$$V_{SQUID}^{nuller\ sweep} = Z_{trans} I_{SQUID} \tag{4.19}$$

$$= Z_{trans} I_{nuller} \frac{R_{TES} + R_{bias} + i\omega L + \frac{1}{i\omega C}}{R_{TES} + R_{bias} + i\omega(L + L_{in}) + \frac{1}{i\omega C}}. \tag{4.20}$$

Noting that $R_{TES} + R_{bias} \approx R_{TES}$, the ratio of (4.20) and (4.18) may be used to measure the frequency-dependent impedance of the multiplexing circuit

$$\frac{V_{SQUID}^{nuller\ sweep}}{V_{SQUID}^{carrier\ sweep}} \approx \frac{I_{nuller}}{I_{carrier} R_{bias}} \left(R_{TES} + i\omega L + \frac{1}{i\omega C} \right) \tag{4.21}$$

as I_{nuller}, $I_{carrier}$, and R_{bias} are easily known from the circuit design. This ratio mimics the effect of the DAN feedback, cancelling out the impedance of the SQUID input coil. Indeed, the measurement method of (4.21) is used to identify the realized resonance frequencies of the cold circuit and was used to generate the measurements shown in Figures 4.3 and 4.5(a).

By comparing the minima frequencies ω_{ratio} in (4.21) to the minima frequencies $\omega_{carrier}$ in (4.18), one may solve for L_{in} with the only requirement being a foreknowledge of the value of L:

$$L_{in} = L \frac{\omega_{ratio}^2 - \omega_{carrier}^2}{\omega_{carrier}^2} \tag{4.22}$$

The difference between ω_{ratio} and $\omega_{carrier}$ due to a nonzero L_{in} is shown in Figure 4.10 for a Simons Array SQUID. Technically, any inductance between the node at which the nuller adds to the TES current will contribute to the phenomena of current sharing, so L_{in} as measured here and as relevant for noise contains a small amount of inductance due to circuit board trace routing and wirebonds.

At the time of design, the noise impact of a nonzero L_{in} was not appreciated, and the readout system was built with SQUID arrays having $L_{in} \approx 200$ nH.[5] Upon system

[5]In the previous DfMux implementation in POLARBEAR and SPTpol, the SQUID input inductance resulted in a ≈5x smaller impedance due to the ≈5x lower carrier frequencies in use.

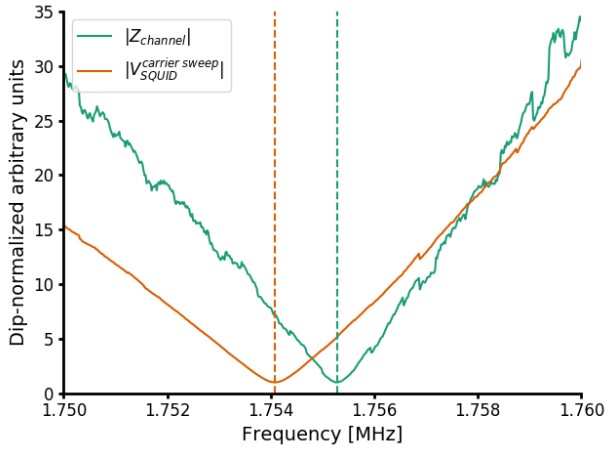

Figure 4.10: Demonstration of measuring the summing node inductance by comparing the peaks in the carrier and "nulled" network analyses with a Simons Array SQUID mounted on a PCB with additional trace inductance. The implied inductance nulled by the operation of DAN feedback is 82 nH in this case.

integration, it was realized that a SQUID design with a smaller L_{in} was needed for acceptable noise performance, and an alternative SQUID array (the NIST SA13a design) was identified to replace the original (the NIST SA4b design). The replacement, while greatly improving the noise performance of the readout system, created two important complications - increased frequency-dependent attenuation of the SQUID voltage due to a larger dynamic resistance and reduced dynamic range due to the smaller input inductance - discussed presently in Sections 4.4.4 and 4.4.5.

4.4.4 Dynamic impedance

The output impedance, or dynamic impedance, of a SQUID array is defined as

$$Z_{out} \equiv \frac{dV}{dI_{cb}}. \tag{4.23}$$

The coupling of the SQUID voltage to its amplifying electronics may be simply modeled with the SQUID as an ideal voltage source in series with Z_{out}, as diagrammed in Figure 4.11(a). The wiring connecting the SQUID coil to the first room temperature amplifier is constructed from twisted pair manganin wire, which contributes ∼20 Ω series resistance and ∼50 pF parallel capacitance across the SQUID voltage leads. A non-negligible output impedance, then, forms an effective low-pass filter which attenuates high frequency voltages before the first amplifier. Using the simple model in Figure 4.11(a), this attenuation is

$$\frac{V_{amplifier}}{V_{SQUID}} = \frac{1}{1 + i\omega C_{wiring}(Z_{out} + R_{wiring})} \tag{4.24}$$

which, as can be seen in Figure 4.11(b), attenuates by a factor of 2 across the 1–5 MHz readout band for a typical 750 Ω output impedance from a NIST SA13b device. Such attenuation effectively reduces the SQUID array gain at high frequencies, modifying the input-referred noise of post-SQUID noise sources. This effect is quantitatively discussed in Section 4.8.

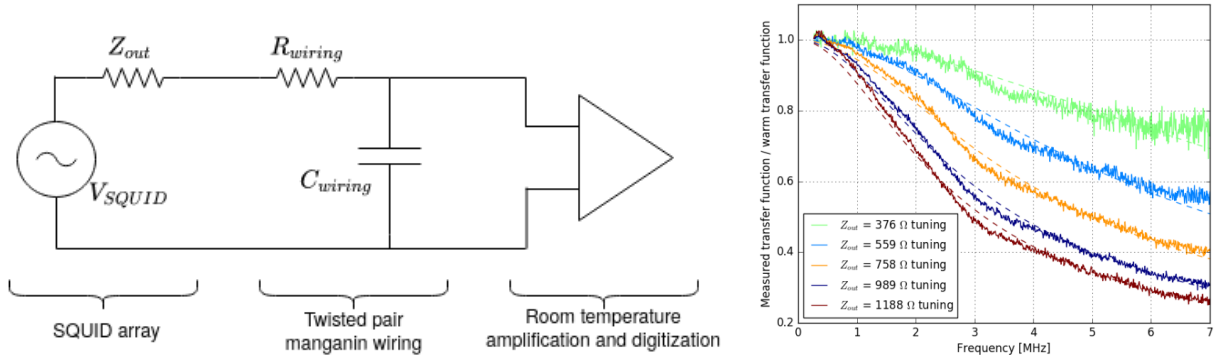

(a) (b)

Figure 4.11: The SQUID output filter formed by the SQUID array output impedance and parasitic wiring capacitances. A simple model of the relevant circuit components is shown in (a), and a demonstration of the effect is shown in (b) by modulating the output impedance of a single SQUID array via retuning.

4.4.5 Dynamic range

As the DAN feedback only nulls the SQUID array input in ∼1 kHz windows at the 40 carrier frequencies, much of the SQUID bandwidth (which, for similar devices, extends past 100 MHz [89]) is effectively operated open-loop. If the total loading on the SQUID array is significant, it can degrade the device dynamic range and gain while increasing noise and nonlinearity [88]. One must endeavor in a DAN-based system, then, to keep the SQUID input sufficiently quiet over a large frequency range. In the current system, this is primarily achieved through passive filtering and radio frequency (RF) shielding, and was verified to enable sufficient SQUID array gain with the original high-L_{in} devices. Upon changing to low-L_{in} SQUID arrays, however, it became apparent that the input impedance of the previous SQUIDs had been acting as an additional layer of protection against very high frequency loading on the nuller line by shunting it to ground via the TES and LC resonator circuit path. A significant degradation of the new SQUID device properties, dependent on the amplitude of the carrier tones, was observed as exemplified by the red curve in Figure 4.12(a). The source of this loading was determined to be Nyquist images of the bias tones produced during their digital generation, as demonstrated in Figure 4.12(b). The addition of additional low-pass filtering

in the room temperature electronics as detailed in Figure 4.12(c), resulted in additional protection of the new SQUID devices, evidenced by the blue and dotted black curves in Figure 4.12(a).

4.4.6 Single-ended readout

Finally, it is worth noting that the schematic in Figure 4.2(b) includes an oversimplification of the SQUID readout circuit. To maximize the dynamic range of the first room temperature amplifier following the SQUID, its inverting input is held at a fixed[6] voltage to offset the DC voltage across the SQUID coil. As such, the SQUID readout is single-ended, creating a mechanism through which environmental noise may couple directly to the SQUIDs. This effect has not been modeled in detail, but empirically it was found that providing a clean circuit ground for the SQUID arrays resulted in improved noise performance. A considerable effort has been spent optimizing the ground configuration, which at ∼MHz frequencies requires more attention than the ∼100 kHz frequencies of the POLARBEAR and SPTpol readout systems.

4.5 Cryogenic cabling

The cable run from the multiplexing summing point on the LC boards at $T \approx 0.3$ K to the SQUID array amplifiers at $T \approx 4$ K is perhaps the most crucial within the readout system. Since the SQUIDs are mounted spatially apart from the detectors, this cable run necessarily long - 60 cm in the Simons Array. To meet crosstalk and detector stability requirements, it must be superconducting and low inductance [90]. Furthermore, as discussed in detail in Chapter 3, the refrigeration system provides only modest cooling power at temperatures below the PTC base; the heat leak through these cables must be sufficiently low to maintain reasonable cryogenic performance.

To satisfy these dual requirements, a custom cable solution was developed. The cables consist of pairs of NbTi planar conductors separated from each other and also sheathed by a polyimid layer. Two conductor pairs are fabricated together in a cable to connect to the double-sided LC boards, as pictured in Figure 4.13. To achieve the desired cable lengths, the conductor strips must be fabricated from bulk NbTi rolled into a thin foil which is subsequently patterned by chemical etching. Connectorization is achieved via an ultrasonic soldering process, which is needed to simultaneously break the strong native oxide layer on the NbTi. Further details of the fabrication and assembly of the NbTi cabling are given in [91].

As discussed in Chapter 3, the NbTi cables contribute the dominant thermal load on the millikelvin refrigeration system, but maintain sufficient performance for operation schedules repeating at integer multiples of a sidereal day. Electrically, the NbTi cables contribute 1.5 nF of parallel capacitance and 21 nH of series inductance to the cryogenic circuit [91].

[6]That is, adjusted during SQUID tuning and held constant thereafter

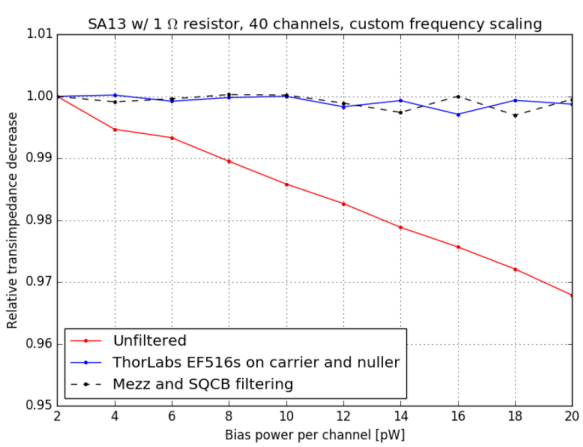

(a)

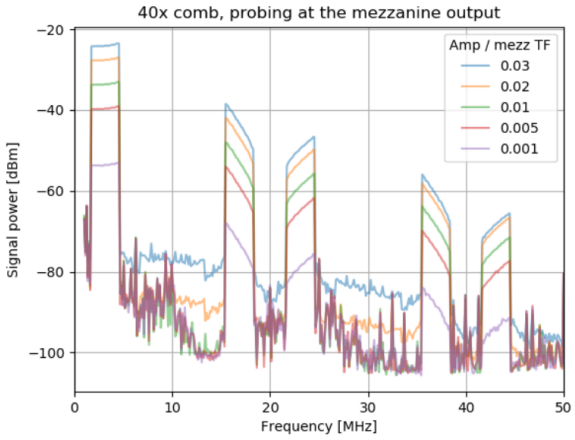

(b)

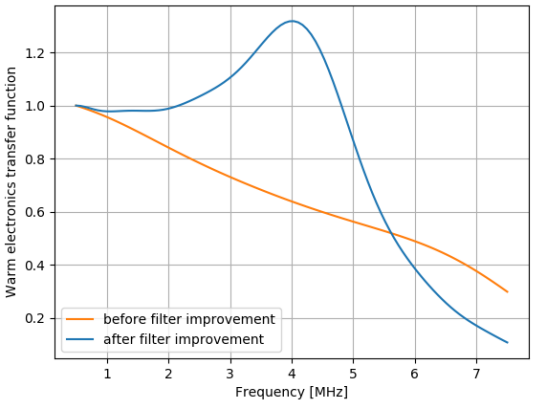

(c)

Figure 4.12: The effect of out-of-band loading on the SQUID arrays and its resolution. (a) shows, in red, the observed phenomenon of low-frequency transimpedance degradation without additional filtering of the bias and nulling combs, which worsens as a function of the bias amplitude. The blue and dashed black measurements demonstrate how additional filtering between the digital tone generation and SQUID array is sufficient to protect the SQUID from this degradation. The out-of-band power from Nyquist images of the bias and nulling combs is shown in (b), as measured at the output of the Iceboard over a range of feasible bias amplitudes. 40 tones are present, but are not resolved by the VNA utilized for the measurement; the comb of tones appears as a "table" in Fourier space here. The original and final filter transfer functions of the warm electronics are shown in (c): additional poles were added that significantly attenuate Nyquist images at higher frequencies.

Figure 4.13: Picture of a Simons Array NbTi readout cryocable used to connect the SQUID array amplifiers at $T \approx 4$ K to the detectors and LC resonators at $T \approx 0.3$ K. The pairs of NbTi traces are visible through the polyimide insulation and also directly through the exposed connectorization windows at either end. Image courtesy of Masaya Hasegawa.

4.6 Detector operation

To operate TES bolometers stably without oscillations, the electrical bandwidth of the readout must exceed the detector thermal bandwidth by a factor of 5.8 [57]. The Simons Array detector thermal time constants are set by the requirement that the time variation of the half-wave plate be sufficiently measured; this sets a soft requirement that τ_{det} be less than 5–10 ms. By choosing $L = 60$ μH for the channelizing inductors, the electrical time constant for a 0.8 Ω TES is $\tau_{elec} = 2L/R_{TES} = 0.15$ ms, providing a comfortable margin of acceptable thermal time constants in the 1–10 ms range.

The sample rate for demodulated detector time-ordered data is set by the desired angular resolution of the instrument. In order to Nyquist sample $\theta_{science}$ ∼1 arcminute scales on the sky with a v_{scan} ∼1 °/s telescope scan speed, one requires

$$f_{sample} \geq 2f_{Nyquist} \gtrsim \frac{v_{scan}}{\theta_{science}} = 120 \text{ Hz}. \tag{4.25}$$

The actual sample rate implemented is $f_{sample} = 152.59$ Hz, corresponding to a 10 MHz clock divided by 2^{16}. The realized sample rate has an important ramification for detector biasing: in order to avoid intermodulation distortion (IMD) products of the 40 bias tones resulting from from nonlinearities in the readout system, all bias frequencies are enforced to be integer multiples of $f_{Nyquist}$. This has the net result that any IMD products will show up as lines just outside the demodulated audio band of each detector after an anti-aliasing filter has been applied. This quantization is very easily achievable without deleterious effects on biasing, since the readout bandwidth is significantly larger than the quantization scale:

$$\Delta f_{readout} = \frac{1}{2\pi\tau_{elec}} = \frac{R}{2\pi L} \gg f_{Nyquist}. \tag{4.26}$$

Several procedural steps are required to prepare detectors for CMB observations. First, as the realized LC resonance frequencies have an intrinsic scatter due to fabrication realities and cryogenic circuit parasitic impedances, they must be measured in-situ using the carrier and nuller sweeps described in Section 4.4.[7] The bias carrier frequencies are then set to the

[7]Because of the temperature dependence of the kinetic inductance of the LC resonators, it is important that the resonance frequencies are measured at the fridge base temperature where they will be operated.

measured resonance locations, rounded to the nearest multiple of $f_{Nyquist}$. In order to bias the TESs into the middle of their superconducting transitions, they must first be heated by raising the detector wafer temperature above the TES critical temperature.[8] At this point, the carrier and nuller for each channel are enabled with a large amplitude $P_{elec} > P_{bath}$ sufficient to ensure the detectors will remain in a normal state when the detector wafer is subsequently cooled back to the fridge base temperature. The procedure of applying electrical power to ensure $T_{TES} > Tc$ is called *overbiasing*.

After the fridge cools, the detectors are tuned in parallel by iteratively reducing V_{bias} until a target fractional resistance $R_{frac} \equiv R_{TES}/R_N$ is achieved. Initially, the detectors are in the Ohmic regime, where $I_{TES} = V_{bias}/R_N$, visible at high bias voltage (and equivalently high bias power) in the measurements shown in Figure 4.14. Eventually, each detector will reach the so-called "turnaround" point, where $\frac{dI}{dV} = 0$, before entering the constant power regime where $I_{TES} = P_{bath}/V_{bias}$.

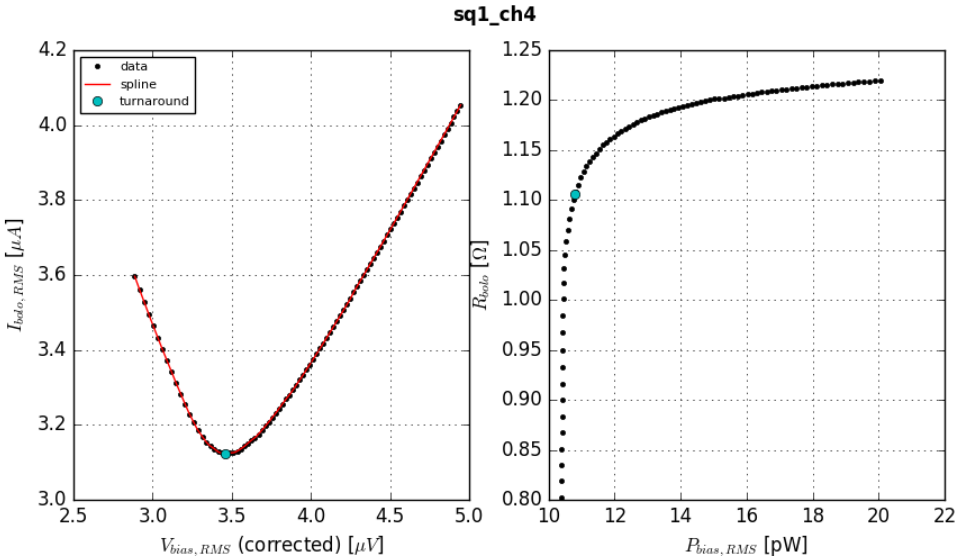

Figure 4.14: Current-voltage and resistance-power relations for a Simons Array TES bolometer

The target tuning point for each detector is practically a trade-off between realizable detector parameters and stability. As discussed in Chapter 3, as the detectors are lowered further into their transitions, their loop gains increase, their thermal time constants decrease, and their responsivities increase. However, if a detector is biased too deep such that its resistance becomes comparable to the equivalent series resistance (ESR) at its channel frequency,

[8]Only when the TES films are at least partially in their normal states may they dissipate Joule power. This operation may be performed during the regular fridge recycling procedure or separately with a distinct fridge operation.

the voltage bias becomes spoiled, the electro-thermal feedback weakens, and oscillations may ensue which irretrievably "latch" the TES into its superconducting state.[9]

A measurement of the ESR for a typical readout module from the original aluminum-based fabrication run and another from subsequent niobium-based fabrication runs. Particularly notable is the large variation in the aluminum-based devices; this is due to the fact that the inductor and capacitor ordering was reversed for half the resonators in each module. The parasitic capacitance of the interdigitated capacitors to the ground plane of their mounting PCB manifests differently in the RCL-ordered and RLC-ordered devices, with the RLC-ordered devices having a larger equivalent Thevenin resistance [92]. This wiring order was fixed for subsequent builds and is independent of the resonator material choice. Additionally, however, the resonator boards with niobium-based devices display an overall larger ESR after the RLC/RCL effect is taken into account. The latter effect has not yet been well studied. The net result of the variance in ESR across resonator builds, however, is that the initial commissioning observations with POLARBEAR-2a were forced to contend with a greater variability in ESR and thus a greater variability in available detector bias parameters than after its 2020/2021 refurbishment.

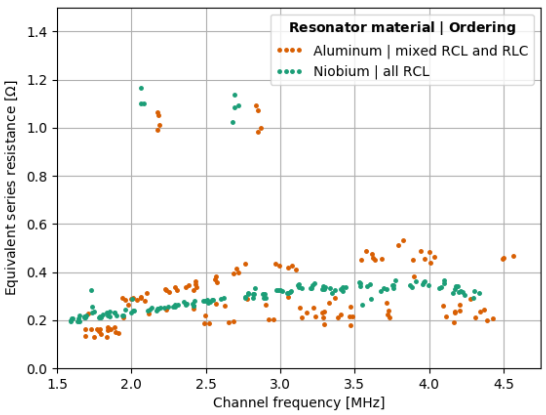

Figure 4.15: Comparison of equivalent series resistance for 4 Al combs in PB2a and 4 Nb combs in PB2a, showing the effect of both the material choice and inductor-capactor ordering. The 1 Ω channels at approximately 2.2 and 2.7 MHz are calibration resistors; their ESR is comparable to their neighbors' values.

The relationship between the magnitude of ESR and detector bias parameter space is demonstrated for detectors read out with resonators from the original build in Figure 4.16. In the left panel, the latching resistance - the resistance below which a further reduction in bias voltage causes an oscillation which traps the TES into its superconducting state - is shown to be correlated with the ESR. In particular, it is impossible to bias a detector to

[9] at least until the next time the detector wafer can be heated above the detector T_c

$R_{TES} < \alpha R_{par}$ where α is at least 1 and as high as 3 for some channels. The right panel shows that the region of conceivable sensitivity between the turnaround (where $dI/dV = 0$ so that $\mathscr{L} = 1$) and where the detector latches is constrained in many cases to as little as 20% of the resistance range of the entire superconducting transition. With the switch to new resonators in POLARBEAR-2a in the 2020/2021 cryogenic refurbishment discussed in Chapter 5, a notable increase in bias flexibility will be gained due to the reduced ESR.

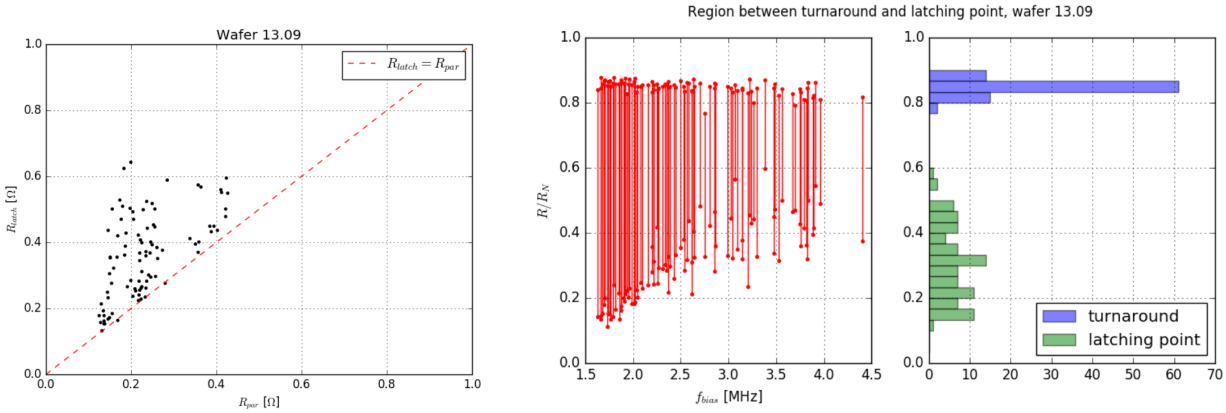

(a) (b)

Figure 4.16: Effect of series impedance in the cold circuit on the detector bias parameter space. (a) shows the latching resistance R_{latch} correlated with the series impedance R_{par}, demonstrating the fundamental limit that the parasitic impedance places: TES resistances below R_{par} are not operable. (b) demonstrates how the distribution of series impedances affects the usable fractions of the TES transitions. In the left panel, a vertical line is drawn connecting the turnaround point - where the detector transitions from the Ohmic regime to the constant-power regime - and the latching point, both plotted as a fraction of the normal resistance R_N. The larger parasitics at higher channel frequencies, due in this measurement primarily to the RLC-ordered resonators from the original aluminum build, limit the usable region of the transition for detector operation.

4.7 Crosstalk

Crosstalk between simultaneously observing detectors can form an important systematic for CMB measurements. In particular, it can lead to spurious B-modes in the measured polarization maps, confusing inflation searches (see, e.g., [93] for a more detailed treatment). If crosstalk is sufficiently large as to merit direct mitigation, it can in principle be characterized and significantly reduced with offline analysis methods [94]. Multiple mechanisms may contribute to the overall crosstalk in an instrument, of which intra-multiplexer electrical

crosstalk is one.[10,11] The Simons Array readout design targets <1% crosstalk globally across all channels [90].

Three mechanisms for crosstalk between channels in a DfMux module are physically motivated:

1. Crosstalk due to inductor cross-coupling: the mutual inductance between nearby inductors on the LC chip can couple current changes from one resonator into the other. Thiis type of crosstalk is easily engineered to be negligible due to measured low mutual inductances and purposeful layout of the resonators on the chip [83].
2. Crosstalk due to bias carrier leakage: due to the parallel combination of 40 RCL resonators, the bias tone intended for one TES realistically deposits a nonzero amount of Joule power on every other TES. Modulation of a neighboring TES's resistance by sky power then will be misidentified by the demodulator as due to the originally targeted TES. Because the off-resonance impedance of each channel is a sharp function of $(f - f_{bias})$, this type of crosstalk is only significant between neighboring channels in frequency space. This crosstalk is fundamentally a *leakage current crosstalk*.
3. Crosstalk due to parasitic series impedance: the impedance (primarily of the NbTi cabling) between the $T \approx 4$ K bias resistor and SQUID input coil and the $T \approx 0.3$ K parallel RCL network realistically develops a small voltage across it, so that the TES bias voltages are smaller than the voltage across the bias resistor. Modulation of one TES's resistance affects the relative ratio of voltage across the parasitic wiring and the RCL network at its carrier frequency, which due to the overlapping nature of the channel impedances in frequency space affects the currents in frequency-adjacent TESs. This crosstalk is fundamentally a *leakage power crosstalk*.

The fractional crosstalk due to bias carrier leakage from a perpetrator channel indexed by n at frequency f into a victim channel indexed by $m = n \pm 1$ of equal resistance R_{TES} at frequency $f \pm \Delta f$ may be approximated as [69]

$$\left|\frac{\delta I_m(f)}{\delta I_n(f)}\right| \approx \frac{R_{TES}^2}{(4\pi L \Delta f)^2} \tag{4.27}$$

and that due to parasitic wiring impedance, in the realistic case that it is dominated by an inductance L_{par} as [69]

$$\left|\frac{\delta P_m(f)}{\delta P_n(f)}\right| \approx \left|\frac{2\pi f L_{par}}{R_{TES}}\left(1 + \frac{iR_{TES}}{4\pi \Delta f L}\right)^{-1}\right|. \tag{4.28}$$

Recently, it has been demonstrated from careful studies of crosstalk in the SPT-3G system that including additional complexities in the crosstalk model matches measured values particularly well [92]. In particular, by accounting for the relative phasing of the two forms of

[10] Various optical effects like reflections off optical surfaces and total internal reflection phenomena inside the detector and lenslet silicon wafers are examples of other crosstalk mechanisms.

[11] Inter-multiplexer crosstalk is expected to be negligible in DfMux readout.

crosstalk, by including the effects of parasitic impedance within the parallel LCR network, and by modeling the realistic quantization of bias frequencies to integer multiples of $f_{Nyquist}$, moderate departures from (4.27) and (4.28) in the on-sky data were able to be explained. This level of detailed modeling has not yet been applied to the deployed hardware in the Simons Array as on-sky crosstalk has yet to be measured, so the more simplistic model from [69] is utilized here for a preliminary estimate.

Crosstalk concerns dictate various details of the multiplexer channel placement. Because both crosstalk mechanisms scale as $(\Delta f)^{-1}$, they become negligible for all channel pairs except nearest neighbors. Through a purposeful ordering of the channels within a multiplexer in frequency space, this effect is leveraged to remove the possibility of crosstalk between detectors observing different sky frequencies, which is more problematic for mitigation in offline analysis. This ordering is shown for the POLARBEAR-2a and POLARBEAR-2b systems (though it will be similar for the 220 GHz and 280 GHz detectors in POLARBEAR-2c) in Figure 4.17. Moreover, as crosstalk due to parasitic wiring impedances was expected at the time of design to be the dominant contributor, a logarithmic frequency spacing (i.e. $\frac{f}{\Delta f} = \kappa$ for some constant κ) was chosen to maintain similar crosstalk levels across all channels. The spacing constant κ was chosen to meet the desired <1% readout-induced crosstalk target, with additional margin to account for fabrication scatter in the realized channel frequencies.

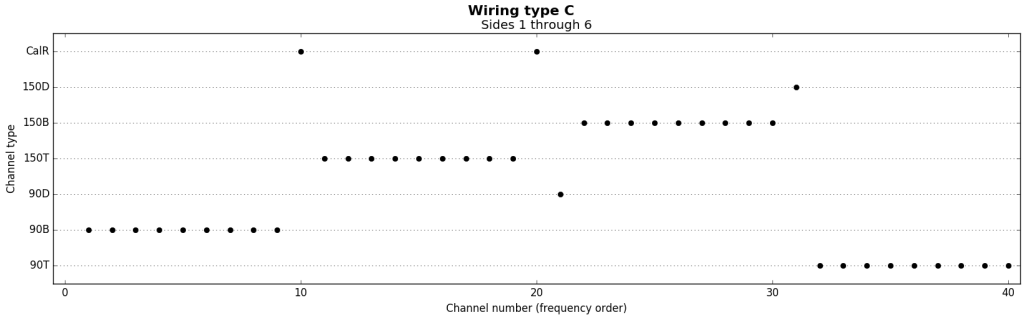

Figure 4.17: The ordering of detector types in frequency space within a multiplexer. Detectors measuring different microwave frequencies on the sky are separated in frequency space so that nearest-neighbor crosstalk is negligible. The placement of dark detectors and calibration resistors further aids this separation.

Estimated readout-induced crosstalk levels for the leakage current and leakage power crosstalk mechanisms are given for a single Simons Array resonator comb in Figure 4.18. As can be seen, there is a safety factor of several between the <1% target and the modeled crosstalk values given the measured resonance frequencies. It should be noted that the two outlier channels at 4.2 MHz are spaced too close to each other due to a chip fabrication error, and most likely only only one of these channels would be biased for real CMB observations.

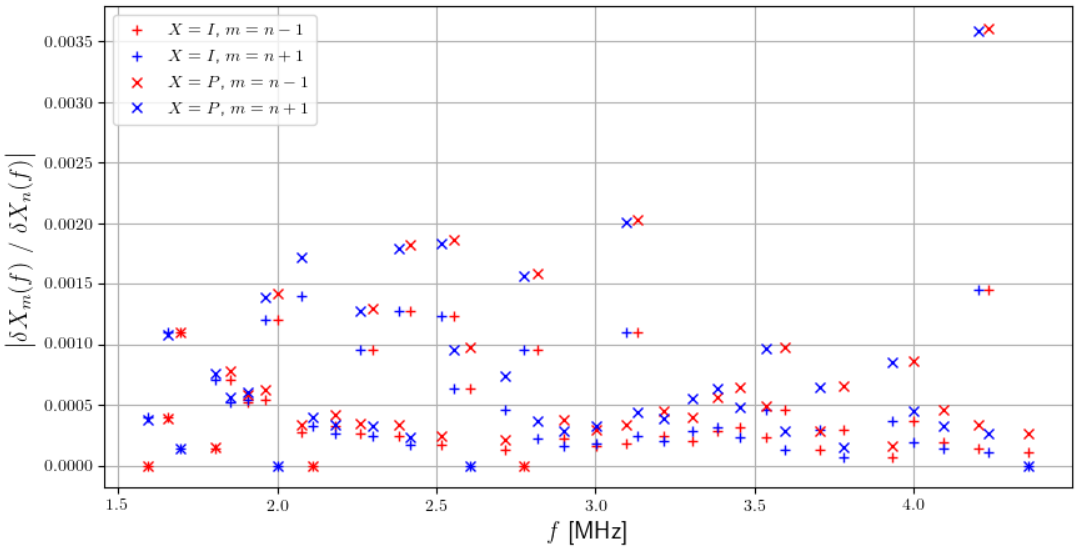

Figure 4.18: Estimated magnitudes of nearest-neighbor (i.e. $m = n \pm 1$) leakage current ($X = I$) and leakage power ($X = P$) crosstalk using the (4.27) and (4.28) for a Simons Array readout module. The plot uses measured frequencies from a multiplexer module in the PB-2a instrument, does not take into account the phase of each crosstalk component, and assumes global values of $R_{bolo} = 0.8R_N$, $R_N = 1.2\ \Omega$, $L = 60\ \mu H$, and $L_{stray} = 45\ nH$.

4.8 System noise

Much of the text in the latter part of this section and Figures 4.21 through 4.24 are excerpts from [95]. ©2021 IEEE

As discussed in Section 3.1.2, noise due to the readout electronics contributes to the overall instrument sensitivity. As such, it merits a careful understanding. In this section, design expectations, as well as modifications to those expectations based on laboratory testing, are presented. Achieved noise distributions from the POLARBEAR-2a detectors are discussed in Chapter 5.

Due to the quadrature demodulation in use, we expect different noise levels in the in-phase (I) and quadrature (Q) timestreams. The demodulation electronics choose the phase that defines the (I,Q) basis after detector tuning by enforcing that $\langle Q(t) \rangle = 0$ so that the carrier and nuller signals are entirely in I. In this basis, I and Q have a simple interpretation as the real and imaginary parts of the detector current. Sky power fluctuations appear preferentially in I, as they are intrinsically aligned with the bolometer responsivities. Reactive parasitics in the cryogenic circuitry are expected to cause the detector signals and power noise sources to be rotated from this default (I,Q) basis by a few degrees. After applying a small offline

rotation to a new (I',Q') basis that undoes this effect, we expect to use the I' time-ordered data for science analysis and discard Q'.

4.8.1 In-phase component

Several types of noise contribute to the overall level of readout noise: Johnson noise in Ohmic components, quantization noise in analog-to-digital converters (ADCs) and digital-to-analog converters (DACs), and noise from complicated circuit elements like SQUIDs and operational amplifiers. To compare the relative magnitudes of these disparate sources, a common reference of equivalent noise current through the TES is used here. From the point of view of this common reference, they various noise contributions may be conceptually divided into 5 or 6 categories:

1. Voltage noise from the components associated with the generation of the carrier tones, which gets referenced to an equivalent noise current via the comb impedance Z_{comb}
2. Johnson-Nyquist noise from the TES resistance itself, which is fundamentally a voltage fluctuation. This is usually grouped separately from "readout" noise as it is due to the detector element itself, but is included here as it cannot be removed from measurements of the readout noise
3. Current noise associated with the generation of the nuller tones and the SQUID flux bias
4. Noise intrinsic to the SQUID array
5. Voltage noise associated with the SQUID current bias and post-SQUID amplification and sensing electronics, which gets referenced to an equivalent noise current via a combination of the SQUID gain and the nuller transfer function
6. Current noise associated with the post-SQUID amplification and sensing electronics (in particular, the input current noise of the room temperature amplifier which follows the SQUID array), which gets referenced to an equivalent noise current via a combination of the SQUID array output impedance, the SQUID array gain, and the nuller transfer function

The parts of the circuit which give rise to each of these noise contributions are highlighted in Figure 4.19, and design values for each are listed in Table 4.2. Details behind these values can be found in [96].

These contributors are Gaussian and uncorrelated, so the total readout (+ TES Johnson)

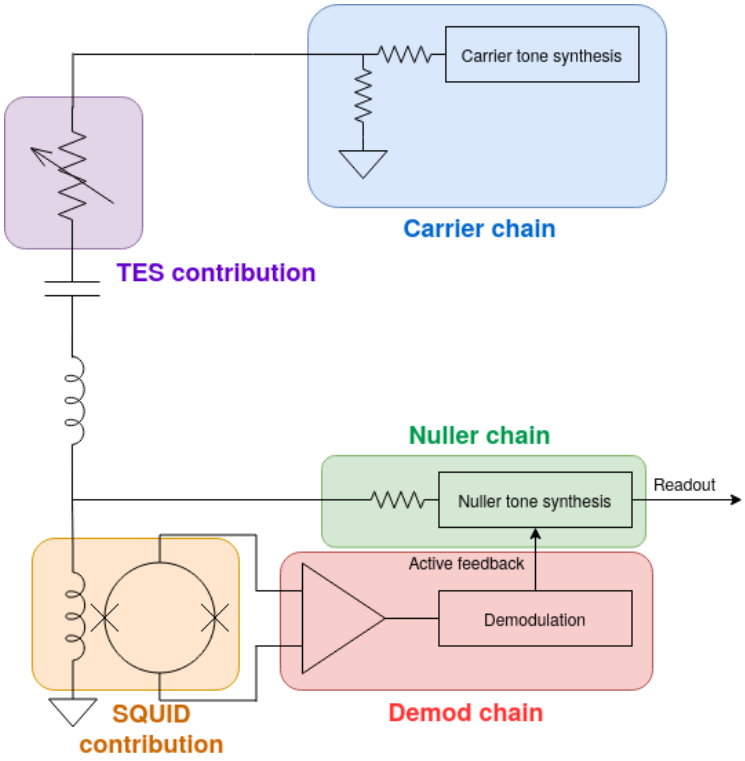

Figure 4.19: Simplified circuit schematic highlighting the various noise contributions in the readout system

Parameter	Value
NEI_{nuller}	5 pA/$\sqrt{\text{Hz}}$
$NEV_{carrier}$	3.2 pV/$\sqrt{\text{Hz}}$
$NEV_{TES\ Johnson}$	4.9 pV/$\sqrt{\text{Hz}}$
NEI_{SQUID}	4 pA/$\sqrt{\text{Hz}}$
NEV_{demod}	3.1 nV/$\sqrt{\text{Hz}}$
NEI_{demod}	3.1 pA/$\sqrt{\text{Hz}}$
$h(\omega = 2\pi \times 2.6\ \text{MHz})$	1.5
$g(\omega = 2\pi \times 2.6\ \text{MHz})$	0.83
$\mathbf{NEI_{total}}$	13.4 pA/$\sqrt{\text{Hz}}$

Table 4.2: Contributions to the expected readout-induced in-phase noise. The entries for h and g are computed using the approximations in (4.32) and (4.33), as well as $L_{in} = 70$ nH, $C_{wiring} = 50$ pF, $R_{TES} = 1\ \Omega$, $Z_{out} = 800\ \Omega$, $R_{wiring} = 20\ \Omega$, and $Z_{trans} = 700\ \Omega$.

noise equivalent TES current is

$$\begin{aligned} NEI_{total}^2 = NEI_{nuller}^2 &+ \left(\frac{NEV_{carrier}}{Z_{comb}}\right)^2 + \left(\frac{NEV_{TES\,Johnson}}{Z_{comb}}\right)^2 \\ &+ (h \times NEI_{SQUID})^2 + \left(\frac{hNEV_{demod}}{gZ_{trans}}\right)^2 \\ &+ \left(\frac{hgZ_{out}NEI_{demod}}{Z_{trans}}\right)^2 \end{aligned} \tag{4.29}$$

where

$$h(\omega) \equiv \left|1 + \frac{Z_{alt}}{Z_{comb}}\right| \tag{4.30}$$

is the current sharing enhancement factor and

$$g(\omega) \equiv \left|\frac{V_{300\,\mathrm{K}}}{V_{\mathrm{SQUID}}}\right| \tag{4.31}$$

is the output attenuation factor, both discussed presently.

The phenomenon of current sharing (discussed earlier in Section 4.4.3) imparts a frequency-dependent weighting to some of the noise contributions listed in Table 4.2. Ideally, DAN would directly measure the SQUID input current $I_{SQUID}(t)$ as its error signal for feedback. In reality, several noise-producing circuit elements lie in between the SQUID input coil and the demod ADC which produce a noise-equivalent current $i_n(t)$ so that the actual error signal used for DAN is of the form $I_{SQUID}(t) + i_n(t)$. Because current sharing causes the nuller transfer function $1/h$ to be significantly less than unity at high frequencies, a nulling current of $h(I_{SQUID}(t) + i_n(t))$ must be applied, multiplying the impact of the demod chain noise by h relative to a hypothetical system with no current sharing. In the simple model where the alternative impedance Z_{alt} which diverts current away from the SQUID is primarily determined by the TES resistance, the current sharing factor becomes

$$h(\omega) \approx \left|1 + \frac{i\omega L_{\mathrm{in}}}{R_{\mathrm{TES}}}\right|. \tag{4.32}$$

Recently, careful analysis of on-sky data with the SPT-3G instrument has demonstrated that a separate current path due to parasitic capacitances to ground in the $T = 0.3$ K circuit adds a further contribution to h [92]. This effect has not yet been studied for the Simons Array hardware, which is expected to have differing levels of parasitic capacitances to ground.

Similarly, the phenomenon of the SQUID array output filtering (discussed earlier in Section 4.4.4) also weights some noise contributions. Voltage noise sources originating from the warm side of the filter are up-weighted by the filter, while current noise sources are down-weighted. Using the simplified circuit model shown in Fig. 4.11, the SQUID output attenuation factor g becomes

$$g(\omega) \approx \left|\frac{1}{1 + i\omega C_{wiring}(R_{wiring} + Z_{out})}\right|. \tag{4.33}$$

Values for h and g are given at the median channel frequency of 2.6 MHz, along with the expected total readout (+ TES Johnson) noise level from (4.29), are given in Table 4.2. An example noise spectra from a laboratory measurement of a 1 Ω calibration resistor is shown in Figure 4.20, demonstrating that noise levels similar to the total given in the final row of Table 4.2 are achievable.

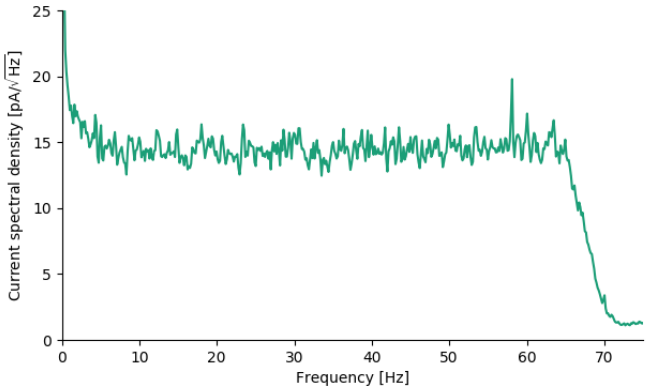

Figure 4.20: Example readout (+ Johnson) noise spectra from a laboratory measurement of a 1 Ω calibration resistor at $T = 250$ mK. The low-frequency noise below 5 Hz is due to thermal drift inside the cryostat and is not intrinsic to the readout. A narrow line is also visible from a parasitic coupling of 60 Hz power into the lab setup.

4.8.2 Quadrature component

Noise sources not dependent on the detector responsivity (e.g. SQUID noise, amplifier noise, resistor Johnson noise) were expected at the time of design to be equal in amplitude between I and Q. A minor exception is the TES Johnson noise, which is preferentially suppressed by the detector loop gain in I but only contributes a negligible fraction of the total noise budget.

However, instead of an equivalence between readout-induced noise in I and Q, we observe a large excess of Q noise. Additionally, this excess increases with the current through the resonator and is coupled with a much smaller current dependence in the I noise level. These effects are demonstrated in Fig. 4.21, in which a resistive channel with zero power-to-current responsivity was "biased" at several current amplitudes. As can be seen in the right part of the figure, there is a small correlation between I and Q, explaining the current dependence of the I noise via a phase shift between the carrier as measured by the room temperature electronics and the phase at which this excess noise is injected.

The current dependence of the Q noise suggests an underlying phase noise. In the DfMux readout system, a jitter in the phase $\phi = \tan^{-1}(Q/I)$ of the channel current corresponds to

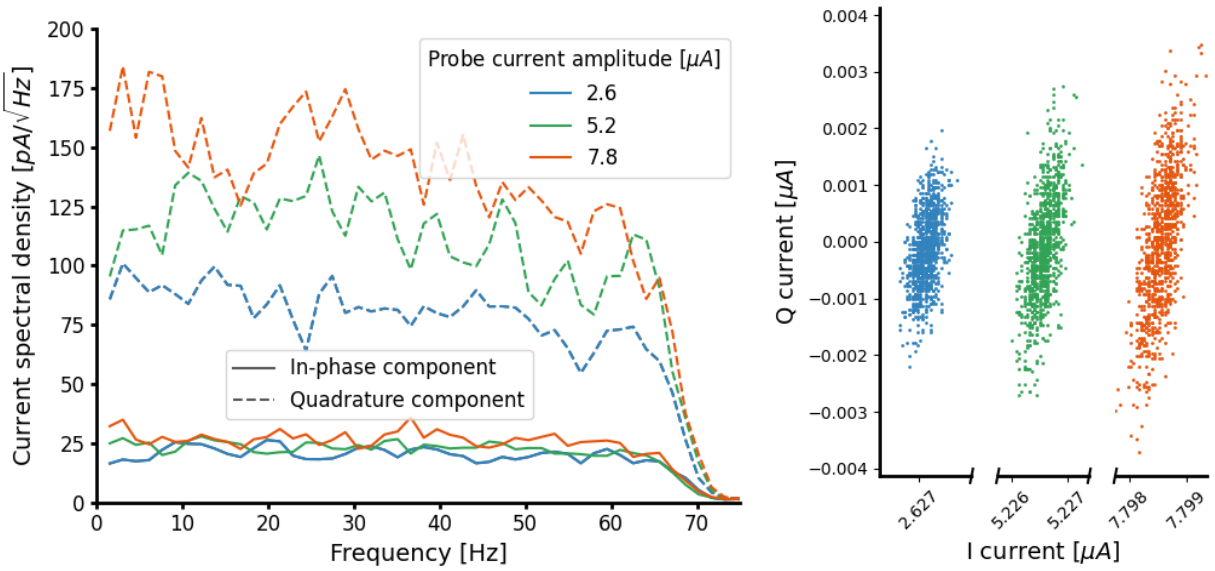

Figure 4.21: *Left:* Spectral densities of the I and Q components of the current through a 3.4 MHz, 1.3 Ω channel at $T = 0.6$ K at several probe currents. The roll off around 70 Hz is due to an anti-aliasing filter in the demodulation electronics. *Right:* Data from three measurements shown on the left, plotted in the I-Q plane. The relatively small probe current dependence in the I noise is evident as simply a consequence of the complex angle of the asymmetric noise, and is removable by a change of basis. The relatively high temperature of 0.6 K enables the use of normal-state TESs for readout characterization, an outlier of which was selected here for visual clarity, but the noise phenomena are qualitatively unchanged at the nominal operating temperature of 0.3 K. ©2021 IEEE

a quadrature noise δQ via

$$\delta Q = \langle I \rangle \tan \delta\phi \tag{4.34}$$

with which we find excellent agreement.[12] However, the observed phase noise is in turn due to a frequency noise, as it is observed to be modulated by the conversion factor between frequency noise and phase noise

$$\frac{\delta\phi}{\delta f} = \frac{d(\arg Z)}{df}\bigg|_{f_r} \tag{4.35}$$

where $f_r = (2\pi\sqrt{LC})^{-1}$ is the natural resonance frequency of the channelizing filter and Z is the complex channel impedance. This is demonstrated in Fig. 4.22, where two channels

[12] As later shown in the right panel of Fig. 4.23, the phase noise $\delta\phi$ itself is a function of $\langle I \rangle$, resulting in a nonlinear dependence of δQ on $\langle I \rangle$.

within the same multiplexer with different sensitivities to frequency jitter can be seen to demonstrate notably different noise asymmetries.

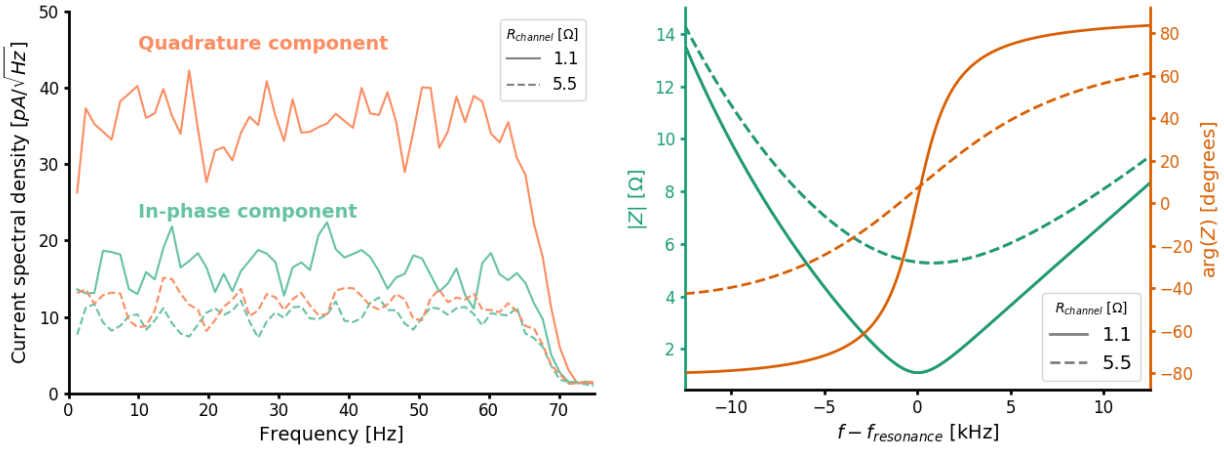

Figure 4.22: *Left:* Noise spectral densities for the currents through two channels at 2.8 and 2.9 MHz with differing resistances within the same multiplexer unit. The measurement was taken at $T = 0.3$ K and with similar probe currents in both channels. The lack of asymmetric noise in the more resistive channel shows that the observed noise is modulated by the resonance width. *Right:* Calculated complex impedances for the two channels measured on the left. The slopes of the orange curves at zero frequency offset determine the conversion from frequency noise to phase noise for each channel and demonstrate that narrower resonances are more sensitive to frequency noise. ©2021 IEEE

The underlying mechanism behind the observed frequency noise appears to be one common to related systems; as reviewed in [84] and [86], superconducting lithographed resonators at ∼GHz frequencies generically host fluctuating two-level tunneling states in amorphous dielectrics which couple to the resonator capacitances and induce resonance frequency jitter. TLS fluctuation noise has a notable set of well-studied dependencies which agree well with our observations.[13] We are currently unaware of any other mechanism capable of simultaneously reproducing all the observed noise phenomena.

Importantly, we observe no phase noise correlation between multiplexer channels, which strongly disfavors mechanisms such as temperature or clock drifts and is consistent with the expectation from TLS fluctuators. Furthermore, TLS noise is known to follow a red spectrum out to the resonator bandwidth where it typically becomes sub-dominant to other noise sources, which we observe as demonstrated in the left panel of Fig. 4.23. A characteristic negative temperature dependence of TLS noise is also reported in the literature,

[13]TLS populations are also known to modify the resonance frequencies and internal quality factors as functions of temperature and readout power, but these were not convenient to measure with our system.

typically following a power law of T^γ where γ varies from -1.2 to -1.7 [86]. Measurements of this dependence in our system were slightly hindered by a lack of direct thermometry and imperfectly constrained thermal gradients as evidenced by the channel-to-channel variation shown in the center panel of Fig. 4.23, but yield broadly consistent fitted power law indices in the -0.6 to -2.5 range. Additionally, the electric field strength in the capacitive part of resonators, or equivalently the average power of the readout tone, is known to suppress TLS noise according to a $P^{-1/2}$ power law. Indeed this is seen in our resonators, as evidenced by the example in the right panel of Fig. 4.23. Finally, TLS population densities are known to be sensitive to fabrication details: material/substrate pairings, residual surface contaminants, oxide layers, etc. In line with this, we observe on average a factor of $\sim$4 larger phase noise in resonators fabricated from aluminum films with an evaporation process over others fabricated from niobium films with a sputter process.

As is visually apparent in the right panel of Fig. 4.21, a simple change of demodulation basis is sufficient to completely remove the excess TLS noise from the data stream. However, we observe a complicating effect, namely that the basis which optimizes TLS noise avoidance is in general distinct from the basis optimizing the detector signal. This phase difference is shown on the left in Fig. 4.24 for an outlier channel where the distinction is visually obvious. Maximizing the detector signal therefore comes with a noise penalty, and vice versa. Practically, then, the basis which optimizes signal-to-noise should be used. Presently, the specific mechanism determining the scale of the non-orthogonality of TLS noise and detector responsivity is unclear, but may be a subject of further study.

In laboratory tests of a spare Simons Array TES wafer where detectors were thermally stimulated with out-of-band optical power from an LED in an otherwise dark cryostat, the rotation angles relating the maximum signal-to-noise basis and the default basis where $\langle Q \rangle = 0$ are typically small: centered around zero with a spread of roughly 10 degrees. To constrain the magnitude of the sensitivity impact on the Simons Array, the signal losses and noise increases relative to a hypothetical system with TLS-free resonators are histogrammed in the right panel of Fig. 4.24, and can be seen to be concentrated at the percent level with a few outliers. As these test conditions under-represent the contribution from photon noise expected during observations, these results should be treated as upper bounds. Therefore, while we expect to perform an offline demodulation basis rotation to maximize sensitivity for the Simons Array, we do not expect TLS noise to appreciably contribute to the overall noise level afterwards.

As DfMux is an amplitude readout scheme, it would be insensitive to TLS noise were it not for the observed non-orthogonality between TLS noise and the detector response. Though the precise mechanism behind the relative angle between signal and noise is unclear, the lack of a fixed relationship is perhaps unsurprising; in other systems susceptible to TLS noise, such as microwave kinetic inductance detectors or microwave SQUID multiplexers, the sensing and readout elements are either co-located in the same structure or coupled via circuitry operating at frequencies significantly below the natural resonance frequency. In our readout system, the RF probe tone and detector bias are coincident, enabling reactive impedances in the wiring between the detector elements and resonators or in the TES itself

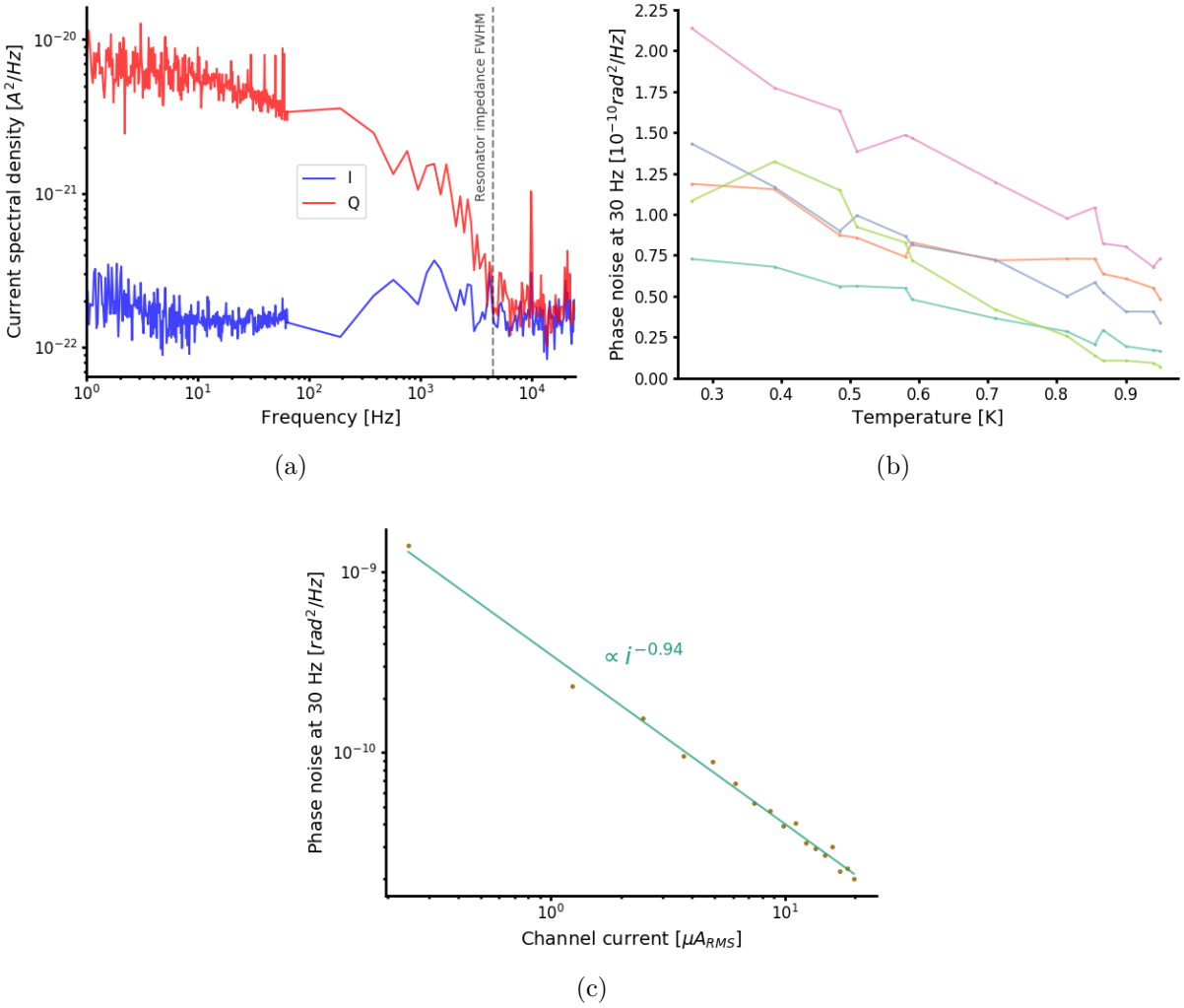

Figure 4.23: (a) spectral density of current through a 2.1 MHz, 1 Ω channel at $T = 0.3$ K over a wider frequency range and with the effect of the anti-aliasing filter removed. The excess asymmetric noise follows a red spectrum out to the resonator bandwidth. (b) temperature dependence of the phase noise measured with a set of 1 Ω channels operated at identical probe currents. Notable channel-to-channel variation is observed, but power law fits yield indices broadly consistent with those reported in the literature for TLS resonator noise. (c) readout current dependence of the phase noise in a 2.1 MHz, 1 Ω channel at $T = 0.3$ K, showing agreement with the $P^{-1/2} = R^{-1/2}I^{-1} \propto I^{-1}$ expectation from TLS fluctuations.

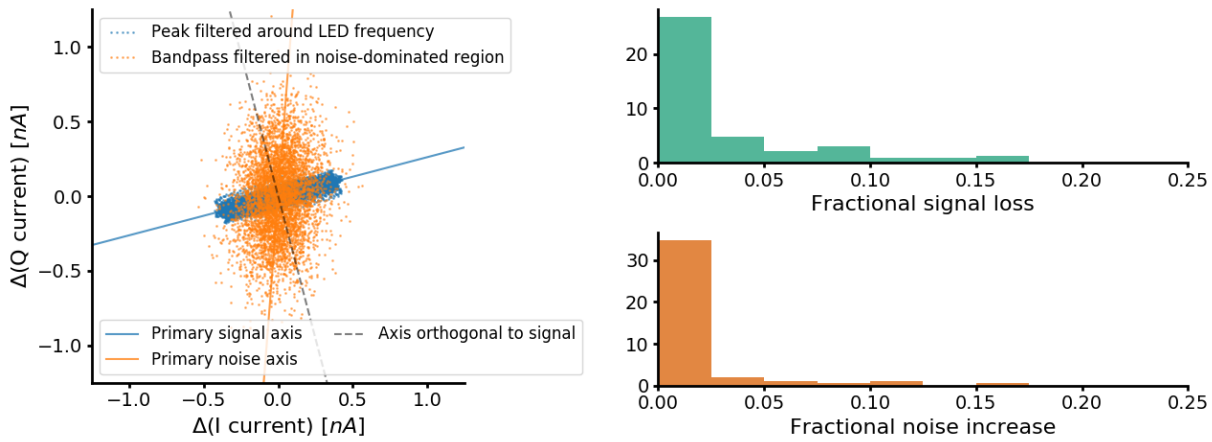

(a) (b)

Figure 4.24: *Left:* The complex current measured in a spare Simons Array detector thermally stimulated at 5 Hz, peak-filtered around the stimulation frequency (blue) and bandpassed in a noise-dominated frequency range (orange). Lines are shown to guide the eye along the principal axis of each data set, showing the non-orthogonality between TLS noise and the detector responsivity. *Right:* Upper bound of the impact of TLS fluctuations on the Simons Array sensitivity by similarly stimulating 91 such detectors. The histograms show the fraction of the maximum possible signal lost and the fractional increase over the minimum possible noise as a result of choosing a demodulation basis that optimizes the signal-to-noise ratio. The relative importance of readout noise in this test is overemphasized due to the lack of photon noise, hence the interpretation of these results as upper bounds. ©2021 IEEE

to produce phase shifts.

For future systems that may wish to adopt TLS noise mitigation strategies, several options are identifiable. At a cost of channel density and/or crosstalk performance, the resonator inductance L may be lowered or the TES operating resistance R_{oper} increased, thereby reducing the conversion factor between frequency noise and phase noise given by Eq. (4.35). For the practical case in which the detector saturation power is held constant, the phase noise will scale with $L/\sqrt{R_{oper}}$ after accounting for the current dependence of TLS noise. Reduction of the TLS fluctuations themselves is also an option; a variety of other techniques, including the use of materials that do not form surface oxides, care to remove residual films in the fabrication process, and modification of the capacitor geometries, have been successfully used in other devices and would be applicable for DfMux readout [84]. Additionally, active feedback on the carrier, similar to that described in [68] or [97], may also provide a further option for avoiding TLS noise. As we are unaware of any report of TLS noise in MHz resonators, at the time of design none of these avoidance or mitigation techniques were

considered;[14] we anticipate that implementation will be straightforward.

[14]For unrelated reasons, R_{oper} is larger by roughly a factor of 2 and a notable fraction of the resonator capacitors were fabricated with wider finger gaps in the SPT-3G implementation relative to the Simons Array implementation [96]. Both of these likely contribute to the relatively smaller level of observed phase noise in SPT-3G.

Chapter 5

Commissioning of the First Simons Array Instrument

At the time of this writing, one of the three Simons Array cryogenic receivers has been integrated with its telescope. This chapter presents select results from the field commissioning of this first instrument, POLARBEAR-2a.

5.1 Overview

After assembly and testing in the laboratory at KEK, the POLARBEAR-2a cryogenic receiver was shipped to Chile in 2018 for installation into its accompanying telescope. The assembly was completed in late 2018, and the first observation of microwave emission from a microwave point source with POLARBEAR-2a occurred in early January, 2019.

During the first cooldown of the receiver after integration with the telescope, an issue with the channelizing resonators in the readout system that had not been present during laboratory testing was observed. The excess loss in the resonators prevented operation of the majority of the detector array, and is described in detail in Section 5.2. Shortly after this new phenomenon was characterized, the cryostat was opened and the resonator issue was resolved by improving a problematic sub-Kelvin cooling path in February 2019.

The subsequent second cooldown of the POLARBEAR-2a receiver was successful; the detector array behaved as expected from laboratory characterization. During this cooldown, many important commissioning tasks were performed: the optical system was focused, the electrical system was characterized, operation strategies were solidified, and many optical properties of the system were measured during this period. The majority of the results presented in Sections 5.4 and 5.5 were from this cooldown. For simplicity, the HWP polarization modulator was not initially installed, so all polarization measurements were instead performed by differencing orthogonal detectors within the same pixel. A separate important focus during this period was on the low-frequency cryogenic stability of the system, which is described in detail in Section 5.3.

Figure 5.1: The first Simons Array telescope in a partially assembled state during early commissioning operations. Image courtesy of Debra Kellner.

Due to infrastructure issues with the diesel power generation for the site, an unintended power outage forced the cryostat to warm to ambient temperature in August 2019. Upon re-cooling, extreme loss in the LC resonators similar to that present in the first cooldown was once again observed. Several subsequent thermal cycles from additional generator failures further increased the additional resonator loss. As a result, only a minority of the detector array was able to be biased and operated. An additional opening of the cryostat to further improve the cooling paths of the resonators was not successful, and the problem was determined not to be fully thermal in origin. Further details are given in Section 5.2.

To resolve the issue with the resonator degradation, an extensive cryogenic refurbishment of the detector array was performed once access to the observing site became possible after the the COVID-19 outbreak. The aluminum-based resonators were replaced with niobium-based devices. Additionally, the original Vespel-based focal plane tower (described in Chapter 3) was replaced with the new carbon fiber design as an attempt to mitigate vibration-induced heating. Several other small repairs, including the replacement of a damaged pulse tube cooler, were also performed during this window of cryostat availability. Once re-cooled in January 2021, the loss in the new resonators was found to be completely nominal (and improved relative to their aluminum counterparts, as explained in Chapter 4).

At the time of this writing, re-commissioning of the POLARBEAR-2a system is underway once again; the detector array is fully operational and the cryogenic system is without significant issues. Furthermore, the HWP polarization modulator has been installed in the optical path and the cryostat enclosure and optical baffling have been nearly finalized. Ad-

ditionally, a new system of redundant power generation at the site has been installed to prevent further unintended outages. As the refurbished POLARBEAR-2a cryogenic receiver in its sixth cooldown has been operating for a relatively short time, a detailed presentation of the post-refurbishment system performance is unfortunately outside the scope of this thesis.

5.2 Excess resonator loss

The time-dependent additional loss in the aluminum resonators have posed a significant obstacle for regular science-quality observations with the POLARBEAR-2a instrument. It has arisen under two seemingly different circumstances - these, along with the eventual resolutions, are described separately in Sections 5.2.1 and 5.2.2.

5.2.1 First occurrence

During the first cooldown of the POLARBEAR-2a cryogenic receiver after installation in Chile, anomalously low resonance frequencies and additional loss was observed in most of the multiplexer resonances, as illustrated in Figure 5.2. In particular, the on-resonance impedance of most channels was greater than the TES impedance, spoiling the ability to voltage bias the detectors with stable electro-thermal feedback. This phenomena of severe resonator loss had not been observed over several years of laboratory testing. The issue was isolated to the LC resonator chips themselves, as the calibration resistor channels were equally affected and as the magnitude of the issue was found to be strongly correlated with the chip fabrication batch details. In particular, 100% of the resonators from the Nb resonator build were unaffected, as well as a minority of batches from the Al resonator build.

Both the resonance frequencies and losses of the affected channels were found to be modulable by temperature, suggestive of a kinetic inductance effect. Independent laboratory tests of nominal aluminum resonator chips were able to reproduce similar phenomena by heating the chips close to their superconducting transition temperature (see Figure 4.5 and the corresponding text in Section 4.3.3). Upon visual inspection of the cryostat interior, it was found that a majority of screws critical to the cooling path of the resonator chips had not been tightened during the assembly of the detector array in Chile. These screws were tightened and a redundant thermal path was added, resulting in a return to approximately nominal parasitic resistance in the affected channels during the second Chilean cooldown as demonstrated in Figure 5.2(b).

5.2.2 Second occurrence

After a thermal cycle of the detector array up to ambient temperature and back in August 2019, a similar resonator problem to that described in Section 5.2.1 was observed, as demonstrated in Figure 5.3. Subsequent thermal cycles of the resonators exacerbated the observed

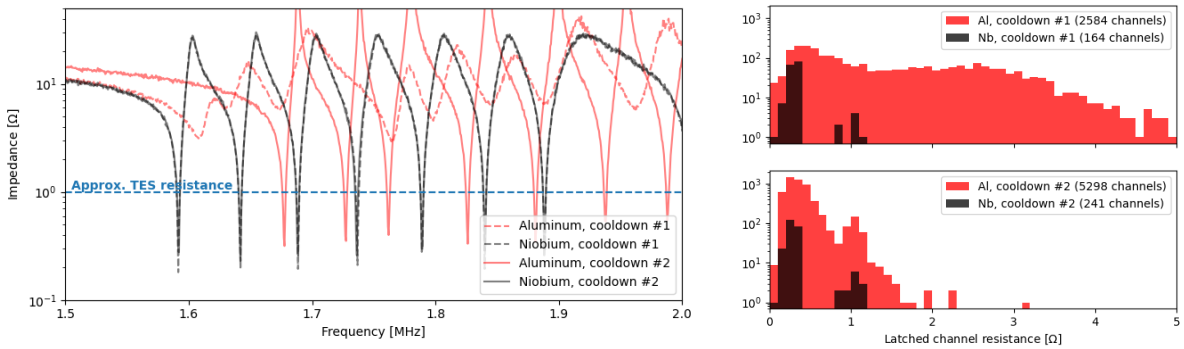

(a) (b)

Figure 5.2: Phenomenology of the first occurrence of the resonator degradation. In (a) the impedance of a typical aluminum module is compared to that of a typical niobium module for both the first problem cooldown and the second cooldown in which the issue was resolved. The aluminum resonances can be seen to have decreased resonance frequencies and significantly increased on-resonance impedance, while the niobium resonances remained unaffected. In (b) the distribution of measured on-resonance impedances with the fridge at base temperature is shown, before (above) and after (below) the cryogenic fix. Many aluminum resonances were so affected that determining their on-resonance frequencies was not feasible, so the upper histogram contains significantly fewer channels and is biased towards the smaller resistances which were possible to measure. The population at 1 Ω is primarily due to the 2 calibration resistors in each multiplexer.

loss and frequency shift. As during the first occurrence of severe resonator loss, the problem was limited to devices from specific fabrication batches of the aluminum resonator build.

From dedicated cryogenic tests and subsequent a physical inspection, it was determined that the affected resonators were properly thermalized with good cooling paths. Additionally, fits to electrical models of the multiplexer impedance confirmed that the impedances of the parallel legs of the RCL network were being modified with each thermal cycle (as opposed to an impedance in series such as from the NbTi cabling). Moreover, the most degraded channels are observed to have a larger temperature sensitivity, as shown in Figure 5.4. From these observations, it is speculated that the zero-temperature kinetic inductance fraction of the aluminum inductors is modified by the cycling to ambient temperature (possibly combined with exposure to the atmosphere instead of their usual vacuum environment) as suggested in [98] and [99].

Because the resonator degradation seemed likely due to a material property and because of the observed immunity of the resonators from the niobium build, an invasive repair was carried out in late 2020 in which all the aluminum resonators were replaced with niobium

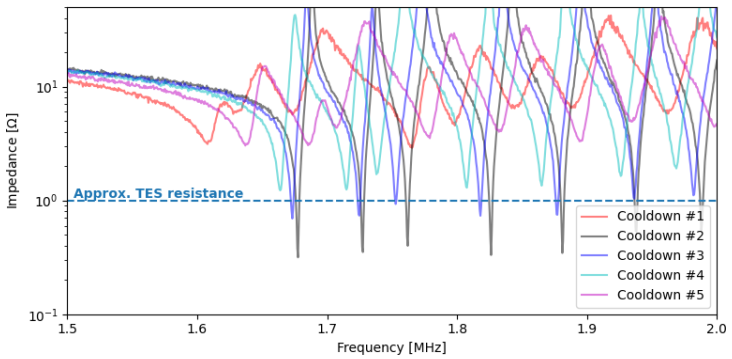

Figure 5.3: Principal observation of the second occurrence of the aluminum resonator degradation. The impedance of the same aluminum module from Figure 5.2 is shown across the 3rd, 4th, and 5th thermal cycles of the cryostat (the first and second are also included for comparison). A worsening with time, approaching the condition of the resonators in the first cooldown, is clearly visible.

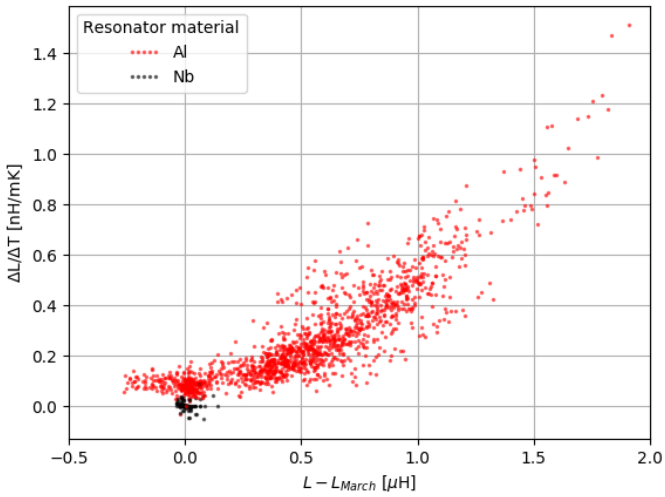

Figure 5.4: Temperature sensitivity of the resonator inductance as a function of the offset from the 2nd cooldown state, under the assumption that the resonator capacitances are unchanging for 1552 example channels. The most degraded aluminum resonators are the most temperature sensitive, consistent with an increased kinetic inductance fraction.

devices. Initial data from the re-cooled system now show nominal resonator properties, consistent with those characterized in the POLARBEAR-2b system [100] which has identical resonator boards.

5.3 Cryogenic stability

As was a concern during the instrument design,[1] vibrational heating of the detector array due to telescope motion was observed after deploying POLARBEAR-2a into the field. The phenomenology of the observed heating is demonstrated in Figure 5.5. In particular, the bath temperature T_{bath} for the detectors is modulated by telescope scanning motions, in turn modulating the detector bias points and gains. Microphonic line pickup is also seen in the detectors coincident with narrow lines seen in the spectra of accelerometers exterior to the cryostat and the encoder of the telescope drive itself, indicating that telescope-induced vibrations have an efficient coupling path to the detectors.

Of the two ways to mitigate this observed vibrational heating - reducing the source of vibrations and reducing the system sensitivity to vibrations - the former is preferable from an engineering standpoint as it does not require invasive cryogenic redesign. As such, a study of the origin of telescope vibrations was carried out. From this study, it was realized that the relatively high (>10 Hz) frequency vibrations of the cryostat are introduced somewhere after the motor drive shaft.[2] This is demonstrated in Figure 5.6, which shows that the rotation of the azimuth motor shaft is quite smooth while the telescope itself responds with several resonant modes above 10 Hz. Unfortunately, due to the design of the motor control system, mitigating these resonances via the motor feedback system is not possible. As demonstrated in Figure 5.7, the bandwidth of the feedback loop which incorporates the telescope encoder is much too slow to damp high-frequency vibrations.

In lieu of a direct mitigation of the telescope vibrations, an avoidance-based strategy is still possible. Due to the strong frequency dependence of the telescope vibrations, one may search the parameter space of scanning motions for those which minimally excite the cryostat interior. From dedicated scan parameter sweeps, it was found that the primary scanning motion which causes heating is the constant-velocity portion of the constant-elevation scans (CESs) which are used to observe the CMB patch. Additionally, the acceleration with which the telescope reverses direction during these scans and the elevation angle at which they are performed do not appreciably affect the net heating of the detector array. The primary result of these tests is shown in Figure 5.8, which demonstrates that by avoiding particular resonant scan speeds and scanning more slowly one may minimize the amount of heating to which the detectors are subjected.

[1] See Chapter 3 for more details

[2] A natural candidate is the azimuth speed reducer, which couples the high-torque, high-speed azimuth motor to the high-torque, low-speed friction bearing and was known to cause issues for the POLARBEAR instrument. The speed reducer is a complicated mechanical device in which imperfections in its manufacture can easily lead to nonlinearities in the relationship between its input shaft speed and output shaft speed.

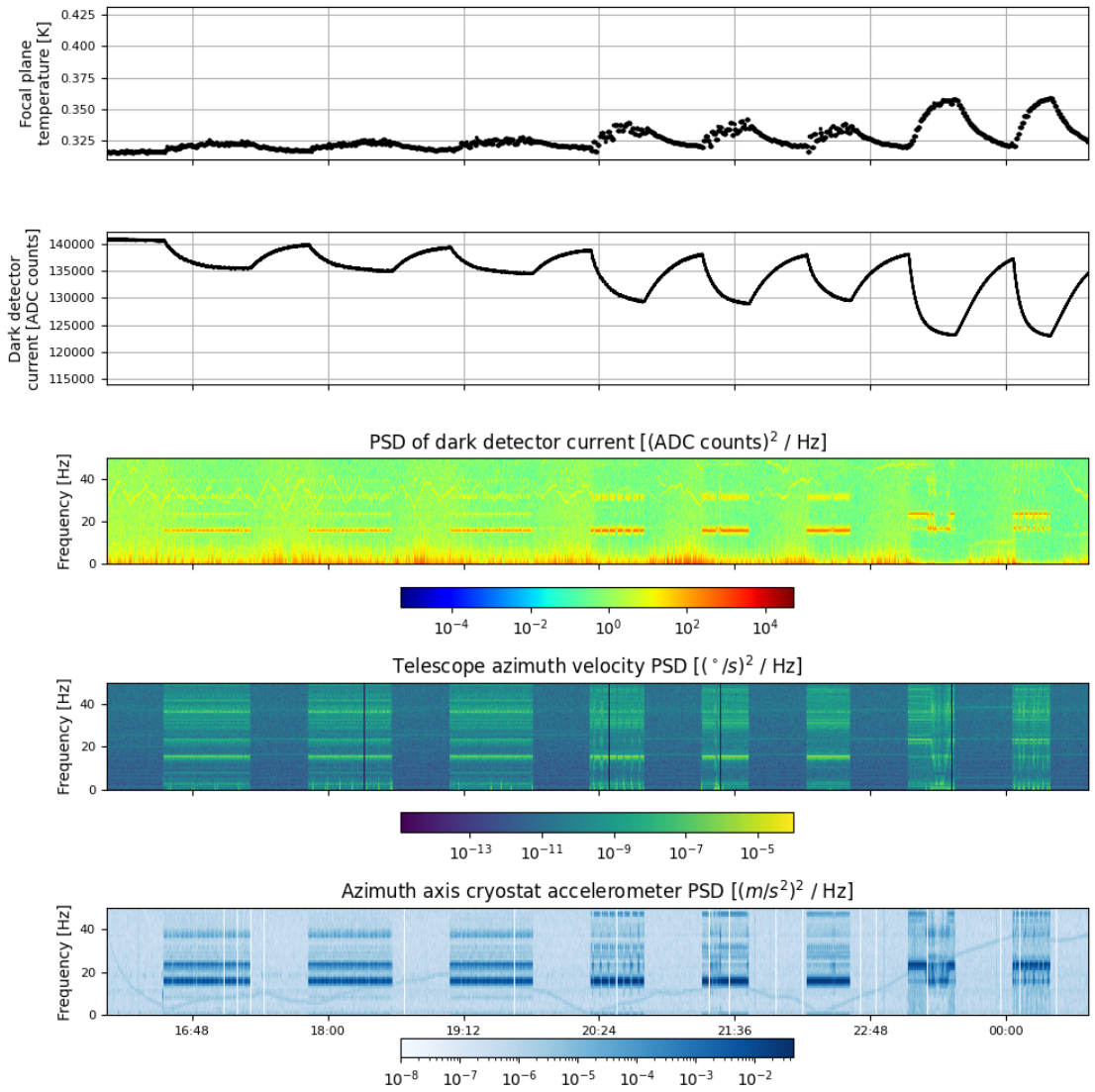

Figure 5.5: Time trends of several quantities during a dedicated scan parameter test which demonstrate many facets of the observed heating. The test was a sequence of constant elevation scans lasting ∼30 minutes each separated by periods where the telescope was stationary. Each "scanlet" modified either the speed of the constant-velocity portion of the scan pattern or the acceleration of the turnaround. The plots show, from top to bottom, (i) the heating of the detector array during periods of telescope motion and its subsequent cooling during stationary periods, (ii) the bias point of a non-optical TES bolometer being modulated by the bath temperature variation, (iii) microphonic pickup in the non-optical detector during scan periods, (iv) resonances in the telescope structure, and (v) narrow-band vibration of the cryogenic receiver.

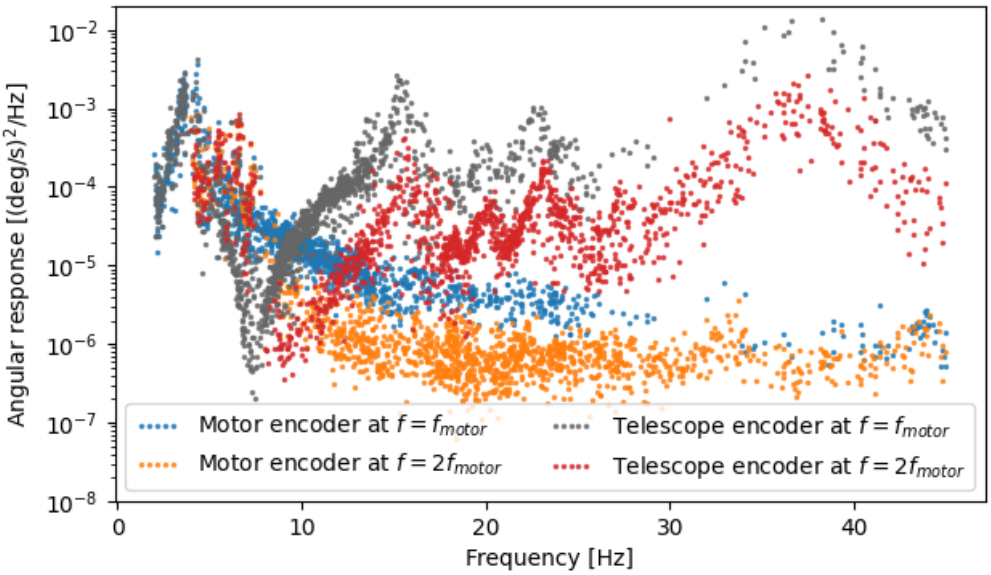

Figure 5.6: Lock-in measurement of the telescope and motor resolver responses at the motor rotation frequency and its first harmonic, for a range of motor rotation speeds. Aside from a resonance at $f \approx 4$ Hz, the motor rotation is observed to be quite smooth; the telescope encoder response indicates resonances not fed back on by the servo system.

Because an opportunity for cryogenic work became available for other reasons, during the retrofitting of the detector array with new channelizing resonators in late 2020, the mechanical support structure for the detector array was also replaced with the one described in detail in Chapter 3. As a result of this recent change, further characterization of the vibrational heating of the system will be required before the scan strategy can be finalized. In general, though, the final strategy will be a trade-off between scanning too slow - in which case 1/f atmospheric fluctuations may more easily contaminate the detector time-ordered data - and scanning too fast - in which case vibrational heating of the detectors leads to low-frequency fluctuations. Other important inputs are the efficacy of the continuously rotating HWP, which is currently undergoing characterization, and the detector gain-temperature coefficients (defined in Equation (3.10)), which have preliminarily been measured to be $\mathcal{O}(-1\ \%/\mathrm{mK})$ but similarly require re-characterization after the resonator replacement. Initial testing of an active temperature regulation scheme utilizing the He-3 fridge also shows promise, and may loosen restrictions on the telescope scan parameters.

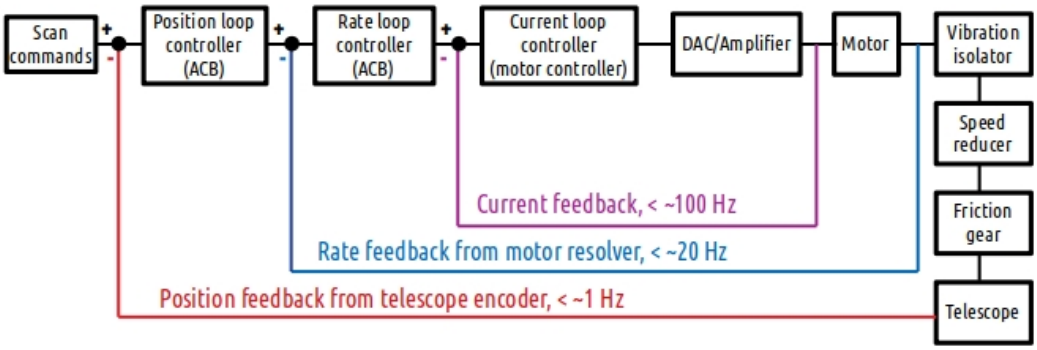

Figure 5.7: Schematic of the telescope drive feedback system. Multiple nested loops, each with reduced bandwidth, are employed, which is typical of servo motor systems. In particular, the bandwidth of the feedback loop which takes the telescope encoder as its input has a very low bandwidth of $\lesssim$1 Hz.

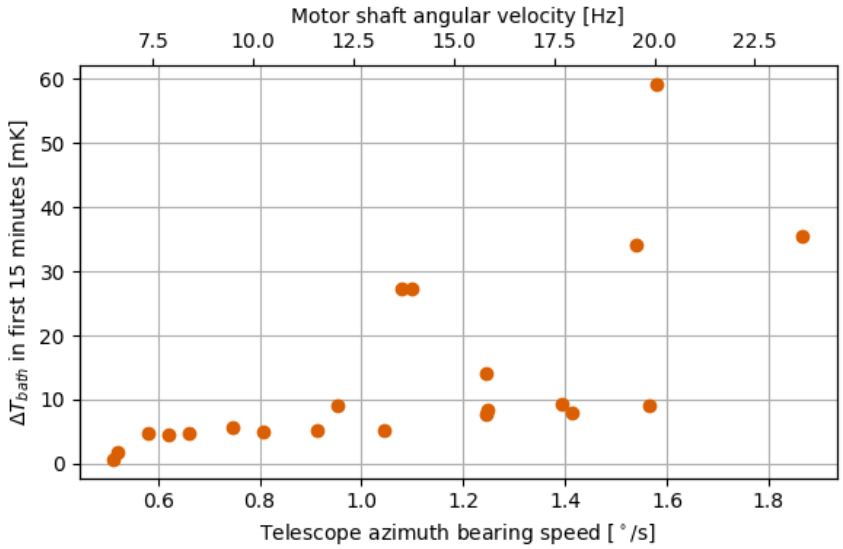

Figure 5.8: Measured detector array heating for constant elevation scans as a function of the azimuth bearing speed.

5.4 Electrical characterization

Though the readout system was vetted in a laboratory setting, it is of course necessary to characterize the fully integrated system under operating conditions. Given the surprises with the resonator loss discussed in Section 5.2, checks of the yield, operability, crosstalk, and noise are warranted. Initial measurements and estimates of all of the above are presented here, though primarily for the system in its 2019 state before the replacement of the aluminum LC resonators.

As the primary motivator for highly multiplexed readout is the large detector count that it enables, the fraction of working readout channels is of great interest. Readout-induced yield losses are categorized into three broad categories in Table 5.1: multiplexer-level losses from SQUID failures, multiplexer-level losses for other reasons, and channel-level losses. The last of these is not a true measurement of readout-only yield, as it is conflated with the yield of connected TESs on the detector, so presents a lower bound. Notably low is the multiplexer-level yield before the 2020/2021 retrofit: this was determined to be due to damaged LC resonator chips resulting from a combination of poor adhesion to their mounting circuit board and differential thermal contraction upon cooling. A deliberate effort was put forward to reduce this yield loss with the retrofitted hardware, which notably improved as can be seen in the table. The individual channel yield for Nb LC resonators is unfortunately lower than for Al LC resonators due to the relative difficulty of the fabrication process and wirebonding.

	Before readout retrofit	**After readout retrofit**
Fraction of SQUID arrays that are operable	>0.99	>0.99
Fraction of multiplexer modules connected to operable SQUID arrays with visible resonant peaks	0.77	0.92
Fraction of channels present on multiplexer modules with at least one channel	0.88	0.74

Table 5.1: Wiring yields in POLARBEAR-2a before and after the 2020/2021 cryogenic refurbishment. While the fraction of working multiplexers improved due to thermal screening of the LC board assemblies, the resonator yield of Nb LC channels is lower. It should be noted that the TES wafer yield is implicitly included in the final row - from the room temperature electrical probing check described in Chapter 3, the fraction of wirebonded, connected TESs in POLARBEAR-2a was measured to be $\leq$94%. Additionally, a small fraction of the flexible cables connecting the LC boards to the wafer were intentionally left unconnected to avoid multi-multiplexer losses due to ground shorts identified late in the assembly process, further lowering the channel yield on the detector side.

Practically, to operate the readout system, two components must be biased - the SQUID array amplifiers and the TES bolometers. For the former, nearly perfect tuning yield was achieved as also indicated in Table 5.1. In order to avoid a self-resonance in the SQUID chips, it should be noted that all the SQUID arrays must be biased on the high dynamic impedance side of the $V(\Phi)$ relation as shown in Figure 5.9(a). This bias restriction was expected from the design but is unfortunate, as it results in a slight noise penalty as discussed in Chapter 4. Distributions of typical tuned SQUID array parameters are shown in Figure 5.9(b) - as can be seen, the dynamic resistance is typically about 100 Ω larger than the transimpedance.

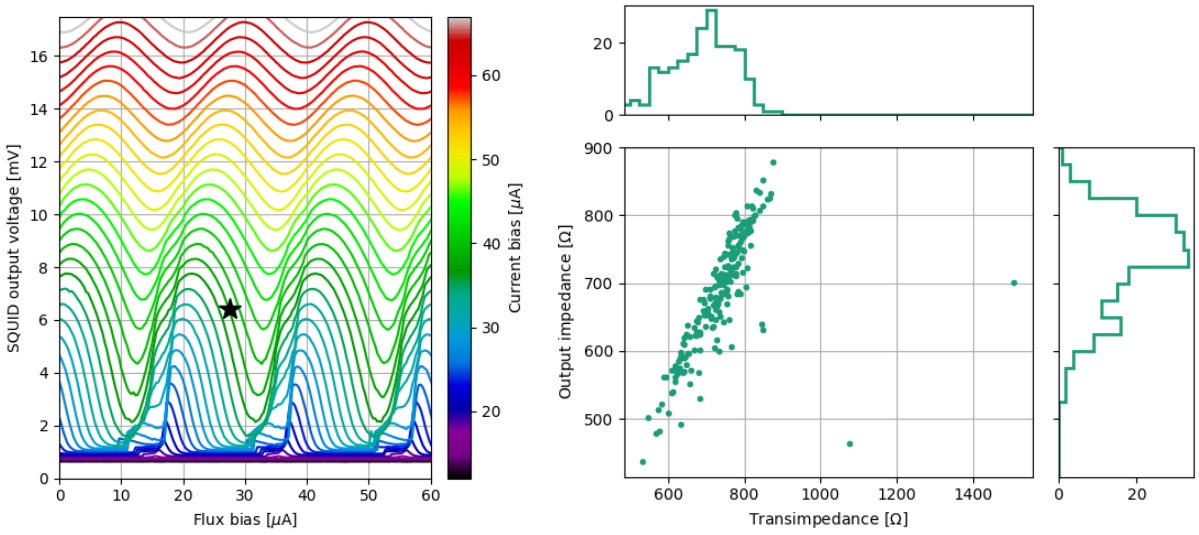

(a) (b)

Figure 5.9: (a) Example SQUID I-V-Φ relationship measured in the POLARBEAR-2a receiver. The bias point chosen by the automated tuning routine is denoted by a back star. The SQUID resonance that must be avoided is visible as the extra "kink" at low current biases on the rising edge of the V-Φ curves. (b) distribution of achieved transimpedance and output impedance parameters after a typical tuning operation.

The tunability of the TES bolometers is somewhat restricted by the individual channel ESRs. Though the overall level of the ESR has decreased recently with the switch to 100% RCL-ordered Nb resonators, the original build of Al resonators contained 50% RLC-ordered resonators resulting in higher ESR as discussed in Chapter 4. The achieved distribution of ESR during the second Chilean cooldown of POLARBEAR-2a is shown in Figure 5.10. Due to some channels latching before they reach their target bias points, along with other quality control cuts including excess noise, the typical tuning yield during observations was 88% during the second cooldown.

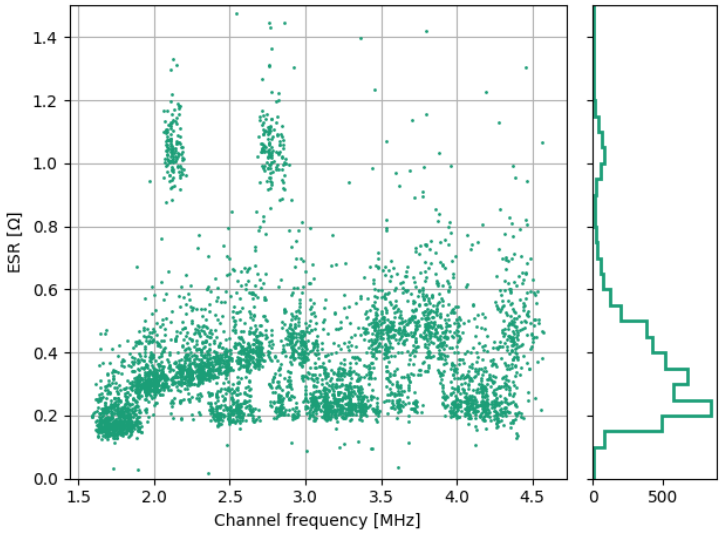

Figure 5.10: Measured ESR in the cryogenic circuit during the second cooldown of POLARBEAR-2a. As explained in Chapter 4, the inductor/capacitor ordering of 50% of the channels resulted in large, frequency-dependent ESR trending up to ≈0.5 Ω at the top edge of the band. Subsequent builds of the resonator chips (including those retrofitted into the cryostat in late 2020) resolved this issue. The two "islands" at 1 Ω around 2.1 MHz and 2.7 MHz are the on-board calibration resistors.

To measure the total on-sky crosstalk in a multi-pixel CMB instrument, typically maps of microwave point sources are fit to a generic crosstalk template.[3] This analysis has not yet been done with POLARBEAR-2a observations, but the model from equations (4.27) and (4.28) may be used for an initial estimate as it depends on only a few circuit parameters which are easily measured. Figure 5.11 shows the distribution of modeled nearest-neighbor crosstalk amplitudes from the measured resonances, which is in particular safely below the <1% design goal discussed in Chapter 4 for nearly all channels.

Another key requirement on the readout system is that it not significantly degrade the sensitivity of the instrument. While the analysis of the additional noise terms to which the readout noise must be compared is still underway, the achieved readout noise-equivalent current is unlikely to dominate the sensitivity given the expected photon and detector noise contributions outlined in Chapter 3. The achieved readout noise across a large sample of channels is shown in Figure 5.12. As can be seen, there is a slight trend with bias frequency, but this is somewhat degenerate with an uncertainty in the frequency-dependent transfer function of the system. After applying a change of basis from the native (I, Q) basis of the readout to a new (I', Q') basis which minimizes the contamination of two-level system noise

[3]This measures both electrical and optical crosstalk, but the sum is the more relevant quantity for science analysis anyway.

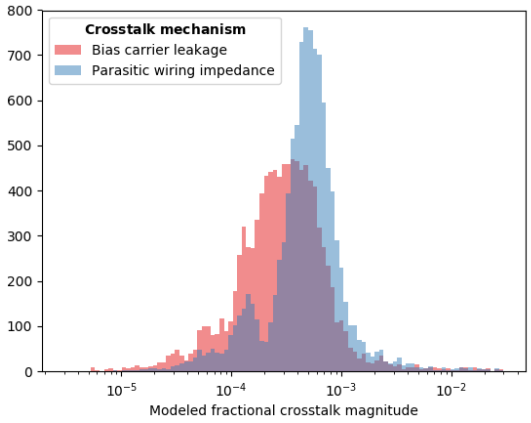

Figure 5.11: Expected electrical crosstalk levels from channels biased during operations in the POLARBEAR-2a receiver as computed via the model from (4.27) and (4.28).

in the science channel I',[4] the noise is negligibly dependent on the bias amplitude and has a median value of 15 pA/$\sqrt{\text{Hz}}$.

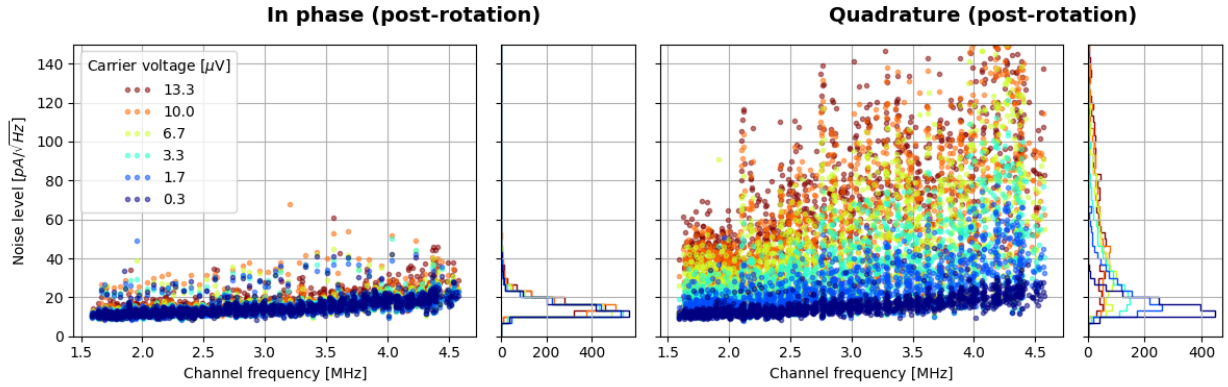

Figure 5.12: Measured noise with the detector array at $T \approx 0.6$ K during the second cooldown of POLARBEAR-2a. After rotating to relegate the excess phase noise to the quadrature component as discussed in Chapter 4, negligible dependence on the carrier voltage remains in the in-phase component. The median in-phase component is 15 pA/$\sqrt{\text{Hz}}$.

[4]See Chapter 4 for a thorough discussion

5.5 Optical characterization

A great deal of characterization must also be done of the optical system in order to certify it as ready for science quality measurements. One typically desires with ground-based CMB telescopes to validate the instrument angular response, polarization response, pixel yield, and overall sensitivity. A brief overview of initial characterization of these aspects is given here, as such work was primarily due to the efforts of others.

The fraction of optically active TESs - defined here as the number of detectors with measured responses to the chopped thermal calibrator over the number of electrically connected detectors - during the 2019 commissioning season was measured to be 87%, and their distribution across the focal plane is shown in Figure 5.13. The angular response of the instrument was iteratively measured with raster scans of solar system planets[5] and used as an input to optimally position the cryostat within the optical system formed by the telescope mirrors. After these operations, the design angular beam FWHM values of 5.2 arcminutes for the 90 GHz beam and 3.5 arcminutes for the 150 GHz beam were met [101]. Preliminary checks of the polarization fidelity of the instrument have been performed with a coherent microwave source temporarily inserted in the optical path, which confirmed the relative angles of the planar antennas across the focal plane [102]. Further verification of the polarization performance was done by reproducing the literature measurement of the polarization angle of Taurus A [103] via a low-sensitivity measurement relying on uncorrected antenna angles alone [101].

It should be noted that until early 2021, for several reasons[6] the HWP polarization modulator was not installed in the optical path. As such, polarization characterization measurements were performed either by differencing orthogonally polarized detectors within the same optical pixel or by temporarily inserting a wire grid into the optical path, and do not necessarily represent the final performance of the system with the HWP. Moreover, without the HWP the telescope baffling could not be fully installed, so far sidelobe angular response also remains to be characterized. Finally, an understanding of the optical efficiency and overall sensitivity remains in progress.

5.6 Future prospects

A great deal of work has collectively gone into the commissioning of the first Simons Array instrument. With the recent reconfigurations and installations, additional commissioning and characterization will be required en route to full science observations. Nevertheless, it is reasonable to expect that POLARBEAR-2a will finalize its hardware configuration and

[5] Jupiter and Venus are most convenient for POLARBEAR-2a in terms of brightness and availability.

[6] The omission of the HWP aided in the simplicity of analysis for initial optical checks, while also giving mechanical freedom for iteratively pistoning the cryostat with respect to the lenses for focusing. Moreover, it allowed for the receiver to be partially open to the environment, which was helpful for human access as various auxiliary systems were continually installed.

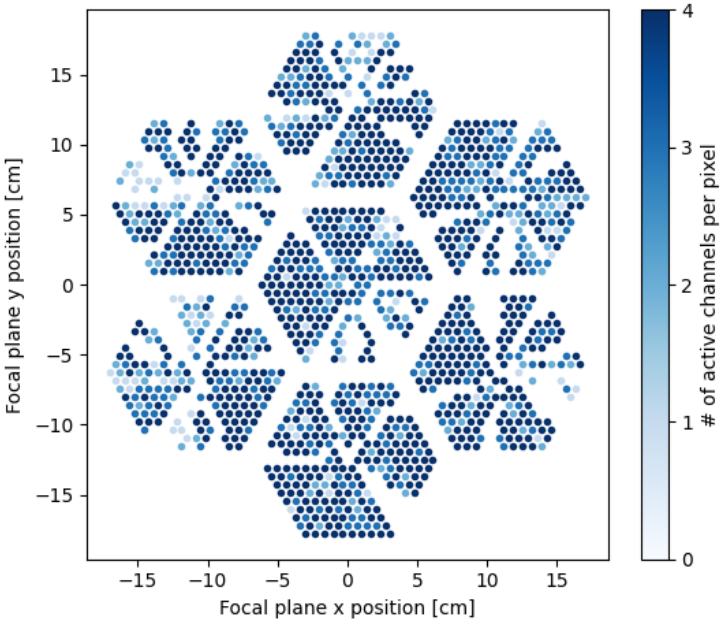

Figure 5.13: Preliminary map of detectors that have measured responses from the chopped thermal calibrator across the focal plane during the second cooldown of POLARBEAR-2a. Broken multiplexer units are visible by eye as missing "wedges" in the hexagonal wafers.

scan parameters in the coming months and begin integrating on the Simons Array cosmology patch. Additionally, the POLARBEAR-2b instrument should see first light this year, subsequently joining POLARBEAR-2a in observations of the cosmology patch. Further afield, POLARBEAR-2c may complete the Simons Array with native dust monitor channels, enabling the full science reach of the experiment.

Bibliography

[1] N. Aghanim et al. "Planck 2018 results". In: *Astronomy & Astrophysics* 641 (Sept. 2020), A6. ISSN: 1432-0746. DOI: 10.1051/0004-6361/201833910.

[2] Planck Collaboration et al. "Planck 2018 results. X. Constraints on inflation". In: *Astronomy and Astrophysics* 641, A10 (Sept. 2020), A10. DOI: 10.1051/0004-6361/201833887. arXiv: 1807.06211 [astro-ph.CO].

[3] Tristram, M. et al. "Planck constraints on the tensor-to-scalar ratio". In: *Astronomy & Astrophysics* 647 (2021), A128. DOI: 10.1051/0004-6361/202039585. URL: https://doi.org/10.1051/0004-6361/202039585.

[4] D. J. Fixsen. "The Temperature of the Cosmic Microwave Background". In: *The Astrophysical Journal* 707.2 (Nov. 2009), pp. 916–920. ISSN: 1538-4357. DOI: 10.1088/0004-637x/707/2/916. URL: http://dx.doi.org/10.1088/0004-637X/707/2/916.

[5] Planck Collaboration et al. "Planck 2018 results. I. Overview and the cosmological legacy of Planck". In: *Astronomy & Astrophysics* 641, A1 (Sept. 2020), A1. DOI: 10.1051/0004-6361/201833880. arXiv: 1807.06205 [astro-ph.CO].

[6] J. M. Nagy et al. "A New Limit on CMB Circular Polarization from SPIDER". In: *The Astrophysical Journal* 844.2 (Aug. 2017), p. 151. ISSN: 1538-4357. DOI: 10.3847/1538-4357/aa7cfd. URL: http://dx.doi.org/10.3847/1538-4357/aa7cfd.

[7] Antony Lewis and Anthony Challinor. *Code for Anisotropies in the Microwave Background*. URL: https://camb.info/.

[8] BICEP2 Collaboration et al. "Constraints on Primordial Gravitational Waves Using Planck, WMAP, and New BICEP2/Keck Observations through the 2015 Season". In: *Physical Review Letters* 121.22, 221301 (Nov. 2018), p. 221301. DOI: 10.1103/PhysRevLett.121.221301. arXiv: 1810.05216 [astro-ph.CO].

[9] Pablo F. de Salas and Sergio Pastor. "Relic neutrino decoupling with flavour oscillations revisited". In: *Journal of Cosmology and Astroparticle Physics* 2016.07 (July 2016), pp. 051–051. ISSN: 1475-7516. DOI: 10.1088/1475-7516/2016/07/051. URL: http://dx.doi.org/10.1088/1475-7516/2016/07/051.

[10] Kevork N. Abazajian et al. "CMB-S4 Science Book, First Edition". In: *arXiv e-prints*, arXiv:1610.02743 (Oct. 2016), arXiv:1610.02743. arXiv: 1610.02743 [astro-ph.CO].

[11] Y. Akrami et al. "Planck 2018 results: XI. Polarized dust foregrounds". In: *Astronomy & Astrophysics* 641 (Sept. 2020), A11. ISSN: 1432-0746. DOI: 10.1051/0004-6361/201832618. URL: http://dx.doi.org/10.1051/0004-6361/201832618.

[12] J. Dunkley et al. "Prospects for polarized foreground removal". In: *AIP Conference Proceedings* (2009). DOI: 10.1063/1.3160888. URL: http://dx.doi.org/10.1063/1.3160888.

[13] Lloyd Knox and Yong-Seon Song. "Limit on the Detectability of the Energy Scale of Inflation". In: *Physical Review Letters* 89.1 (June 2002). ISSN: 1079-7114. DOI: 10.1103/physrevlett.89.011303. URL: http://dx.doi.org/10.1103/PhysRevLett.89.011303.

[14] Uros Seljak and Christopher M. Hirata. "Gravitational lensing as a contaminant of the gravity wave signal in the CMB". In: *Physical Review D* 69.4 (Feb. 2004). ISSN: 1550-2368. DOI: 10.1103/physrevd.69.043005. URL: http://dx.doi.org/10.1103/PhysRevD.69.043005.

[15] Christopher M. Hirata and Uros Seljak. "Reconstruction of lensing from the cosmic microwave background polarization". In: *Physical Review D* 68.8 (Oct. 2003). ISSN: 1089-4918. DOI: 10.1103/physrevd.68.083002. URL: http://dx.doi.org/10.1103/PhysRevD.68.083002.

[16] Kendrick M Smith et al. "Delensing CMB polarization with external datasets". In: *Journal of Cosmology and Astroparticle Physics* 2012.06 (June 2012), pp. 014–014. ISSN: 1475-7516. DOI: 10.1088/1475-7516/2012/06/014. URL: http://dx.doi.org/10.1088/1475-7516/2012/06/014.

[17] BICEP2 Collaboration et al. "BICEP2. II. Experiment and three-year Data Set". In: *The Astrophysical Journal* 792.1, 62 (Sept. 2014), p. 62. DOI: 10.1088/0004-637X/792/1/62. arXiv: 1403.4302 [astro-ph.CO].

[18] R. Gualtieri et al. "SPIDER: CMB Polarimetry from the Edge of Space". In: *Journal of Low Temperature Physics* 193.5-6 (Dec. 2018), pp. 1112–1121. DOI: 10.1007/s10909-018-2078-x. arXiv: 1711.10596 [astro-ph.CO].

[19] Kathleen Harrington et al. "The Cosmology Large Angular Scale Surveyor". In: *Millimeter, Submillimeter, and Far-Infrared Detectors and Instrumentation for Astronomy VIII*. Ed. by Wayne S. Holland and Jonas Zmuidzinas. Vol. 9914. International Society for Optics and Photonics. SPIE, 2016, pp. 380–400. DOI: 10.1117/12.2233125. URL: https://doi.org/10.1117/12.2233125.

[20] S. W. Henderson et al. "Advanced ACTPol Cryogenic Detector Arrays and Readout". In: *Journal of Low Temperature Physics* 184.3-4 (Mar. 2016), pp. 772–779. ISSN: 1573-7357. DOI: 10.1007/s10909-016-1575-z. URL: http://dx.doi.org/10.1007/s10909-016-1575-z.

[21] A. Anderson et al. "SPT-3G: A Multichroic Receiver for the South Pole Telescope". In: *Journal of Low Temperature Physics* 193 (Dec. 2018). DOI: 10.1007/s10909-018-2007-z.

[22] Zigmund D. Kermish et al. "The POLARBEAR experiment". In: *Millimeter, Submillimeter, and Far-Infrared Detectors and Instrumentation for Astronomy VI*. Ed. by Wayne S. Holland. Vol. 8452. International Society for Optics and Photonics. SPIE, 2012, pp. 366–380. DOI: 10.1117/12.926354.

[23] N. Stebor et al. "The Simons Array CMB polarization experiment". In: *Millimeter, Submillimeter, and Far-Infrared Detectors and Instrumentation for Astronomy VIII*. Ed. by Wayne S. Holland and Jonas Zmuidzinas. Vol. 9914. International Society for Optics and Photonics. SPIE, 2016, pp. 363–371. DOI: 10.1117/12.2233103. URL: https://doi.org/10.1117/12.2233103.

[24] Howard Hui et al. "BICEP Array: a multi-frequency degree-scale CMB polarimeter". In: *Millimeter, Submillimeter, and Far-Infrared Detectors and Instrumentation for Astronomy IX*. Ed. by Jonas Zmuidzinas and Jian-Rong Gao. Vol. 10708. Society of Photo-Optical Instrumentation Engineers (SPIE) Conference Series. July 2018, p. 1070807. DOI: 10.1117/12.2311725. arXiv: 1808.00568 [astro-ph.IM].

[25] Maria Salatino et al. "The design of the Ali CMB Polarization Telescope receiver". In: *Millimeter, Submillimeter, and Far-Infrared Detectors and Instrumentation for Astronomy X* (Dec. 2020). Ed. by Jonas Zmuidzinas and Jian-Rong Gao. DOI: 10.1117/12.2560709. URL: http://dx.doi.org/10.1117/12.2560709.

[26] Peter Ade et al. "The Simons Observatory: science goals and forecasts". In: *Journal of Cosmology and Astroparticle Physics* 2019.2, 056 (Feb. 2019), p. 056. DOI: 10.1088/1475-7516/2019/02/056. arXiv: 1808.07445 [astro-ph.CO].

[27] G. J. Stacey et al. "CCAT-Prime: science with an ultra-widefield submillimeter observatory on Cerro Chajnantor". In: *Ground-based and Airborne Telescopes VII*. Ed. by Heather K. Marshall and Jason Spyromilio. Vol. 10700. International Society for Optics and Photonics. SPIE, 2018, pp. 482–501. DOI: 10.1117/12.2314031. URL: https://doi.org/10.1117/12.2314031.

[28] Kevork Abazajian et al. *CMB-S4 Science Case, Reference Design, and Project Plan*. 2019. arXiv: 1907.04473 [astro-ph.IM].

[29] M. Hazumi et al. "LiteBIRD: A Satellite for the Studies of B-Mode Polarization and Inflation from Cosmic Background Radiation Detection". In: *J. Low Temp. Phys.* 194 (Feb. 2019). DOI: 10.1007/s10909-019-02150-5.

[30] BICEP/Keck Collaboration et al. "A demonstration of improved constraints on primordial gravitational waves with delensing". In: *Physical Review D* 103.2, 022004 (Jan. 2021), p. 022004. DOI: 10.1103/PhysRevD.103.022004. arXiv: 2011.08163 [astro-ph.CO].

[31] Duncan J. Watts et al. "A Projected Estimate of the Reionization Optical Depth Using the CLASS Experiment's Sample Variance Limited E-mode Measurement". In: *The Astrophysical Journal* 863.2, 121 (Aug. 2018), p. 121. DOI: 10.3847/1538-4357/aad283. arXiv: 1801.01481 [astro-ph.CO].

[32] Michael Levi et al. "The Dark Energy Spectroscopic Instrument (DESI)". In: *Bulletin of the American Astronomical Society*. Vol. 51. Sept. 2019, p. 57. arXiv: 1907.10688 [astro-ph.IM].

[33] Adrian Liu et al. "Eliminating the optical depth nuisance from the CMB with 21 cm cosmology". In: *Phys. Rev. D* 93 (4 Feb. 2016), p. 043013. DOI: 10.1103/PhysRevD.93.043013. URL: https://link.aps.org/doi/10.1103/PhysRevD.93.043013.

[34] Scott Paine. *The am atmospheric model*. Version 11.0. Sept. 2019. DOI: 10.5281/zenodo.3406496. URL: https://doi.org/10.5281/zenodo.3406496.

[35] Hiroaki Aihara et al. "The Hyper Suprime-Cam SSP Survey: Overview and survey design". In: *Publications of the Astronomical Society of Japan* 70.SP1 (Sept. 2017). S4. ISSN: 0004-6264. DOI: 10.1093/pasj/psx066. eprint: https://academic.oup.com/pasj/article-pdf/70/SP1/S4/23692189/psx066.pdf. URL: https://doi.org/10.1093/pasj/psx066.

[36] Chao-Lin Kuo. "Assessments of Ali, Dome A, and Summit Camp for mm-wave Observations Using MERRA-2 Reanalysis". In: *The Astrophysical Journal* 848.1 (Oct. 2017), p. 64. DOI: 10.3847/1538-4357/aa8b74. URL: https://doi.org/10.3847/1538-4357/aa8b74.

[37] Y. Mizugutch, M. Akagawa, and H. Yokoi. "Offset Dual Reflector Antenna". In: *IEEE International Symposium on Antennas and Propagation Digest*. Jan. 1976, pp. 2–5.

[38] C. Dragone. "Offset multireflector antennas with perfect pattern symmetry and polarization discrimination". In: *AT T Technical Journal* 57 (Sept. 1978), pp. 2663–2684.

[39] Huan Tran et al. "Comparison of the crossed and the Gregorian Mizuguchi-Dragone for wide-field millimeter-wave astronomy". In: *Appl. Opt.* 47.2 (Jan. 2008), pp. 103–109. DOI: 10.1364/AO.47.000103. URL: http://ao.osa.org/abstract.cfm?URI=ao-47-2-103.

[40] Polarbear Collaboration et al. "A Measurement of the Cosmic Microwave Background B-mode Polarization Power Spectrum at Sub-degree Scales with POLARBEAR". In: *The Astrophysical Journal* 794.2, 171 (Oct. 2014), p. 171. DOI: 10.1088/0004-637X/794/2/171. arXiv: 1403.2369 [astro-ph.CO].

[41] Haruki Nishino et al. "Data acquisition and management system for the CMB polarization experiment: Simons Array". In: *Millimeter, Submillimeter, and Far-Infrared Detectors and Instrumentation for Astronomy X*. Ed. by Jonas Zmuidzinas and Jian-Rong Gao. Vol. 11453. International Society for Optics and Photonics. SPIE, 2020, pp. 328–340. DOI: 10.1117/12.2560616. URL: https://doi.org/10.1117/12.2560616.

[42] Y. Inoue. "Development of POLARBEAR-2 receiver system for cosmic microwave background polarization experiment". PhD thesis. Graduate University for Advanced Studies, 2016.

[43] O. Jeong et al. "Broadband Plasma-Sprayed Anti-reflection Coating for Millimeter-Wave Astrophysics Experiments". In: *Journal of Low Temperature Physics* 184 (Aug. 2016), pp. 1–6. DOI: 10.1007/s10909-015-1442-3.

[44] Satoru Takakura et al. "Performance of a continuously rotating half-wave plate on the POLARBEAR telescope". In: *Journal of Cosmology and Astroparticle Physics* 2017.05 (May 2017), pp. 008–008. DOI: 10.1088/1475-7516/2017/05/008. URL: https://doi.org/10.1088/1475-7516/2017/05/008.

[45] S. Adachi et al. "A Measurement of the Degree-scale CMB B-mode Angular Power Spectrum with Polarbear". In: *The Astrophysical Journal* 897.1 (July 2020), p. 55. DOI: 10.3847/1538-4357/ab8f24. URL: https://doi.org/10.3847/1538-4357/ab8f24.

[46] S. Pancharatnam. "Achromatic combinations of birefringent plates". In: *Proceedings of the Indian Academy of Sciences - Section A* 41 (1955), pp. 130–136.

[47] Charles A. Hill et al. "Design and development of an ambient-temperature continuously-rotating achromatic half-wave plate for CMB polarization modulation on the POLARBEAR-2 experiment". In: *Millimeter, Submillimeter, and Far-Infrared Detectors and Instrumentation for Astronomy VIII*. Ed. by Wayne S. Holland and Jonas Zmuidzinas. Vol. 9914. International Society for Optics and Photonics. SPIE, 2016, pp. 699–716. DOI: 10.1117/12.2232280. URL: https://doi.org/10.1117/12.2232280.

[48] C. A. Hill et al. "A cryogenic continuously rotating half-wave plate mechanism for the POLARBEAR-2b cosmic microwave background receiver". In: *Review of Scientific Instruments* 91.12 (2020), p. 124503. DOI: 10.1063/5.0029006. eprint: https://doi.org/10.1063/5.0029006. URL: https://doi.org/10.1063/5.0029006.

[49] J. Choi et al. "Radio-transparent multi-layer insulation for radiowave receivers". In: *Review of Scientific Instruments* 84.11 (Nov. 2013). ISSN: 0034-6748. DOI: 10.1063/1.4827081. URL: https://www.osti.gov/biblio/22251536.

[50] Peter AR Ade et al. "A review of metal mesh filters". In: *Millimeter and Submillimeter Detectors and Instrumentation for Astronomy III*. Vol. 6275. International Society for Optics and Photonics. 2006, 62750U.

[51] P. A. R. Ade et al. "Antenna-coupled TES bolometers used in BICEP2, Keck Array, and SPIDER". In: *The Astrophysical Journal* 812.2 (Oct. 2015), p. 176. DOI: 10.1088/0004-637x/812/2/176. URL: https://doi.org/10.1088/0004-637x/812/2/176.

[52] R. O'Brient. "Log-Periodic Focal-Plane Architecture for Cosmic Microwave Background Polarimetry". PhD thesis. University of California, Berkeley, 2010.

[53] A. Suzuki. "Multichroic Bolometric Detector Architecture for Cosmic Microwave Background Polarimetry Experiments". PhD thesis. University of California, Berkeley, 2013.

[54] P. Siritanasak et al. "The Broadband Anti-reflection Coated Extended Hemispherical Silicon Lenses for Polarbear-2 Experiment". In: *Journal of Low Temperature Physics* 184.3 (Aug. 2016), pp. 553–558. ISSN: 1573-7357. DOI: 10.1007/s10909-015-1386-7. URL: https://doi.org/10.1007/s10909-015-1386-7.

[55] Benjamin Westbrook et al. "The POLARBEAR-2 and Simons Array Focal Plane Fabrication Status". In: *Journal of Low Temperature Physics* 193 (Dec. 2018). DOI: 10.1007/s10909-018-2059-0.

[56] P. L. Richards. "Bolometers for infrared and millimeter waves". In: *Journal of Applied Physics* 76.1 (1994), pp. 1–24. DOI: 10.1063/1.357128. eprint: https://doi.org/10.1063/1.357128. URL: https://doi.org/10.1063/1.357128.

[57] K.D. Irwin and G.C. Hilton. "Transition-Edge Sensors". In: vol. 99. July 2005, pp. 81–97. ISBN: 978-3-540-20113-7. DOI: 10.1007/10933596_3.

[58] T. Elleflot et al. "Effect of Stray Impedance in Frequency-Division Multiplexed Readout of TES Sensors in POLARBEAR-2b". In: *Journal of Low Temperature Physics* 199.3-4 (Mar. 2020), pp. 840–848. DOI: 10.1007/s10909-020-02387-5.

[59] Charles A. Hill et al. "BoloCalc: a sensitivity calculator for the design of Simons Observatory". In: *Millimeter, Submillimeter, and Far-Infrared Detectors and Instrumentation for Astronomy IX* (July 2018). Ed. by Jonas Zmuidzinas and Jian-Rong Gao. DOI: 10.1117/12.2313916. URL: http://dx.doi.org/10.1117/12.2313916.

[60] P. Siritanasak. "Precise Measurement of B-mode polarization signal from the cosmic microwave background with the Polarbear and the Simons Array". PhD thesis. University of California, San Diego, 2018.

[61] A. Cukierman. "Multiscale multichroic focal planes for measurements of the cosmic microwave background". PhD thesis. University of California, Berkeley, 2018.

[62] M.C. Runyan and William Jones. "Thermal conductivity of thermally-isolating polymeric and composite structural support materials between 0.3 and 4K". In: *Cryogenics* 48 (July 2008), pp. 448–454.

[63] N. Kellaris et al. "Sub-Kelvin Thermal Conductivity and Radioactivity of Some Useful Materials in Low Background Cryogenic Experiments". In: *Journal of Low Temperature Physics* 176.3 (Aug. 2014), pp. 201–208. ISSN: 1573-7357. DOI: 10.1007/s10909-013-1048-6. URL: https://doi.org/10.1007/s10909-013-1048-6.

[64] Marco Barucci et al. "Low temperature thermal conductivity of Kapton and Upilex". In: *Cryogenics* 40 (Feb. 2000), pp. 145–147.

[65] J.R. Olson. "Thermal conductivity of some common cryostat materials between 0.05 and 2 K". In: *Cryogenics* 33.7 (1993), pp. 729–731. ISSN: 0011-2275. DOI: https://doi.org/10.1016/0011-2275(93)90027-L. URL: http://www.sciencedirect.com/science/article/pii/001122759390027L.

[66] Amy N. Bender et al. "Digital frequency domain multiplexing readout electronics for the next generation of millimeter telescopes". In: *Millimeter, Submillimeter, and Far-Infrared Detectors and Instrumentation for Astronomy VII* (July 2014). Ed. by Wayne S. Holland and JonasEditors Zmuidzinas. DOI: 10.1117/12.2054949. URL: http://dx.doi.org/10.1117/12.2054949.

[67] K. Bandura et al. "ICE: A Scalable, Low-Cost FPGA-Based Telescope Signal Processing and Networking System". In: *Journal of Astronomical Instrumentation* 05.04 (2016), p. 1641005. DOI: 10.1142/S2251171716410051.

[68] Tijmen Haan, Graeme Smecher, and Matt Dobbs. "Improved Performance of TES Bolometers using Digital Feedback". In: *Proc SPIE* 8452 (Oct. 2012). DOI: 10.1117/12.925658.

[69] M. A. Dobbs et al. "Frequency multiplexed superconducting quantum interference device readout of large bolometer arrays for cosmic microwave background measurements". In: *Review of Scientific Instruments* 83.7 (2012), p. 073113. DOI: 10.1063/1.4737629.

[70] J. W. Henning et al. "Feedhorn-coupled TES polarimeter camera modules at 150 GHz for CMB polarization measurements with SPTpol". In: *Millimeter, Submillimeter, and Far-Infrared Detectors and Instrumentation for Astronomy VI* (Oct. 2012). Ed. by Wayne S.Editor Holland. DOI: 10.1117/12.927172. URL: http://dx.doi.org/10.1117/12.927172.

[71] T. de Haan et al. "Recent Advances in Frequency-Multiplexed TES Readout: Vastly Reduced Parasitics and an Increase in Multiplexing Factor with Sub-Kelvin SQUIDs". In: *Journal of Low Temperature Physics* 199.3-4 (Feb. 2020), pp. 754–761. DOI: 10.1007/s10909-020-02403-8. arXiv: 1908.07642 [astro-ph.IM].

[72] Amy E. Lowitz et al. "Digital frequency multiplexing with sub-Kelvin SQUIDs". In: *Millimeter, Submillimeter, and Far-Infrared Detectors and Instrumentation for Astronomy IX*. Ed. by Jonas Zmuidzinas and Jian-Rong Gao. Vol. 10708. Society of Photo-Optical Instrumentation Engineers (SPIE) Conference Series. July 2018, p. 107081D. DOI: 10.1117/12.2311984. arXiv: 1807.05995 [astro-ph.IM].

[73] A. Tartari et al. "Development and Testing of the FDM Read-Out of the TES Arrays Aboard the LSPE/SWIPE Balloon-Borne Experiment". In: *Journal of Low Temperature Physics* 199 (Apr. 2020). DOI: 10.1007/s10909-020-02431-4.

[74] R. A. Hijmering et al. "Readout of a 176 pixel FDM system for SAFARI TES arrays". In: *Millimeter, Submillimeter, and Far-Infrared Detectors and Instrumentation for Astronomy VIII*. Ed. by Wayne S. Holland and Jonas Zmuidzinas. Vol. 9914. Society of Photo-Optical Instrumentation Engineers (SPIE) Conference Series. July 2016, p. 99141C. DOI: 10.1117/12.2231714.

[75] H. Akamatsu et al. "Progress in the Development of Frequency-Domain Multiplexing for the X-ray Integral Field Unit on Board the Athena Mission". In: *Journal of Low Temperature Physics* 199.3-4 (Jan. 2020), pp. 737–744. DOI: 10.1007/s10909-020-02351-3. arXiv: 2003.11899 [astro-ph.IM].

[76] Shawn W. Henderson et al. "Readout of two-kilopixel transition-edge sensor arrays for Advanced ACTPol". In: *Millimeter, Submillimeter, and Far-Infrared Detectors and Instrumentation for Astronomy VIII*. Ed. by Wayne S. Holland and Jonas Zmuidzinas. Vol. 9914. International Society for Optics and Photonics. SPIE, 2016, pp. 346–362. DOI: 10.1117/12.2233895. URL: https://doi.org/10.1117/12.2233895.

[77] K. M. Morgan et al. "Code-division-multiplexed readout of large arrays of TES microcalorimeters". In: *Applied Physics Letters* 109.11 (2016), p. 112604. DOI: 10.1063/1.4962636. eprint: https://doi.org/10.1063/1.4962636. URL: https://doi.org/10.1063/1.4962636.

[78] B. Dober et al. "A microwave SQUID multiplexer optimized for bolometric applications". In: *Applied Physics Letters* 118.6 (2021), p. 062601. DOI: 10.1063/5.0033416. eprint: https://doi.org/10.1063/5.0033416. URL: https://doi.org/10.1063/5.0033416.

[79] Yaqiong Li et al. "Assembly and Integration Process of the High-Density Detector Array Readout Modules for the Simons Observatory". In: *Journal of Low Temperature Physics* 199.3-4 (Mar. 2020), pp. 985–993. DOI: 10.1007/s10909-020-02386-6.

[80] Mayuri Sathyanarayana Rao et al. "Simons Observatory Microwave SQUID Multiplexing Readout: Cryogenic RF Amplifier and Coaxial Chain Design". In: *Journal of Low Temperature Physics* 199.3-4 (Mar. 2020), pp. 807–816. ISSN: 1573-7357. DOI: 10.1007/s10909-020-02429-y. URL: http://dx.doi.org/10.1007/s10909-020-02429-y.

[81] A. Cukierman et al. "Microwave Multiplexing on the Keck Array". In: *Journal of Low Temperature Physics* 199.3-4 (Dec. 2019), pp. 858–866. ISSN: 1573-7357. DOI: 10.1007/s10909-019-02296-2. URL: http://dx.doi.org/10.1007/s10909-019-02296-2.

[82] C Yu et al. "An impedance-modulated code-division microwave SQUID multiplexer". In: *Engineering Research Express* 2.1 (Jan. 2020), p. 015011. DOI: 10.1088/2631-8695/ab68a4. URL: https://doi.org/10.1088/2631-8695/ab68a4.

[83] K. Rotermund et al. "Planar Lithographed Superconducting LC Resonators for Frequency-Domain Multiplexed Readout Systems". In: *Journal of Low Temperature Physics* 184 (July 2016). DOI: 10.1007/s10909-016-1554-4.

[84] Jonas Zmuidzinas. "Superconducting Microresonators: Physics and Applications". In: *Annual Review of Condensed Matter Physics* 3.1 (2012), pp. 169–214. DOI: 10.1146/annurev-conmatphys-020911-125022.

[85] Michael Tinkham. *Intoduction to Superconductivity: Second Edition*. Dover Publications, 2004.

[86] Clemens Muller, Jared H Cole, and Jurgen Lisenfeld. "Towards understanding two-level-systems in amorphous solids: insights from quantum circuits". In: *Reports on Progress in Physics* 82.12 (Oct. 2019), p. 124501. DOI: 10.1088/1361-6633/ab3a7e.

[87] John Clarke and Alex I. Braginski. *The SQUID Handbook: Fundamentals and Technology of SQUIDs and SQUID Systems*. Vol. 1. Weinheim: Wiley-VCH, 2006.

[88] Maximiliano Silva-Feaver et al. "Comparison of NIST SA13a and SA4b SQUID Array Amplifiers". In: *Journal of Low Temperature Physics* 196 (Aug. 2019). DOI: 10.1007/s10909-018-2083-0.

[89] Martin Huber et al. "DC SQUID series array amplifiers with 120 MHz bandwidth (corrected)". In: *Applied Superconductivity, IEEE Transactions on* 11 (July 2001), pp. 4048–4053. DOI: 10.1109/77.947383.

[90] Y. Akiba et al. "Development of readout electronics for POLARBEAR-2 Cosmic Microwave Background experiment". In: *Journal of Low Temperature Physics* 184 (July 2016). DOI: 10.1007/s10909-015-1448-x.

[91] J. Avva et al. "Design and Assembly of SPT-3G Cold Readout Hardware". In: *Journal of Low Temperature Physics* 193 (Nov. 2018). DOI: 10.1007/s10909-018-1965-5.

[92] J. Montgomery et al. "Performance and characterization of the SPT-3G digital frequency multiplexed readout system using an improved noise and crosstalk model". In: *Millimeter, Submillimeter, and Far-Infrared Detectors and Instrumentation for Astronomy X*. Ed. by Jonas Zmuidzinas and Jian-Rong Gao. Vol. 11453. International Society for Optics and Photonics. SPIE, 2020, pp. 167–188. DOI: 10.1117/12.2561537.

[93] Kevin T. Crowley et al. "Studies of systematic uncertainties for Simons Observatory: detector array effects". In: *Millimeter, Submillimeter, and Far-Infrared Detectors and Instrumentation for Astronomy IX*. Ed. by Jonas Zmuidzinas and Jian-Rong Gao. Vol. 10708. International Society for Optics and Photonics. SPIE, 2018, pp. 658–684. DOI: 10.1117/12.2313414.

[94] J. W. Henning et al. "Measurements of the Temperature and E-mode Polarization of the CMB from 500 Square Degrees of SPTpol Data". In: *The Astrophysical Journal* 852.2 (Jan. 2018), p. 97. DOI: 10.3847/1538-4357/aa9ff4.

[95] J. C. Groh et al. "Anomalous Frequency Noise from the Megahertz Channelizing Resonators in Frequency-Division Multiplexed Transition Edge Sensor Readout". In: *IEEE Transactions on Applied Superconductivity* (2021). DOI: 10.1109/TASC.2021.3065283.

[96] J. Montgomery. "Digital Frequency Domain Multiplexing Readout: Design and Performance of the SPT-3G Instrument and LiteBIRD Satellite Readout". PhD thesis. McGill University, 2020.

[97] J. Kuur et al. "Active Tuning of the Resonance Frequencies of LC Bandpass Filters for Frequency Domain Multiplexed Readout of TES Detector Arrays". In: *Journal of Low Temperature Physics* 193 (Nov. 2018), pp. 1–7. DOI: 10.1007/s10909-018-2055-4.

[98] J. Wheeler et al. "Sub-kelvin thermometer for on-chip measurements of microwave devices utilizing two-level systems in superconducting microresonators". In: *Applied Physics Letters* 117.19 (2020), p. 192601. DOI: 10.1063/5.0029351. eprint: https://doi.org/10.1063/5.0029351. URL: https://doi.org/10.1063/5.0029351.

[99] X. Liu et al. "Superconducting micro-resonator arrays with ideal frequency spacing". In: *Applied Physics Letters* 111.25 (2017), p. 252601. DOI: 10.1063/1.5016190. eprint: https://doi.org/10.1063/1.5016190. URL: https://doi.org/10.1063/1.5016190.

[100] Darcy Barron et al. "Integrated Electrical Properties of the Frequency Multiplexed Cryogenic Readout System for POLARBEAR/Simons Array". In: *(in prep.)* ().

[101] M. Navaroli. "Precise Astronomical Polarization Angle Calibration and its Impact on Studying Lorentz and Parity Violation in the Cosmic Microwave Background". PhD thesis. University of California, San Diego, 2020.

[102] Yuuko Segawa et al. "Method for rapid performance validation of large TES bolometer array for POLARBEAR-2A using a coherent millimeter-wave source". In: vol. 2319. Feb. 2021, p. 040019. DOI: 10.1063/5.0038197.

[103] J. Aumont et al. "Measurement of the Crab nebula polarization at 90 GHz as a calibrator for CMB experiments". In: *Astronomy and Astrophysics* 514, A70 (May 2010), A70. DOI: 10.1051/0004-6361/200913834. arXiv: 0912.1751 [astro-ph.CO].